ABSTRACT

Title of Dissertation: GROWTH AND CHARACTERIZATION OF MULTIFERROIC $BATIO_3$-$COFE_2O_4$ THIN FILM NANOSTRUCTURES

Haimei Zheng, Doctor of Philosophy, 2004

Dissertation Directed By: Professor Lourdes Salamanca-Riba

Professor Ramamoorthy Ramesh

Department of Materials Science and Engineering

Multiferroic materials which display simultaneous ferroelectricity and magnetism have been stimulating significant interest both from the basic science and application point of view. It was proposed that composites with one piezoelectric phase and one magnetostrictive phase can be magnetoelectrically coupled via a stress mediation. The coexistence of magnetic and electric subsystems as well as the magnetoelectric effect of the material allows an additional degree of freedom in the design of actuators, transducers, and storage devices. Previous work on such materials has been focused on bulk ceramics.

In the present work, we created vertically aligned multiferroic $BaTiO_3$-$CoFe_2O_4$ thin film nanostructures using pulsed laser deposition. Spinel $CoFe_2O_4$ and perovskite $BaTiO_3$ spontaneously separated during the film growth. $CoFe_2O_4$ forms nano-pillar arrays embedded in a $BaTiO_3$ matrix, which show three-dimensional heteroepitaxy. $CoFe_2O_4$ pillars have uniform size and spacing. As the growth

temperature increases the lateral size of the pillars also increases. The size of the $CoFe_2O_4$ pillars as a function of growth temperature at a constant growth rate follows an Arrhenius behaviour. The formation of the $BaTiO_3$-$CoFe_2O_4$ nanostructures is a process directed by both thermodynamic equilibrium and kinetic diffusion. Lattice mismatch strain, interface energy, elastic moduli and molar ratio of the two phases, etc., are considered to play important roles in the growth dynamics leading to the nanoscale pattern formation of $BaTiO_3$-$CoFe_2O_4$ nanostructures.

Magnetic measurements exhibit that all the films have a large uniaxial magnetic anisotropy with an easy axis normal to the film plane. It was calculated that stress anisotropy is the main contribution to the anisotropy field. We measured the ferroelectric and piezoelectric properties of the films, which correspond to the present of $BaTiO_3$ phase. The system shows a strong coupling of the two order parameters of polarization and magnetization through the coupled lattices. This approach to the formation of self-assembled ferroelectric/ferro(ferri-)magnetic nanostructures is generic. We have created similar nanostructures from other spinel-perovskite systems such as $BiFeO_3$-$CoFe_2O_4$, $BaTiO_3$-$NiFe_2O_4$, etc., thus making it of great interest and value to a broad materials community.

GROWTH AND CHARACTERIZATION OF MULTIFERROIC $BATIO_3$-$COFE_2O_4$ THIN FILM NANOSTRUCTURES

By

Haimei Zheng

Dissertation submitted to the Faculty of the Graduate School of the
University of Maryland, College Park, in partial fulfillment
of the requirements for the degree of
Doctor of Philosophy
2004

Advisory Committee:

Professor Lourdes Salamanca-Riba, Chair/Advisor
Professor Ramamoorthy Ramesh, Co-advisor
Professor Alexander L. Roytburd
Professor Manfred Wuttig
Associate Professor Ichiro Takeuchi
Professor Ellen D. Williams

dedication

to my mother

ACKNOWLEDGEMENTS

I would like to express my sincere gratitude to my advisors, Prof. Lourdes Salamanca-Riba and Prof. Ramamoorthy Ramesh, for giving me the opportunity to work on this exciting project. I would especially like to thank both of them for their faith, guidance and support throughout the course of my Ph.D research. I have been working with Prof. Salamcanca-Riba since the first day I came to the U.S. starting as her TA, and then as her RA. I benefited from her guidance in every aspect during my Ph.D study, including her "structural analysis and electron microscopy" class, the discussions we held and intelligent suggestions she made regarding my research, her great patience during the corrections of my papers and my thesis, and her assistance on my preparation for conference talks. I deeply appreciate all her invaluable help, the care she showed for me, and the freedom she gave me.

Also, I have tremendous respect for Prof. Ramesh for his knowledge and passion for research. He has been excited about every small step forward I have made during my research. In addition, he always made me feel I could do anything. There are few who can instill such enthusiasm in his students and colleagues as he does Without his ever-present guidance and confidence in my work, my scientific achievements would not have been possible.

I would like to thank Prof. Alexander Roytburd for his kind assistance on the theoretical calculations of the magnetoelectric coupling effect as related to this project.

I appreciate the insights and advice Prof. Manfred Wuttig has given me on the growth of $BaTiO_3$-$CoFe_2O_4$ and the coupling effect in the $BiFeO_3$-$CoFe_2O_4$ system.

I am also grateful to Prof. Samuel E. Lofland, Prof. Dwight Viehland and Prof. Darrell G. Schlom for their valuable assistance in my research on this project.

I would like to thank the other members of my Ph.D committee Prof. Ichiro Tackeuchi and Prof. Ellen Williams for taking time out of their busy schedules to evaluate my work. I specially thank Prof. Ellen D. Williams for her consistent support and belief in my research.

I would like to give my special acknowledgements to Junling Wang as a friend and as a collaborator. All the ideas we shared have been very fruitful. Without his contribution this project would not have gone so well.

I would like to thank Dr. Satishchandra B. Ogale and Dr. Sanjay R. Shinde for their help with the magnetic measurements at the beginning of the project.

I would like to show my gratitude for the helping hands from my friends in our research group: Ladan Mohaddes-Ardahili for the XRD experiments, Dr. Florin Zavaliche for the PFM-MFM measurements, Zhenkun Ma for the d_{33} measurements, Tong Zhao and Seung Yeul Yang for the helpful suggestions in my experiments.

I would also like to thank Prof. Yuri Suzuki, Mike Scarpulla, Rajesh Chopdekar and Dr. Yayoi Takamura at UC Berkeley for their valuable discussions on the magnetic properties of the films while I was writing my dissertation. I extend my special thanks to Rajesh for spending so much time on helping me with the magnetic measurements and the proofreading of my dissertation.

I want to thank all of the group members at University of Maryland. And I also want to thank the new group members at UC Berkeley. My research has been so exciting because of all the talented and great team members I interact with daily.

I would like to thank all my friends who made my life in the U.S. very colorful.

Finally, I want to thank my mother, my brothers and my sisters for their love, enthusiasm and support. I would never have gone this far without their unwavering belief and support.

TABLE OF CONTENTS

LIST OF TABLES

LIST OF FIGURES

Chapter 1 Introduction

1.1 Multiferroic materials and magnetoelectric effect

1.1.1 Why multiferroics?: applications, issues

The term "Multiferroics" refers to a class of materials in which two or all three of the properties: ferroelectricity, ferromagnetism, and ferroelasticity occur simultaneously. A ferroelectric material exhibits a polarization even in the absence of an external electric field, and the direction of the spontaneous polarization can be reversed by an external electric field. Ferromagnetism is a phenomenon by which a material exhibits a spontaneous magnetization that can be switched by an externally applied magnetic field. Ferroelasticity refers to a spontaneous deformation in response to an applied stress. The simultaneous ferroelectricity and ferroelasticity is known as piezoelectricity, and leads to the wide and well established use of piezoelectric materials in transducer applications. Similarly, the coupling between ferromagnetism and ferroelasticity results in magnetostriction and the consequent application of piezomagnets as magnetomechanical actuators. A less known subgroup of materials, known as magentoelectric multiferroics, are simultaneously ferroelectric and ferromagnetic (or at least show some kind of magnetic ordering). These materials have stimulated significant interest both from the basic science and the application point of view.

The discovery of magnetoelectric materials was preceded by the development of the physics of magnetism and ferroelectricity. In a ferromagnetic material, the macroscopic magnetization is caused by the magnetic dipole moments of the atoms

tending to line up in the same direction. There are two phenomenological theories that successfully explained many of the ferromagnetic properties. One is the Curie-Weiss localized-moment theory[1] and the other is Stoner band theory of ferromagnetism[2]. In 1907, Weiss[1] postulated that an internal "molecular field" acts in ferromagnetic materials to align the magnetic moments parallel to each other. The origin of this molecular field was later understood to be the quantum mechanical spin exchange interaction, which causes electrons with parallel spins to have lower energy than electrons with antiparallel spins when the sign of the exchange interaction is negative, all other factors being equal. If the exchange interaction is positive a state with lower energy is the one with antiparallel alignment of the spins, so-called, antiferromagnetism. At temperatures below the, so-called, Curie temperature (T_c), the molecular field is so strong that the magnetic moments align even without an external field. At temperature higher than T_c, the thermal energy, kT, is larger than the alignment energy of the molecular field, resulting in a random orientation of the magnetic moment (paramagnetic behavior). The Weiss localized-moment theory explains the experimentally observed Curie-Weiss law behavior for the susceptibility, χ, of many magnetic materials, namely $\chi = \frac{C}{T - T_c}$ Eq.1. 1

In the Stoner theory[2], ferromagnetism is also due to the exchange interaction which is minimized if all of the spins are aligned. Opposite alignment of the spins leads to an increase in the band energy involved in transferring electrons from the lowest band states to band states of higher energy. This band energy prevents simple metals from being ferromagnetic.

The applications of ferromagnetic materials are largely related to the characteristics of their hysteresis loops. For example, a square-shaped hysteresis loop, with two stable magnetization states, is suitable for magnetic data storage, whereas a

small hysteresis loop that is easily switched between the two states is suitable for a transformer core.

A ferroelectric material is one that undergoes a phase transition from a high-temperature phase (paraelectric) to a low temperature phase (ferroelectric) that has a spontaneous polarization whose direction can be switched by an applied electric field. The existence or absence of ferroelectricity in an ionic material is determined by a balance between the short-range repulsions, which prefer the nonferroelectric symmetric structure, and additional bonding consideration, which might stabilize the ferroelectric phase. The most widely studied and used ferroelectric materials are oxides with perovskite structure, of the form ABO_3, such as $BaTiO_3$. The perovskite structure and ferroelectricity in $BaTiO_3$ are discussed in detail in section 1.2.1.

Ferroelectrics find a large range of applications, such as nonvolatile random access memories, capacitors (the high concentration of electric flux density results in high dielectric permeabilities), transducers and actuators (piezoelectricity), etc.

Magentoelectric multiferroics have all the potential applications of both their parent ferroelectric and ferromagnetic materials. In addition, a whole range of new applications can be envisaged [3]. The simultaneous ferroelectric and magnetic properties in a single material and the ability to couple the two order parameters allows an additional degree of freedom in device design. Such devices include, for example, faraday rotators operating in the microwave range. The figure of merit for the magnetoelectric coupling is determined by the value of $\varepsilon' M_z/\varepsilon''$, where M_z is the component of the magnetization in the direction of the magnetic wave propagation, ε' and ε'' are the real and imaginary parts of the dielectric permittivity[4]. The use of the magnetoelectric coupling, for example, for switching or modulation of the electric polarization by a magnetic field can create a magnetically switchable device in the

visible and IR spectra. Its operation consists of the variation in the magnitude of the linear double refraction with polarization under the action of a magnetic field. Magnetoelectic materials can also be applied as film wave guides in integral optics and fiber optical communications as reported by Yu. N. Venevtsev *et al*[13]. Other applications include multiple state memory elements, in which data can be stored both in the magnetic and electric polarizations, or novel memory media, which allow the writing of a ferroelectric data bit and the reading of the magnetic field generated by the coupling effect. Aside from the potential applications, the fundamental physics of multiferroic materials is rich and fascinating.

As early as 1894 P. Curie[4] claimed that symmetry conditions enable the bodies containing asymmetric molecules to be polarized in a magnetic field and, possibly, to be magnetized in an electric field. In 1916 S. A. Boguslavsky[5] predicted the existence of substances that simultaneously have electric and magnetic dipole moments. He also pointed out that an electric field may induce electric polarization equally with magnetic polarization (and vice versa). The existence of magnetoelectric materials was first experimentally observed in an unoriented Cr_2O_3 crystal by Astrov[6] in 1960. Rado and Folen then revealed the anisotropic nature of the magnetoelectric effect in oriented Cr_2O_3 crystals[7,8]. In late 1961, S. A. Smolenskiĭ and his colleagues experimentally proved the existence of magentoelectric effect in a solid solution of $PbFe_{2/3}W_{1/3}O_3{\cdot}Pb_2MgWO_6$[9]. At the beginning of 1962, G. S. Zhdanov et al. independently confirmed the existence of magetoelectric perovskite materials based on a study on the $PbTiO_3$-$BiFeO_3$[10] and $BiFeO_3$[11] systems. Later, a magnetoelectric effect was revealed in other structures and more and more systematic studies were undertaken[12,13,14].

All the magnetoelectric materials that have been studied to date can be classified into two categories: single phase ferroelectromagnets and multiferroic composites. In the following sections, these two classes of magentoelectric materials are discussed. Moreover, the theories on the magnetoelectric interactions are also reviewed.

1.1.2 Single phase multiferroics

Almost all the ferroelectromagnets are synthetic compounds, while only two natural ferroelectromagnetic crystals are known, namely, congolite $Fe_3B_7O_{13}Cl$ and chambersite $Mn_3B_7O_{13}Cl$[15,16]. The ferroelectromagnets can be classified into several fundamental classes[12] according to their structural features.

1. Compounds having the perovskite-type structure containing magnetic ions fully or partially occupying the octahedral positions, i.e., $BiFeO_3$, $Pb(Fe_{2/3}W_{1/3})O_3$, $Pb(Fe_{1/2}Nb_{1/2})O_3$, $Pb(M_{1/2}Re_{1/2})O_3$ (M = Fe, Mn, Ni, Co) etc. Typically, the compounds $Bi_{m+1}M_mO_{3m+3}$ ($M = Fe^{3+}$, Ti^{4+}) have a layered perovsike-like structure with alternating of bismuth and oxygen, and different numbers of octahedron in the packets. The octahedral positions contain either Fe^{3+} or Ti^{4+} ions. The exchange interaction between the Fe^{3+} ions within a packet occurs along the chain of Fe-O-Fe atoms forming an angle of about 180°. The Fe^{3+} ions of adjacent packets are separated by a layer of the diamagnetic Bi^{3+} and O^{2-} ions.

2. The hexagonal rare-earth manganites have the overall formula $MMnO_3$ (M = Y, Ho, Er, Tm, Yb, Lu, or Sc), and are ferroelectromagnets with antiferromagnetic or weak ferromagnetic properties[17,18,19,20]. Their crystal structure[12] consists of trigonal bipyramids connected by their vertices to form layers perpendicular to the sixfold axis. The Mn atoms lie inside the bipyramids, while the rare-earth atoms lie between the

layers of bipyramids. The hexagonal structure in these compounds arises from the small ionic radii of the rare-earth ions and the presence of covalent Mn-O bonds.

3. The boracites-compounds have the general formula $M_3B_7O_{13}X$ (M = Cr, Mn, Fe, Co, Cu, or Ni, and X = Cl, Br, or I), and are ferroelectric-antiferromagnets (some having weak ferromagnetism). In the high-temperature phase all the boracites have the cubic symmetry $\bar{4}3m$. Phase transitions arise with decreasing temperature in the sequence $\bar{4}3m \rightarrow mm2 \rightarrow m \rightarrow 3m$. In some compounds the $3m$ and/or m phases do not appear. A transition to the orthorhombic $mm2$ phase is accompanied in all the boracites by the onset of FE properties. In some cases, this is an improper FE transition [21]. The magnetic ordering in the boracites arises at temperatures considerably below room temperature.

4. The compounds BaMF$_4$ (M = Hn, Fe, Co, Ni) have an orthorhombic crystal structure at high-temperature. The lattice of the isomorphous BaMnF$_4$ and BaCoF$_4$ consists of distorted MF$_4$ octahedron connected by their vertices to form layers separated by the nonmagnetic Ba ions. The M-F-M configuration in the layer is close to linear[22]. The BaMF$_4$ compounds are pyro- or ferro-electrics. The temperatures of the FE transitions, obtained by extrapolation, lie above the corresponding melting points[23]. At high enough temperatures, antiferromagnetic or weak ferromagnetic ordering arises[24,25], while antiferroelectric and ferro-electro-elastic properties can also arise[22,26].

In addition to the compounds listed above, there are ferroelectromagnetic compounds of other structural types, which are not discussed here.

Table 1.1 gives some of the ferroelectromagnets and indicates the type of electric and magnetic ordering and corresponding temperatures of the electric and

magnetic transitions. The complete lists of the ferroelectromagnets and their physical characteristics can be obtained in early reviews[12,27,28].

Table 1.1 Some of the single phase ferroelectromagnetic oxides.

Compound	Type of electric order	Type of magnetic order	T_C (K)	T_N (K)
$Pb(Fe_{2/3}W_{1/3})O_3$	FE	AFM	178	363
$Pb(Fe_{1/2}Nb_{1/2})O_3$	FE	AFM	387	143
$Pb(Mn_{2/3}W_{1/3})O_3$	AFE?	AFM	473	203
$Pb(Fe_{1/2}Ta_{1/2})O_3$	FE	AFM	233	180
$Eu_{1/2}Ba_{1/2}TiO_3$	FE	FM	165	4.2
$BiFeO_3$	FE	AFM	1123	650
$BiMnO_3$	AFE	FM	773	103
$YMnO_3$	FE	AFM	913	80
$YbMnO_3$	FE	AFM/WFM	983	87.3
$HoMnO_3$	FE	AFM/WFM	873	76
$ErMnO_3$	FE	AFM	833	79
$ScMnO_3$	FE	AFM	-	120
β-$NaFeO_2$	FE	WFM	723	723
$Co_{1.75}Mn_{1.25}O_4$	FE	FIM	170	170

Notes: FE-ferroelectric, AFE-antiferroelectric, FM-ferromagnetic, AFM-antiferromagnetic, WFM-weak ferromagnetic, FIM-ferrimagnetic. For more detailed information see review by G. A. Smolenskiĭ and I. E. Chupis[12]

The possible coexistence of the spontaneous magnetization and polarization in the same phase does not contradict the general criteria for appearance of ferromagnetism and ferroelectricity taken separately. Namely, magnetic ordering is governed by the exchange interaction of the electron spins, while ferroelectric ordering is governed by the redistribution of charge density in the lattice. However, limited ferroelectromagnets exist in nature or have been synthesized in the laboratory.

The fundamental physics behind the scarcity of ferromagnetic/ferroelectric coexistence has been explored by Nicola A. Hill[14]. It was found that, in general, the d electrons in transition metals, which are essential for magnetism, reduce the tendency for off-center ferroelectric distortion. Consequently, an additional electronic or structural driving force must be present for ferromagnetism and ferroelectricity to occur. Detailed theoretical analysis can be obtained in the original paper[14].

1.1.3 Multiferroic composites

Simultaneous ferroelectric and ferromagnetic properties can be achieved in multiferroic composites. Such multiferroic composites consist of a ferroelectric phase (also piezoelectric) and a ferromagnetic phase (also piezomagnetic or magnetostrictive). The coupling between the two order parameters is through a stress mediation, i.e., a magnetic field induces a distortion of the magnetostrictive phase, which in turn distorts the piezoelectric phase in which an electric field is generated. The composite can be considered as a new material with multiferroic properties. The magnetoelectric effect is extrinsic in this case since magnetoelectric effect is not exhibited by any of the constituent phases on their own. Such physical property of the composite is called a "product property"[29], which refers to an effect in one of the phases or submaterials which in turn leads to a second effect in the other phase.

The concept of "product property" in multiferroic composites was first proposed by the Philips Laboratory[29] using $BaTiO_3$-$CoFe_2O_4$ as a model system. The multiferroic $BaTiO_3$-$CoFe_2O_4$ composite was synthesized by unidirectional solidification. A eutectic composition $0.62BaTiO_3$-$0.38CoFe_2O_4$ was selected from the quaternary system Fe-Co-Ti-Ba-O[29,30,31,32]. The magnetoelectric coefficient in such composite material (dE/dH = 130 mV/cm Oe) was reported to be superior to

single-phase materials such as Cr_2O_3. There have been considerable studies on multiferroic composites thereafter. In addition to the above "one-step process" of unidirectional solidification of eutectics, different methods have been used to synthesize the composite materials, i.e. ceramic sintering[33,34,35], gluing/bonding of multilayers[36,37,38,39,40], etc. Various constituent materials have been reported as multiferroic composite materials. Table 1.2 lists several multiferrioc materials with the preparation methods that have been reported in the literature.

Table 1.2 Multiferroic composite materials and preparation methods.

Composite	Preparation method	Ref
$BaTiO_3$-$CoFe_2O_4$	Eutectic unidirectional solidification	[29,30,31,32,41]
$BaTiO_3$-$NiFe_2O_4$	Eutectic unidirectional solidification, Ceramic centering	[42,43,44,45]
$BaTiO_3$-Ni(Co, Mn)Fe_2O_4	Ceramic centering	[46,47,48]
$Bi_4Ti_3O_{12}$-$CoFe_2O_4$	Ceramic centering	[48]
$BaPbTiO_3$-$CuFeCrO_4$	Ceramic centering	[49]
PZT-$NiFe_2O_4$	Ceramic centering	[50]
PZT-$CoFe_2O_4$	Ceramic centering	[50,51]
PZT-Tb-Dy-Fe alloy (Terfenol-D)	Multilayers bonded epoxy binders	[36,37,52]
$Pb(Mg_{1/3}Nb_{2/3})O_3$-$PbTiO_3$ (PMN-PT)/Terfenol-D	Multilayers bonded epoxy binders	[38]
PZT/$La_{0.7}Sr_{0.3}MnO_3$	Multilayers by tape casting	[40]
PZT/polyvinylidene-fluoride (PVDF) and Terfenol-D/PVDF	Multilayers by hot-molding	[39]

The advantages of multiferroic composites over single phase multiferroics are: (i) the physical properties of the materials can be tailored by the selection of different

constituent phases and their volume ratios in order to meet specific applications. (ii) The magnetoelectric coupling effect in multiferroic composites is much higher than single phase ferroelectromagnets.

In the present work, $BaTiO_3$-$CoFe_2O_4$ was selected as a model system. Multiferroic $BaTiO_3$-$CoFe_2O_4$ thin film nanostructures with epitaxial features were synthesized to explore the possibility of enhancement of the magnetoelectric properties through the coupling of the lattices. Detailed thin film design is discussed in section 1.2.4.

1.1.4 The magnetoelectric effect

A thermodynamic analysis of the magnetoelectric (ME) coupling effect in single phase ferromagnetoelectrics was conducted by G. A. Smolenskiĭ[12,53], who investigated the behavior of crystals that display ferroelectric and ferromagnetic properties near the phase transition temperatures. The equilibrium properties of the material can be described by the Landau theory using a free energy expansion in power series of electric and magnetic moments.

Assume $\phi(P,M) = \phi(-P,M) = \phi(P,-M) = \phi(-P,-M)$, where P is the polarization, and M the magnetization. The thermodynamic potential $\phi(P,M)$ is written as:

$$\phi = \phi_0 + \alpha P^2 + \frac{\beta}{2}P^4 - PE + \alpha' M^2 + \frac{\beta'}{2}M^4 - MH + \gamma P^2 M^2 \qquad \text{Eq.1. 2}$$

where α, β, α', β', and γ are coefficients, and ϕ_0 is a constant.

An analysis of the expansion, with the requirement of minimum potential and stability conditions, yields a number of important results[13], which include:

1) Appearance of a break in the temperature dependence of magnetic (dielectric) susceptibility at the ferroelectric (magnetic) transition temperature;
2) A jump in the magnetic (dielectric) susceptibility at the ferroelectric (magnetic) transition temperature.

Although this thermodynamic analysis was based on single phase magnetoelectric materials, the approach can be extended to magnetoelectric composites. In a ferroelectric and magnetic two-phase system, the elastic interactions between the two phases have to be considered in addition to the ferroelectric and ferromagnetic contributions in the free energy expression. Thermodynamic analysis of the present $BaTiO_3$-$CoFe_2O_4$ two-phase magnetoelectric composite thin films was performed by Prof. A Roytburd[54]. A more detailed description of this analysis is discussed in chapter 4.

The atomic mechanisms of the magnetoelectric effect involve changes due to the electric field E of some parameter in a spin Hamiltonian[55,56]. The atomic ME mechanisms reported so far apply to two types of materials[57], to be referred to as type 1 and type 2. The two types of materials represent limiting situations in regards to the relative importance of the crystalline electric field and the spin-orbit coupling in determining the energy levels of the magnetic ions. Also considered by this theory is the use of thermodynamic perturbation theory for calculating the fractional components of each phase and temperature dependences. It is suggested that this mechanism is probably the most effective one because it is based on the lowest possible order in the perturbation.

The magnetic ions in type 1 magnetoelectric materials are transition metal ions whose ground state in the total crystalline electric field is an orbital singlet. An additional assumption is that the width in energy of the ground state spin multiplet is

small compared to the energy separation between the orbital ground state and the first excited orbital state. The mechanism for magnetoelectric susceptibility (α) proposed in this theory involves changes due to E of the quadratic axial term ("D" term) in the spin Hamiltonian.

The magnetic ions in type 2 magnetoelectric materials are rare-earth ions in which an applied electric field E induces in a change in a parameter, similar to the g-factor of the rare-earth ions involved in the magnetoelectric susceptibility α in such materials. A more detailed description of the atomic theory of the magnetoelectric effect can be obtained in the original paper[55,56,57].

1.2 Design of multiferroic $BaTiO_3$-$CoFe_2O_4$ thin films

1.2.1 Perovskite structure and ferroelectricity in $BaTiO_3$

Most ferroelectric materials have a perovskite structure, named after the $CaTiO_3$ perovskite mineral. In fact ferroelectricity itself is closely related to the intrinsic frustration associated with perovkite structures. A perfect perovskite structure (see Fig.1.1) has a general formula of ABO_3, where A represents a divalent or a trivalent cation, and B is typically a tetravalent or a trivalent cation. The A ions occupy the corners of the cube, while the B ions sit in the body center position inside an octahedron formed by the oxygen ions, which are at the face centers.

Barium titanate ($BaTiO_3$) is one of the most studied ferroelectric materials and can serve as an excellent example to illustrate the intrinsic structural frustration and thus the ferroelectricity associated with perovskite structures. The tetravalent Ti^{4+} ions occupy the B sites of the $BaTiO_3$ perovskite structure and are surrounded by O^{2-} in an octahedral configuration. The large Ba^{2+} ions and O^{2-} ions form an *f.c.c.* – like lattice

with Ti ions fitting into octahedral interstices. The lattice constant of $BaTiO_3$ is a = 0.401 nm (at just above the ferroelectric transition temperature T_c = 120 °C), so the distance between Ti^{4+} and O^{2-} ions is 0.2005 nm. However, the sum of the Ti^{4+} and O^{2-} ionic radii is: $r = r_{Ti^{4+}} + r_{O^{2-}}$ = 0.064 nm + 0.132 nm = 0.196 nm. Obviously, the distance between Ti^{4+} and O^{2-} ions is larger than the sum of the Ti^{4+} and O^{2-} ionic radii, that is, the space of the octahedral interstices is larger than the Ti^{4+} ion. Therefore, the Ti^{4+} ion can move relatively freely inside the oxygen octahedron with very small restoring force.

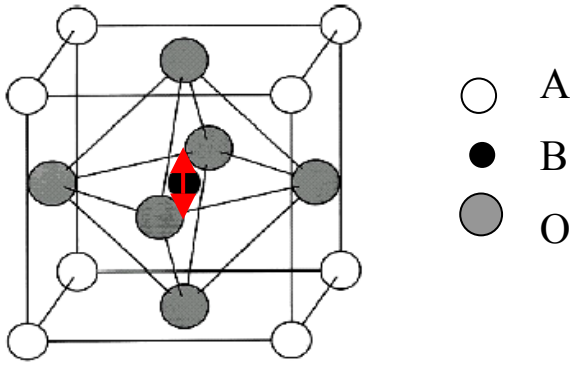

Fig.1.1 Cubic perovskite structure. The large A cations (white) occupy the unit cell corners. The small B cation (in black) is at the center of an octahedron of oxygen anions (in gray).

At high temperatures ($T > T_c$), the thermal energy is sufficient to allow the Ti^{4+} ions to move randomly from one position to another, so there is no fixed asymmetry. The open octahedral structure allows the Ti^{4+} ion to develop a large dipole moment in an applied field, but there is no spontaneous alignment of the dipoles. In this symmetric configuration the material is paraelectric, (i.e., no net dipole moment exists when E = 0). At temperatures below T_c, the structure changes

from cubic to tetragonal symmetry with the Ti^{4+} ion in an off-center position giving rise to a net dipole moment.

The behavior of the spontaneous polarization of ferroelectrics can be explained by thermodynamic (Landau-Ginzburg-Devonshire) theory[58]. We assume that the free energy F in one dimension may be expanded as a function of the polarization P:

$$F(P,T,E) = -EP + \alpha_0 + \frac{1}{2}\alpha_1 P^2 + \frac{1}{4}\alpha_2 P^2 + \frac{1}{6}\alpha_3 P^6 + \ldots \quad \text{Eq.1. 3}$$

where the coefficients α_n are temperature dependent. This series does not contain terms in odd powers of P if the unpolarized crystal has a center of inversion symmetry. The value of P in thermal equilibrium is given by the minimum of F as a function of P; differentiating the equation above with respect P gives:

$$\frac{\partial F}{\partial P} = 0 = -E + \alpha_1 P + \alpha_2 P^3 + \alpha_3 P^5 + \ldots \quad \text{Eq.1. 4}$$

The coefficient α_1 takes the form $\alpha_1 = \gamma(T - T_0)$, where γ is a positive constant and T_0 may be equal to or lower than the phase transition temperature, T_c. The assumed form of α_1 is a necessary result of mean field theory and its validity is supported by the experimentally observed Curie-Weiss law. A small positive value of α_1 indicates that the lattice is "soft" and close to instability. A negative value of α_1 indicates that the unpolarized state is unstable.

When α_2 is positive, we can neglect the α_3 term. The polarization for zero field can be found from Eq.1.5.

$$\gamma(T - T_0)P_s + \alpha_2 P_s^3 = 0 \quad \text{Eq.1. 5}$$

so that either $P_s = 0$ or $P_s^2 = \frac{\gamma}{\alpha_2}(T_0 - T)$. For $T \geq T_0, P_s = 0$ since γ and α_2 are positive. Therefore, T_0 is the Curie temperature. For $T < T_0$, the minimum of the free energy in zero field is at

$$|P_s| = \sqrt{\frac{\gamma}{\alpha_2}(T_0 - T)} \qquad \text{Eq.1. 6}$$

which is plotted in Fig.1.2A. Changes in the free energy and polarization at the transition temperature are continuous and the transition is a second order transition.

When α_2 is negative, the transition is first order. We must retain α_3 and take a positive value to ensure that F converges. The equilibrium condition for $E = 0$ in this case is:

$$\gamma(T - T_0)P_s + \alpha_2 P_s^3 + \alpha_3 P_s^5 + ... = 0 \qquad \text{Eq.1. 7}$$

so that either $P_s = 0$ or

$$\gamma(T - T_0) + \alpha_2 P_s^2 + \alpha_3 P_s^4 + ... = 0. \qquad \text{Eq.1. 8}$$

At the transition temperature T_c the free energies of the paraelectric and ferroelectric phases are equal. The plot of the free energy versus polarization at different temperature is shown in Fig.1.3. The existence of metastable phases during the phase transition is characteristic of first order transitions. Correspondingly, a sudden jump in polarization occurs at T_c. Fig.1.2B plots the P_s versus temperature for a first order phase transition.

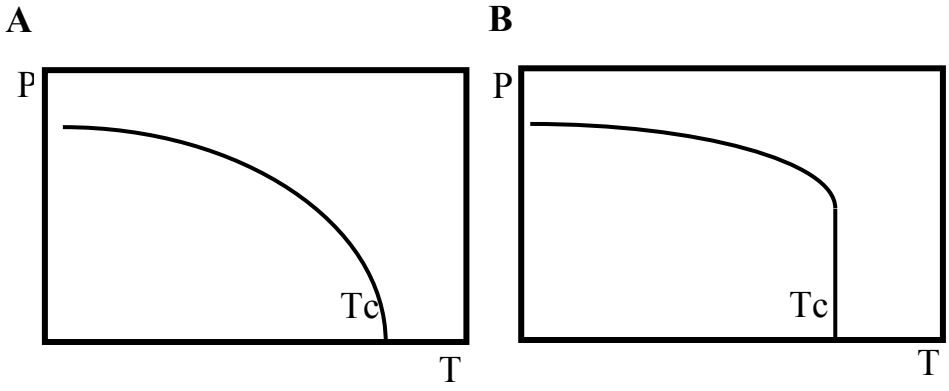

Fig.1.2 Polarization vs. temperature plot for: A. 2nd order phase transition; B. 1st order phase transition.

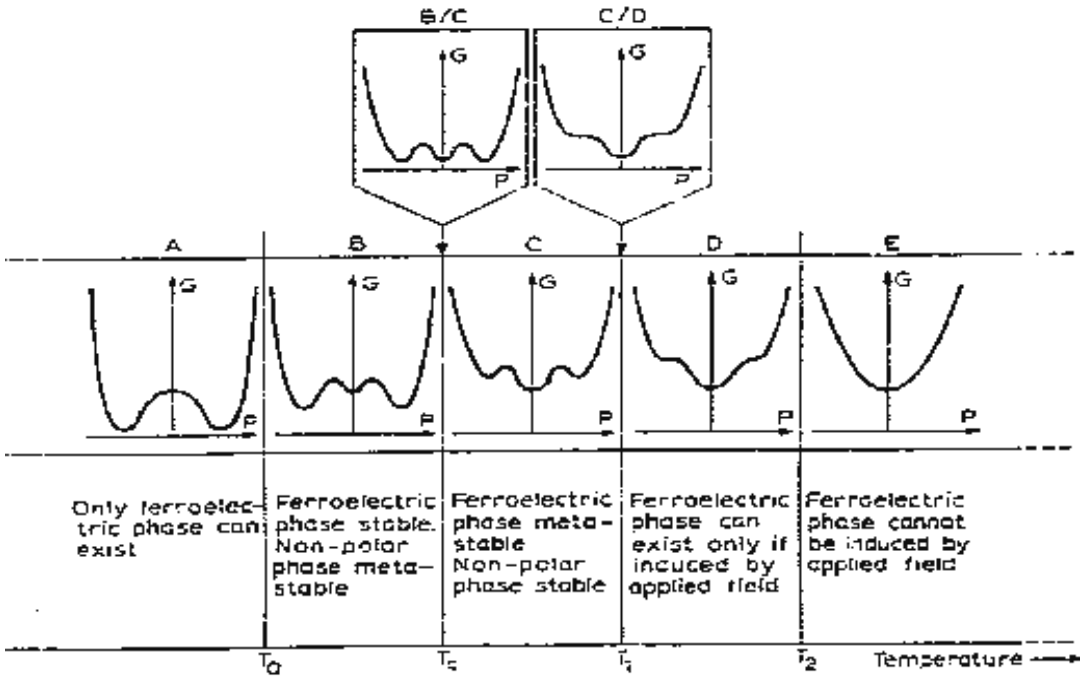

Fig.1.3 Gibbs free energy as a function of polarization in a 1st order phase transition.

1.2.2 Spinel structure and ferrimagnetism in $CoFe_2O_4$

$CoFe_2O_4$ belongs to the family of spinels. The spinel family is a group of compounds with a general formula of AB_2X_4 (A and B are cations; X is an anion, i.e., O, S, Se, Te). The spinel structure is named after the mineral spinel, $MgFe_2O_4$, which is the parent compound in this group. The crystal structure of spinel was determined by Bragg[59] and Nishikawa[60] independently in 1915. The cubic unit cell of spinel structure is illustrated in Fig.1.4. There are eight formula units per cubic unit cell, each of which consists of 32 anions and 24 cations, for a total of 56 atoms. As a consequence, the spinel lattice parameters are large, for instance, $CoFe_2O_4$ a = 8.38 Å.

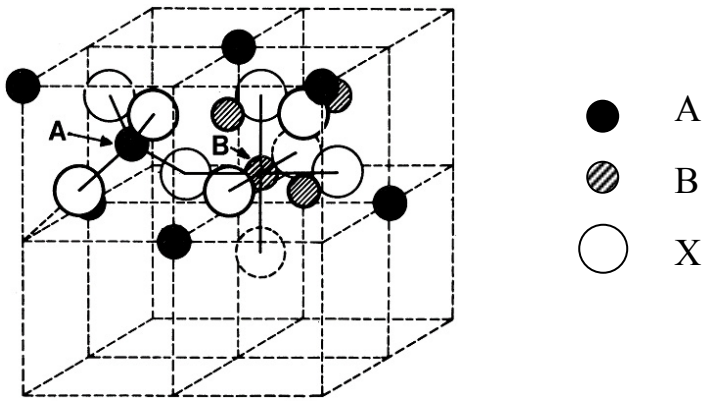

Fig.1.4 Schematic of the spinel structure, showing octahedral and tetrahedral sites occupied by A and B cations.

The 32 anions, i.e., O^{2-}, are arranged in a face-centered cubic (*f.c.c.*) lattice. There are 64 tetrahedral interstices (A sites) that exist between the anions, 8 of them are occupied by cations. There are 32 octahedral interstices (B sites) between the anions, 16 cations occupy half of the sites. Full occupation of the tetrahedral (8a) sites with a divalent transition metal produces a normal spinel structure, while occupation

of the octahedral (16d) sites with divalent transition metal ions yields an inverse spinel structure. Table 1.3 shows the site occupancy in the normal and inverse spinels. If divalent transition-metal ions are present in both A and B sublattices, the structure is mixed or disordered.

$CoFe_2O_4$ has an inverse spinel structure, with 8 Co^{2+} occupying half of the octahedral sites (16d) and 16 Fe^{3+} occupying the rest of octahedral and the 8 tetrahedral sites.

Table 1.3 Site occupancy in Normal and Inverse spinels.

Site Type	Interstices (per unit cell)	Number of Interstices Occupied (per unit cell)	Normal Spinel Cation Occupation	Inverse Spinel Cation Occupation
Tetrahehral (A)	64	8	8 M^{2+}	8 M^{3+}
Octahedral (B)	32	16	16 M^{3+}	8 M^{3+} , 8 M^{2+}

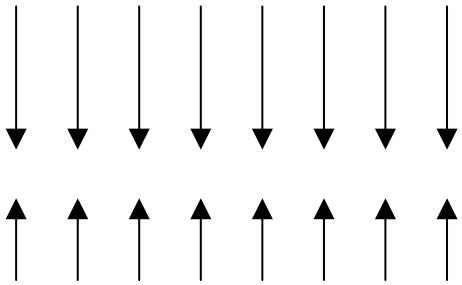

Fig.1.5 Schematic of ordering of magnetic ions in a ferrimagnetic lattice

The magnetic properties of spinel-phase ferrimagnets are rich and complex. The term ferrimagnetism was first used by Néel[61] to describe the properties of ferrites, which combine the resistivity of good insulators with high permeability. Ferrimagnets behave similar to ferromagnets, in that they exhibit a spontaneous magnetization

below some critical temperature, T_c, even in the absence of an applied magnetic field. In a ferrimagnet, the exchange coupling between adjacent magnetic ions leads to antiparallel alignment of the localized moments, which is similar to antiferromagnets. The overall magnetization occurs because the magnetization of one sublattice is greater than that of the other sublattice. A schematic of the ordering of magnetic moments in a ferrimagnet is shown in Fig.1.5.

In spinel ferrimagnets, there are different cation moments of the same cation on different sites. Magnetic ordering in spinels can be described by mean field theory, which considers the exchange interactions between cations[62]. In mean field theory, the magnetic ordering temperatures (either Curie for ferromagnetic materials or Néel for antiferromagnetic materials) are functions of oxygen-mediated superexchange interactions between magnetic ions. Superexchange is the mechanism for electron hopping between magnetic cations and oxygen anions. When an excited electron from an oxygen ion transfers to an adjacent transition-metal ion, it must possess the same spin as the electrons on the transition metal if the metal ion has a less than half-filled *d*-shell. This is in accordance with Hund's rule for high-spin metal ions, which is the case for spinels. The spin of the remaining unpaired electrons in the oxygen ions should be of opposite spin compared with the electron transferred to the metal according to Pauli exclusion principle. Therefore, a negative exchange integral and antiferromagnetic coupling are expected, according to the superexchange mechanism. Superexchange depends on the orientation of the *p*-orbital of the oxygen ion with respect to the near-neighbor transition metals. If the adjacent transition-metal ions are at an angle near 180° with an oxygen ion, the magnitude of the exchange integral is large and the sign is in negative (large antiferromagnetic coupling Jex << 0).

However, as the angle is decreased to 90°, the exchange integral becomes small and positive (small ferromagnetic coupling Jex ~ +0).

The phenomenon of ferrimagnetism can be described further using Néel's two-sublattice theory[61]. This model assigns two internal Weiss fields to the A and B sublattices, respectively. The sublattice magnetizations, M_A and M_B, are associated with moments of ions in the octahedral and tetrahedral sites, respectively. The internal fields arise from A-A, B-B, and A-B superexchange interactions. Assuming that the A-B interaction drives the antiparallel alignment, and that both A-A and B-B interactions are ferromagnetic. The total magnetization is:

$$M = M_A + M_B = \alpha n \mu_A + \beta n \mu_B \qquad \text{Eq.1. 9}$$

where n is the number of magnetic ions per unit volume, α is the fraction of A ions, β is the fraction of B ions, μ_A is the average magnetic moment of an A ion in the direction of the field at certain temperature, and μ_B is the average moment of a B ion. Using this simple model, Néel was able to predict quite accurately the saturation magnetization of some of the inverse spinel ferrites, and their Neel temperatures. Nevertherless, this model fails to describe the properties of mixed spinel structures.

A more sophisticated model for exchange coupling in spinel ferrites was developed by Yafet and Kittel[63].

Due to their high resistivity compared with ferromagnetic materials, ferrimagnetic materials find applications in situations where the electrical conductivity shown by most ferromagnetic materials would be detrimental. For example, they are widely used in high-frequency applications, because an ac field does not induce undesirable eddy currents in an insulating material.

1.2.3 Multiferroic $BaTiO_3$-$CoFe_2O_4$ composites – A review

Multiferroic $BaTiO_3$-$CoFe_2O_4$ composites are a model system illustrating magnetoelectric effect "product properties". As we discussed in the previous sections, $BaTiO_3$ is a typical ferroelectric material with large piezoelectricy; $CoFe_2O_4$ is ferrimagnetic with large magnetostriction. Composites of $BaTiO_3$-$CoFe_2O_4$ combine the ferroelectricity of $BaTiO_3$ and ferrimagnetism of $CoFe_2O_4$. The magnetoelectric coupling effect is through stress mediation. When a magnetic field is applied to the composite, there is stress generated by the $CoFe_2O_4$ due to its magnetostriction. Such a stress can create an electric field in the $BaTiO_3$ due to its piezoelectricity. The reverse process is also possible in which an electric field applied to the composite produces a stress due to the piezoelectric response of the $BaTiO_3$. The stress induces a magnetic field in the $CoFe_2O_4$ due to its magnetostriction.

Earlier work[29,30,31] on $BaTiO_3$-$CoFe_2O_4$ was on eutectic composites ($0.62BaTiO_3$-$0.38CoFe_2O_4$) synthesized by unidirectional solidification. The unidirectional solidification of eutectics is a method that has been used to produce an anisotropic composite directly from the melt[64,65]. To make the eutectic melt $BaCO_3$, $CoCO_3$, TiO_2, and Fe_2O_3 were used as starting materials. In order to obtain highly homogeneous melts the melt is kept above the melting temperature (T_{melt} = 1350 ºC) for a few hours in the desired atmosphere before the unidirectional solidification process starts. Then, a Pt 20% Rh wire is introduced at the top of the capillary until it is wetted by the melt. After that the wire is withdrawn at the desired speed and the temperature is regulated such that the thickness of the film has the maximum value for the growth of a rod with a stable (constant) diameter.

Among the phases of the quinary system Fe-Co-Ti-Ba-O there are several possible phases, besides the liquid phase. These are perovskite $BaTiO_3$, spinel

$CoFe_2O_4$, magneto plumbite phase $BaFe_{12-2y}Co_yTi_yO_{19}$, hexagonal $BaFe_{12}O_{19}$, $BaCo_6Ti_6O_{19}$, and miscible phases [66] of $CoFe_2O_4$ and Co_2TiO_4. Fig.1.6 shows a simplified composition tetrahedron for Fe, Co, Ti and Ba oxides at the corners[30]. At P, the perovskite $BaTiO_3$ phase is present. S' and S are the spinel phases with composition Co_2TiO_4 and $CoFe_2O_4$, respectively. The solid phase P and S would be situated on a curve in the plane through SS' and P, e.g. a curve starting at Q and intersecting the line PS at R. This curve is the projection of a temperature/composition curve at a constant P_{O_2}. In practice, however, because the S phase is not restricted to compositions on the line SS' and the P phase is not restricted to the point P; this curve of composition of the liquids will be situated on a regulated surface between the two solid phases. In order to obtain regular eutectic structures upon solidification under steady state conditions, this curve has to be determined for each O_2 pressure. However, it is found that there is not much influence of the O_2 pressure on the position of the curve of coupled growth.

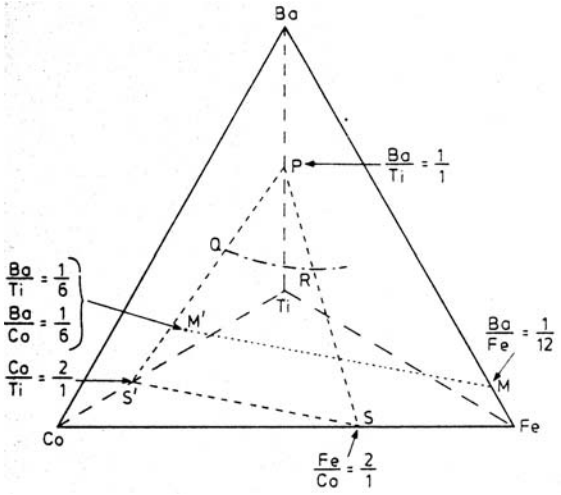

Fig.1.6 Simplified diagram of the Ba-Ti-Co-Fe-O quinary system giving the ratios of the metallic components.

The unidirectional solidification helps in the decomposition of the eutectic liquid composition into alternate layers of the constituent phases: a piezoelectric $BaTiO_3$ perovskite phase and a piezomagnetic $CoFe_2O_4$ spinel phase.

The unidirectional solidification process requires high temperature, and a critical control over the composition especially when one of the components (oxygen) is gas, and unexpected third phases can appear in the composites.

Sintered magnetoelectric composites have been an alternative to the in-situ eutectic composite formation. Sintered composites have many advantages over in-situ composites[33,46]. The sintered composites are much cheaper and easier to fabricate. Moreover, the molar ratio of the phases, grain size, and sintering temperature are easily controllable in sintered composites. There are some important issues in the fabrication of sintered magnetoelectric particulate composites. First, no chemical reaction should occur between the piezoelectric and magnetostrictive phases during the sintering process. Chemical reactions may reduce the piezoelectricity or magnetostriction of each phase. Second, the resistivity of the magnetostrictive phase should be improved. This has been a problem for most of the sintered composites because a low resistivity induces leakage which makes the electric poling difficult. Good dispersion of the ferrite particles in the matrix (to avoid the connection of ferrite particles into chains) is required in order to sustain sufficient electric resistivity of the composite. Third, mechanical defects such as pores at the interface between the two phases should be reduced in the composite in order to achieve good mechanical coupling.

To improve the resistivity of the composite, Ni and Ni-Co ferrites have been used as the magnetostrictive phase (i.e., $Ni_{0.9}Co_{0.1}Fe_2O_4$[47,48]), since $NiFe_2O_4$ has a higher resistivity than $CoFe_2O_4$. Also, PZT instead of $BaTiO_3$ has been used as the

ferroelectric phase[67,68] in composites in order to improve the piezoelectricity and consequently the magnetoelectric coefficient of the composite.

Laminate composites of piezoelectric and magnetostrictive materials have gained considerable attention due to the large ME effect (dE/dH = 5.90 V/cm·Oe) found in these composites[36]. There are many recent research work reported on multiferroic multilayers, in which alternate layers of ferroelectric and ferromagnetic phases are bonded. The piezoelectric coefficient and thickness ratio of the two layers are important factors in the multilayered composite to obtain a high magnetoelectric coefficient[37]. The problem associated with low-resistivity of ferrites can be eliminated in a layered structure.

Prior to the present work, almost all the previous work on multiferroic composites had focused on bulk ceramics. In the present work, we created heteroepitaxial $BaTiO_3$-$CoFe_2O_4$ nanostructure thin films. The films were designed in an attempt to explore means to enhance the coupling effect between the ferroelectric and ferromagnetic order parameters through the coupled lattices. Thin film design and challenges are discussed in the following section. This work focuses on the growth of the $BaTiO_3$-$CoFe_2O_4$ nanostructures as well as their ferroelectric and ferromagnetic properties. The indirect measurements on the magnetoelectric coupling effect as well as theoretical analysis on the enhanced coupling effect in the nanostructures are presented.

1.2.4 Design of $BaTiO_3$-$CoFe_2O_4$ thin film nanostructures

In a film-on-substrate geometry, the two-phase composite can be created in two extreme forms as illustrated schematically in Fig.1.7 (A, B). Fig.1.7A shows a "multilayer" geometry consisting of alternating layers of the ferroelectric phase

(perovskite $BaTiO_3$) and the ferro/ferrimagnetic phase (spinel $CoFe_2O_4$). Fig.1.7B shows a vertically aligned structure, with one phase (i.e., $CoFe_2O_4$) forming pillars embedded in a matrix of the other phase (i.e., $BaTiO_3$). When the magnetoelectric coupling is purely through elastic interactions, the coupling effect in the multilayer structure is negligible due to the clamping effect from the substrate[69]. Therefore, our effort is on creating and analyzing vertically aligned nanostructures. According to our thermodynamic analysis an enhanced coupling is expected from the vertically aligned nanostructures due to the coherent interface between the two phases and the vertical geometry.

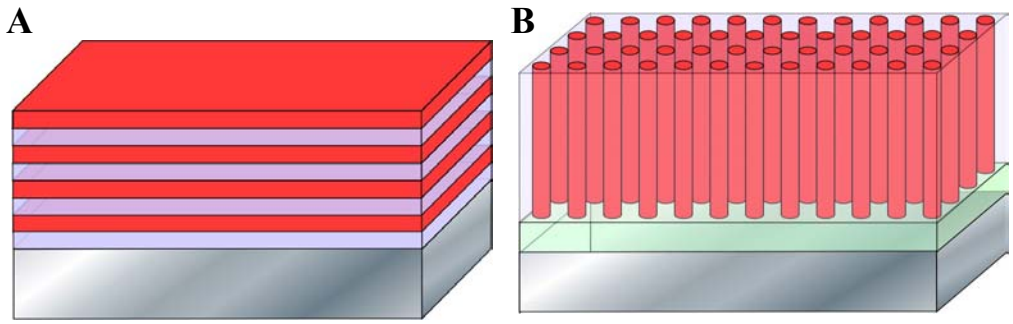

Fig.1.7 A. Schematic illustration of a multilayer structure of alternating ferroelectric and ferromagnetic layers on a substrate; B. Schematic illustration of a vertically aligned thin film structure consisting of pillars of one phase embedded in a matrix of the other phase on a substrate.

The Ba-Ti-Co-Fe-Oxide system is a very complex system, in which there are many possible phases as we discussed in section 1.2.3. The creation of $BaTiO_3$-$CoFe_2O_4$ vertically aligned two-phase nanostructures is a challenge and also a critical

issue for the success of this project. In order to obtain high quality $BaTiO_3$-$CoFe_2O_4$ thin film nanostructures, several aspects have to be considered. First is to obtain high quality two-phase structures by controlling the chemical stoichiometry of the two phases, elimination of impurity phases, etc. Second is to achieve high quality interfaces between the two phases, i.e. sharp, coherent interfaces and no interdiffusion between the two phases. Third are the ferroelectric/piezoelectric and magnetic properties. High resistivity is one of the important requirement in order to obtain large polarization and magnetoelectric coupling. A systematic study of the growth of $BaTiO_3$-$CoFe_2O_4$ thin film nanostructures is discussed in chapter 3.

Another critical issue in this project is the measurement of ferroelectric/piezoelectric and magnetic properties, as well as magnetoelectric coupling effect, which are discussed in chapter 4. Direct measurement of polarization is difficult for bulk ceramics due to a large leakage current. In the present work, ferroelectric/piezoelectric and magnetic hysteresis loops from the nanostructure films were obtained. The effects of changes in the structure on the properties of the films are systematically studied and presented in chapter 4. The magnetoelectric coupling effect in $BaTiO_3$-$CoFe_2O_4$ nanostructures was studied indirectly by the measurement of magnetization changes as a function of temperature. A thermodynamic analysis was conducted, which illustrates that the strong coupling observed in the $BaTiO_3$-$CoFe_2O_4$ thin film nanostructures derives from a strong coupling through the crystal lattices. Direct measurements of magnetoelectric coupling by measuring the change of magnetization by applying an electric field or the change of polarization by applying a magnetic field are in progress.

In order to compare the differences in the magnetoelectric coupling effect in vertically aligned nanostructures with that in multilayer structures $BaTiO_3$-$CoFe_2O_4$

multilayer structures were also fabricated. The structure and properties of the multilayer structures are discussed briefly in chapter 5.

The approach of multiferroic nanostructures in the present work is generic. Similar structures have been obtained in related systems, i.e., $BiFeO_3$-$CoFe_2O_4$, $BaTiO_3$-$NiFe_2O_4$[70], $PbTiO_3$-$CoFe_2O_4$[71], etc. As an example, the growth and properties of self-organized $BiFeO_3$-$CoFe_2O_4$ nanostructures are discussed in chapter 6.

Chapter 7 summarizes the research presented in this dissertation and addresses possible future work.

Chapter 2 Experimental Techniques

2.1 Pulsed laser deposition

Pulsed laser deposition (PLD) is the thin film growth technique that has been used in this work. Fig.2.1 is a schematic diagram of a laser ablation system. As shown in Fig.2.1, the basic components of a PLD system include a laser beam source and a stainless steel vacuum chamber with a rotating target holder and a substrate heater. In a laser ablation process, a pulsed laser beam (typically 30 ns pulses with energy in the range of 0.01-1.2 J and at a frequency of 1-20 Hz) is focused onto a target by a lens external to the chamber. Materials are dissociated from the target surface and ablated out with strong forward-directed particles towards the substrate, which is mounted on the temperature variable heater block. Multiple targets can be used during the deposition process, enabling the growth of a multilayered film. The ablation process takes place in a vacuum chamber - either in vacuum or in the presence of some background gas. In the case of oxide films, oxygen is the most common background gas.

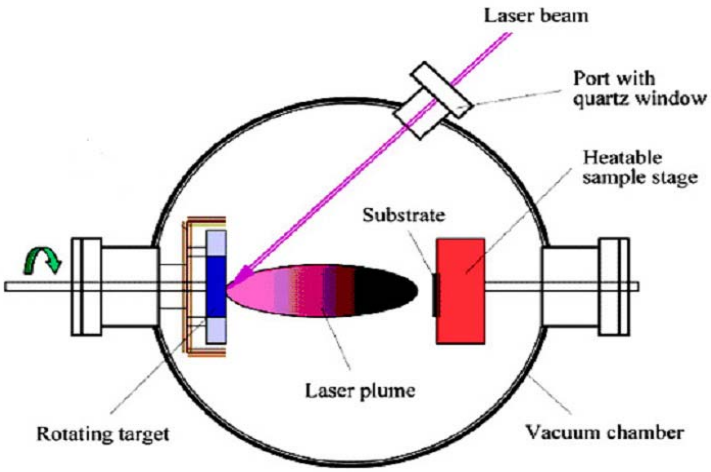

Fig.2.1 Schematic of a pulsed laser deposition system.

A pulsed laser deposition process involves complex physical phenomena such as collisional, thermal, and electronic excitation, exfoliation and hydrodynamics etc[72]. Generally, a PLD process can be divided into the following four steps: i. laser radiation interaction with the target; ii. dynamics of the ablation materials; iii. deposition of the ablation materials on the substrate; iv. nucleation and growth of a thin film on the substrate surface. Each of the above steps is critical to the quality and characteristics of the films i.e. crystallinity, stoichiometry, uniformity, and surface roughness. During deposition parameters are optimized to achieve high quality film growth. These include substrate temperature, laser energy density and frequency, target-to-substrate distance, base pressure and deposition gas pressure etc. The substrate temperature is critical to the crystallinity of the films. Normally, an amorphous phase forms when the substrate temperature is below a certain value. As the substrate temperature increases films start to crystallize. To achieve an epitaxial growth the substrate temperature should be optimized, which is different for different materials. The energy density of the laser beam has significant effects on the uniformity of the film. Target-to-substrate distance is a parameter that governs the angular spread of the ablated materials. The oxygen partial pressure is also a very important parameter in the growth of oxide films. The chamber is normally pumped down to a base pressure of ~1 x 10^{-5} Torr before the reactive gas, such as oxygen, is introduced into the chamber.

The lasers commonly used for PLD include ArF, KrF, XeF excimer lasers and Nd:YAG laser. It is generally recognized that the shorter the wavelength the more effective the laser ablation process. The laser used in this study was a KrF laser with a wavelength of 248 nm and pulse width of 30 ns.

The films studied in the present work were deposited at a dynamic oxygen pressure of 100 mTorr. The substrate temperature varied from 700 °C to 950 °C. Substrates were cleaned using a sequence of ultrasonic baths in trichloroethyene (TCE), acetone and methanol prior to loading into the chamber for deposition. A shutter was used to allow the target to be cleaned by pre-ablating the surface with the laser beam without contamination of the substrate. A laser energy density of ~1.5 J/cm^2 was used, corresponding to a growth rate of 10 nm/min. The samples were cooled down at a rate of 5 °C per minute in a 760 Torr O_2 atmosphere after deposition.

One of the main advantages of PLD is its versatility. Many materials can be deposited in a wide variety of gases over a broad range of gas pressures and substrate temperatures. Furthermore, the process is conceptually simple in that a laser beam vaporizes a target surface producing atoms and molecules that deposited on the substrate forming a film with the same composition as the target. Because of the very short pulse width of the laser, the evaporation of the target is negligible. When the target material explodes towards the substrate different components have similar deposition rates making the film have the exact composition as the target material. Another primary advantage of PLD is its cost-effectiveness. Multiple chambers can be set up around one laser source and laser beam can be directed to each chamber using mirrors and lenses. In addition, PLD is a fast and relatively clean process, and able to produce multilayer hetero-structures by simply using several targets.

There are, however, certain drawbacks associated with PLD. The intrinsic "splashing" associated with laser ablation results in the incorporation of micron to submicron size particles on the film surface. However, a number of schemes can eliminate the particles, which include using a high quality target, velocity filter and shadow mask, etc. Scaling up is another concern for PLD. The highly directional

plume makes the film uniform only over a relatively small area. PLD is somewhat limited in the investigation of new materials in the research environments. Nevertheless, with the demand for improved electronics based on metal-oxide, or other multicomponent thin films, the commercial-scale development of PLD systems is possible. It has been reported[73] that some PLD systems can deposit thin films on 8-inch wafers with the deposition rates of more than 1 micron-cm^2/s.

2.2 Structural characterization

2.2.1 X-Ray diffraction

X-ray diffraction is the result of the interaction between X-rays and the periodic electronic potential geometry of crystals. Diffraction occurs as waves interact with a regular structure whose repeat distance is about the same order as the wavelength of the waves. This is expressed in Braggs's Law:

$$n\lambda = 2d\sin\theta \qquad \text{Eq.2.1}$$

where n is an interger, λ is the wavelength of X-rays (1.54056 Å for copper K_α), d is the lattice interactomic spacing, θ is the diffraction angle.

X-ray structural analysis can be used to determine the epitaxial feature of the thin films and nanostructures. The techniques include θ-2θ scans, ϕ scans, and rocking curves. θ-2θ scans are used to determine the crystalline orientation of the thin films. The source and detector angles are synchronized to each other, so that Bragg condition is always satisfied for the plane parallel to the surface of the film. As the angle of the incident X-ray beam is varied, the detector will pick up the constructive interference of the reflected X-rays when an angle corresponding to the crystalline lattice spacing of any family planes in the sample is reached. *c*-axis orientated thin

film corresponds to when only one family of planes, i.e. (00*l*), satisfies the Bragg condition during the θ-2θ scan. The degree of *c*-axis orientation can be determined with a rocking curve. By fixing the detector angle to the value for the (001) crystalline plane, i.e. $2\theta_{001}$, the source angle can be varied by as much as two degrees around $2\theta_{001}$. The full width at half maximum (FWHM) of the resulting peak thereby gives an indication of the degree *c*-axis orientation of the crystal. To determine the expitaxy of the films, ϕ scans need to be performed. Most of the films that were studied in this work have approximately cubic structure. There are small distortions in the cubic structures of some films, which induce tetragonal, orthorhombic, or rhombohedral crystal structure. A cubic structure can be assumed for simplicity in each case. For a *c*-oriented cubic crystal, for example, the sample could be tilted for example to the (101) family of planes in order to reveal the in-plane character of the film. The tilted angle χ is determined by:

$$\cos\chi = (h_1h_2 + k_1k_2 + l_1l_2)/[(h_1^2 + k_1^2 + l_1^2)(h_2^2 + k_2^2 + l_2^2)] \qquad \text{Eq.2. 2}$$

where (h_1, k_1, l_1) are the indices of the crystalline direction normal to the sample and (h_2, k_2, l_2) are the indices of the family of planes of interest.

Therefore, $\chi = 45°$ in order to tilt from (001) plane to (101) planes. The ϕ scans would display four-fold symmetry peaks corresponding to (101), $(10\bar{1})$, (011), and $(0\bar{1}1)$ for the expitaxial films with a cubic structure.

X-ray diffraction characterization of the films in this dissertation was conducted by using Cu K_α radiation in a Siemens D5000 four-circle diffractometer. θ-2θ scans, rocking curves and ϕ scans were performed in the XRD studies.

2.2.2 Transimission electron microscopy

Extensive transmission electron microscopy (TEM) was performed to characterize the microstructures of the films in this dissertation. The morphological, crystallographic features as well as chemical information in the films have been provided. The microscopes that were used in this study include a JOEL 4000FX operated at 300 KV, a CM300 operated at 300 KV and a CM200 operated at 200 KV.

A TEM operates similarly to an optical microscope, except optical microscopes use light sources and focus light beams with glass lenses, while TEMs use electron sources and focus electron beams with electromagnetic lenses[74]. The electrons emitted from the filament are accelerated by a high voltage (100 kV – 1000 kV) and focused through a set of condenser lenses (electromagnetic lenses) onto the specimen. The electron beam is scattered by the specimen. The diffracted beams are then brought to focus by the objective lens on its back focal plane and form a diffraction pattern. A final TEM image or diffraction pattern can be produced on the fluorescent viewing screen by a series of objective lens, intermediate lens and projector lens. The main imaging and diffraction techniques include: 1. conventional imaging (bright-field and dark-field TEM); 2. electron diffraction (selected area electron diffraction, SAD); 3. convergent-beam electron diffraction (CBED); 4. phase-contrast imaging (high-resolution TEM, HRTEM); 5. Z-contrast imaging. Besides diffraction and spatial imaging, the high-energy electrons in TEM cause electronic excitations of the atoms in the specimen. Two important spectroscopic techniques make use of these excitations, i.e. energy-dispersive x-ray spectroscopy (EDS) and electron energy-loss spectroscopy (EELS). In this dissertation, the conventional bright-field and dark-field imaging, SAD, HRTEM and EDS are used to

study the microstructures of the films. For a reference to different TEM techniques see the reference by B. Fultz and J. Howe[74].

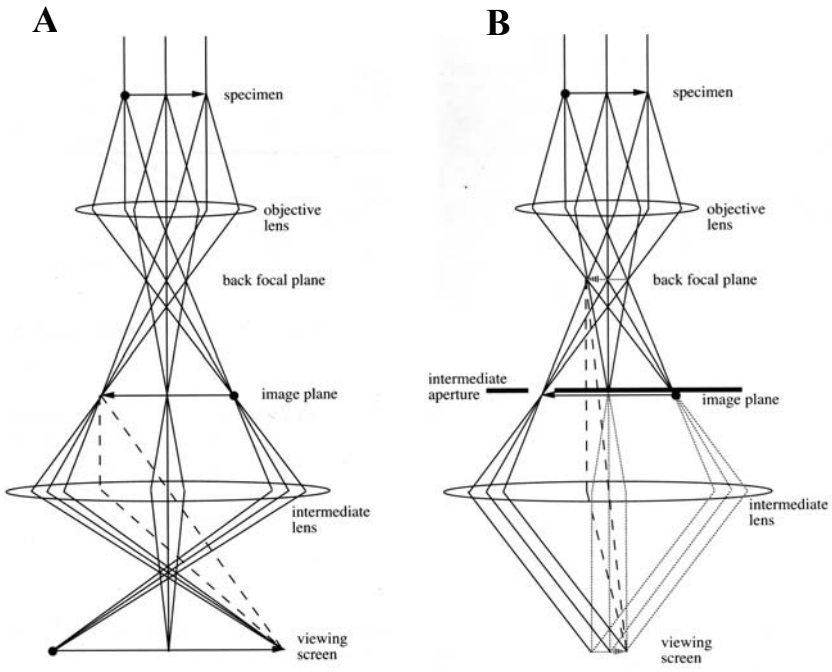

Fig.2.2 The two basic operation modes of the TEM imaging system: diffraction mode (left) and imaging mode (right).

Fig.2.2 shows two basic operation modes of the TEM imaging system: diffraction mode and imaging mode. By changing the focal length of the intermediate lens, diffraction mode and imaging mode can be easily obtained in the TEM. In the diffraction mode, the image plane coincides with the back focal plane of the objective lens; while in the image mode, the image plane coincides with the image plane of the objective lens. The artificial dashed lines in the Fig.2.2 show the intermediate lens is focus on different plane of the objective lens.

In SAD mode, a second aperture, an “intermediate aperture” is positioned in the image plane of the objective lens, which is to confirm that the diffraction pattern is

produced by a selected area of the specimen. As it is shown in Fig.2.2, the SAD pattern that appears on the viewing screen (left side of figure) originates from the area selected in the image mode (right side of the figure, the tip of the solid arrow). The separation of the diffraction spots on the viewing screen can be used to determine the interplanar spacings in the crystal.

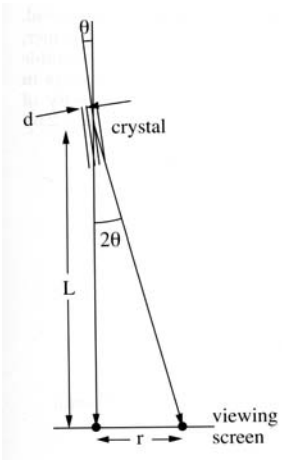

Fig.2.3 Geometry for electron diffraction, L is the camera length.

Consider the geometry of a selected area diffraction pattern in Fig.2.3. According to Bragg's law, we can get:

$$2d\sin\theta = \lambda \qquad \text{Eq.2.3}$$

Since θ ~ 1º for low order diffractions from most materials, we can assume:

$$\sin\theta \sim \tan\theta \sim \frac{1}{2}\tan(2\theta) = \frac{r}{L} \qquad \text{Eq.2.4}$$

Substitute Eq.2. 4 into Eq.2. 3, we get:

$$rd = \lambda L \qquad \text{Eq.2.5}$$

Eq.2.5 is the "camera equation", where λL is known as the "camera constant". It

allows us to determine an interplanar spacing, *d*, by measuring the separation of diffraction spots, *r*.

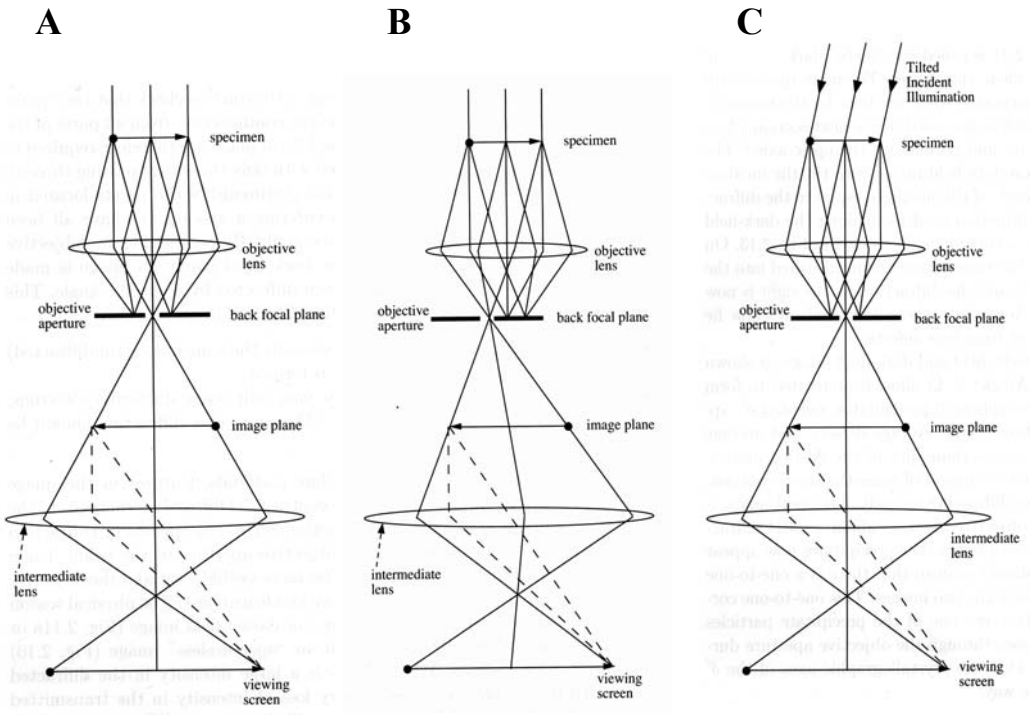

Fig.2.4 Schematic of various imaging modes of the TEM imaging system. A. Bright-Field (BF) image mode; B. Dark-Field (DF) image mode; C. Axial Dark-Field (DF) mode, minimizing blurring from lens defects.

In the simple imaging mode (see Fig.2.2A), the specimen shows little contrast. To increase the contrast objective apertures are inserted at the back focal plane of the objective lens in the conventional imaging mode, which is called diffraction contrast. When the aperture is positioned to allow only the transmitted (undiffracted) electrons to pass, a bright-field (BF) image is formed, illustrated in Fig.2.4A. When the aperture is positioned to allow only some diffracted electrons to pass, a dark-field (DF) image is formed, shown in illustrated in Fig.2.4B. Since magnetic lenses are far from ideal thin lenses, the more rays tilt away from the optic axis, the less accurately they are

bent by the magnetic lens. Therefore, it is always better to keep rays close to and parallel to the optic axis. For this purpose, the incident beam is tilted by the Bragg angle, $2\theta_B$, of the beam of interest in order to make a high-resolution dark-field image and minimize image blurring from lens defects. This imaging mode is called axial dark-field image mode, see Fig.2.4C.

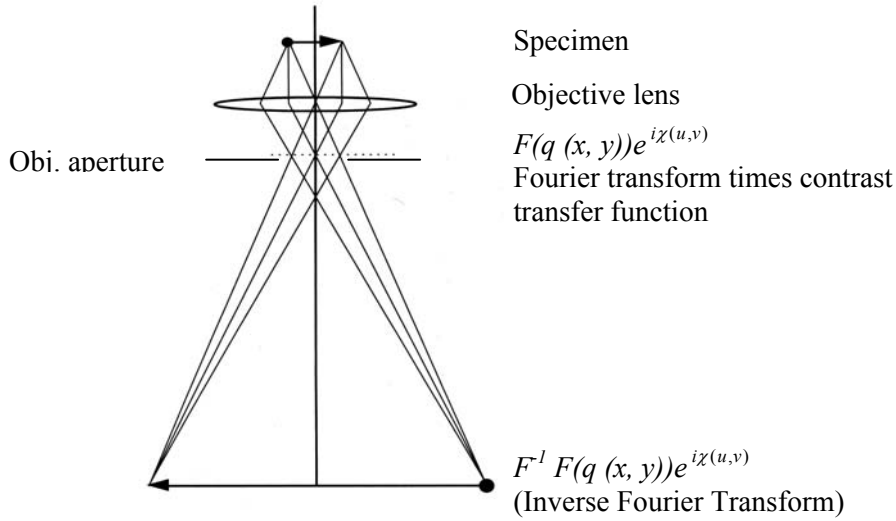

Fig.2.5 Fourier transforms and planes of a ray diagram. The function accounts for the characteristics in the objective lens.

The conventional bright-field and dark-field image cannot be used to form the "high-resolution" HRTEM image of columns of atoms. The HRTEM image is obtained when two or more diffracted beams are included in the objective aperture for the image formation. The image is an interference pattern between the forward-scattered and diffracted electron waves from the specimen. The diffracted wave, in this case an electron wavefunction, is the Fourier transform of the scattering factor distribution in the material. The phase of the waves at the electron wavefront is important for interference pattern. The specimen is approximated as a phase object that provides phase shifts to the electron wavefront. The absorption by the sample can

be neglected since the HRTEM sample is normally very thin, so the scattering of electrons by the sample only causes a phase change of the wave function. The HRTEM image is, therefore, called the phase contrast image. HRTEM images are best understood in terms of Fourier transforms. Fig.2.5 shows how Fourier transforms of the diffracted electron waves correspond to the specimen, the back focal plane of the objective lens, and the image plane.

The transmission function of the object can be expressed as:

$$q(x,y) = e^{i\sigma\varphi(x,y)\Delta z} \qquad \text{Eq.2.6}$$

where σ is the interaction constant, $\varphi(x, y)$ is the projected potential of the object along the z (optic) axis, and Δz is the sample thickness. As shown in Fig.2.5, the amplitude at the back focal plane of the objective lens is the combination of Fourier transform (F) of the transmission function of the object and the contrast transfer function of the objective lens. It can be expressed as:

$$\psi(u,v) = F(q(x,y))e^{i\chi(u,v)} \approx \delta(u,v) + iF(\sigma\varphi(x,y)\Delta z) \qquad \text{Eq.2.7}$$

where $e^{i\chi(u,v)}$ is the contrast transfer function of the objective lens. It stands for the phase change of the electron wave function caused by the objective lens. $\chi(u,v)$ can be expressed as:

$$\chi(u,v) = \pi\{\Delta f\lambda(u^2+v^2) - 0.5C_s\lambda^3(u^2+v^2)^2\} \qquad \text{Eq.2.8}$$

where Δf is the defocus value, C_s is the spherical aberration of the objective lens, and u, v are the coordinates in the back focal plane.

By taking account of the objective aperture, the amplitude at the image plane is:

$$\varphi(x,y) = F(C(u,v)\psi(u,v)) \qquad \text{Eq.2.9}$$

where $C(u,v)$ is the aperture function of radius r given by:

$C(u, v) = 1$ when $\sqrt{u^2+v^2} \le r$

$C(u, v) = 0$ when $\sqrt{u^2 + v^2} > r$ Eq.2.10

Therefore, the intensity at the image plane is:

$$\begin{aligned} I(x,y) &= \varphi^*(x,y)\varphi(x,y) \\ &= \left|1 + iF(C(u,v)F(iF\sigma(\varphi(x,y)\Delta z)e^{i\chi(u,v)})\right|^2 \\ &\approx 1 \pm f(\sigma, \Delta f, C_s, \lambda, r, \Delta z)\sigma\varphi(x,y)\Delta z \end{aligned} \quad \text{Eq.2.11}$$

It can be seen from the above equation that a phase contrast image is a direct reflection of the projected crystal potential $\varphi(x, y)$. And, it depends on many parameters, such as the defocus value Δf, the sample thickness Δz, and the spherical aberration of the objective lens C_s. Interpretations of high-resolution images involve image simulation making models of the structure of the specimen, taking into account the constant of the microscope and the conditions (Δf) used to take the HRTEM image, and fitting these models to the experimental image.

2.2.3 TEM sample preparation

Since electrons scatter very strongly by the atomic electronic potential of the sample, extremely thin samples (< 1 μm) are required for TEM characterization. Both cross-section and plan-view specimens were prepared for TEM observation in this dissertation. For a cross section sample, the transmitted electron beam is perpendicular to the film growth direction, while for a plan view sample the transmitted electron beam is parallel to the film growth direction. A tripod polishing method[75] was used for the preparation of both cross-section and plan-view samples.

The preparation process for a plan-view sample is much simpler than that of a cross-section sample. The cross-sectional TEM specimen preparation involves several steps. The first step is to cut off two pieces of ~1 mm × 5 mm from the 5 mm × 5 mm sample by using a diamond saw or cleave by using a diamond scriber. Then the two

pieces of sample are glued together with the film side facing each other using M-bond 610 adhesive. Subsequently, the glued sample is mounted on a tripod polisher holder with acetone dissolvable wax. The glued sample is mechanically thinned from both sides across the glued interface using diamond lapping paper. The mechanical polishing includes polishing using 30 μm, 9 μm, 3 μm and 1 μm diamond lapping paper step by step and final fine polishing using 0.05 μm silica suspension on texture. The finished polished sample is in wedge shape with the thinner side close to a thickness of less than a few microns. The sample is detached from the holder by dipping the sample with L bracket into acetone. After the sample de-attached from the holder, it is then glued on a slotted copper grid with the thinner edge at the center of the slot. If the sample is not electron transparent after mechanical polishing it is ion-milled for a short time (20~40 min).

It is very important to be able to determine the thickness of the sample, to know when to stop the polishing. The tripod polishing method takes advantage of the angle polishing concept to monitor the sample thickness. Initially, a larger angle (~5°) is used until an edge appears at the sample. Then, the polishing angle is changed to a smaller angle (~1°) for fine polishing. Thus, a shadowed area is created in front of the sample. The sample is polished until the shadow area disappears. The process is schematically shown in Fig.2.6. Thus, the specimen prepared by tripod polisher is in a wedged shape with one extremely thin edge (less than 1 μm, ideally). However, the whole sample is still thick enough to avoid mechanical damages. The supporting copper grid can also be used to assist monitoring the sample thickness. The specimen can be glued on the copper grid holder at the final polishing step. Because of the wedge polishing, one side of the sample is thinner than the other side. When copper

grid is polished it changes color. The sample edge close to the changed color side of the copper grid will be very thin.

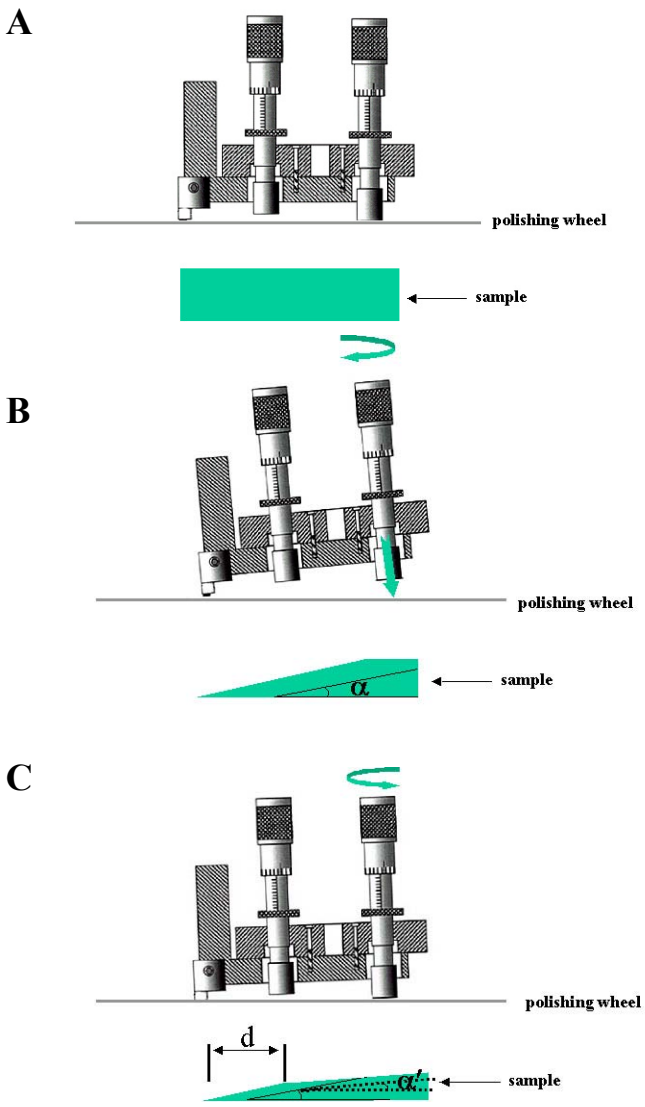

Fig.2.6 Schematic of tripod angle polishing. (a) The glass holder is flat polished before the sample is attached; (b) Sample is polished with a large angle, $\alpha = 5°$; (c) Sample is polished with a small angle, $\alpha' = 1°$. A shadow area of width d creased from the cross section, which is the width of the wedge polished at 5°C.

One of the main advantages of the tripod polishing is the reduced time required for thinning the sample compared to dimpling and ion milling method. Two or three TEM specimens can be prepared within a day, which is much faster than the traditional polishing. Another advantage is the short or no ion milling, which translates into less damage to the specimen.

2.3 Electric measurement

Ferroelectric measurements were performed using a commercial RT6000 test system (Radiant Technologies, USA). Fig.2.7A shows the schematic of the electric set up used for this study. It consists of an Analog Data Precision model 2020 programmable pulse generator with an internal impedance of 50 Ω. A series of pulses is programmed so that a hysteresis loop (Fig.2.8) is generated when the pulse train traverses the test ferroelectric capacitor. The pulse sequence shown in Fig.2.7B is called PUND pulse series[76]. Switched (P^*) and non-switched ($P^\wedge$) polarization was obtained for each test capacitor and the difference gives the polarization from ferroelectric domain switching ($P=P^*-P^\wedge \approx 2P_r$).

An HP 4192 impedance/gain analyzer was used to measure the dielectric properties. A small signal with 50~100 mV amplitude and various frequencies was applied to the test capacitors while a dc field was swept from positive bias to negative bias and back again, i.e., –10 V ~ +10 V. The small signal capacitance was recorded and the dielectric constant was evaluated using:

$$\varepsilon = \frac{Cd}{4\pi\varepsilon_0 A} \qquad \text{Eq.2.12}$$

where ε is dielectric constant, ε_0 is the dielectric constant in free space, C is the capacitance, A is the area of the capacitor and d is the film thickness.

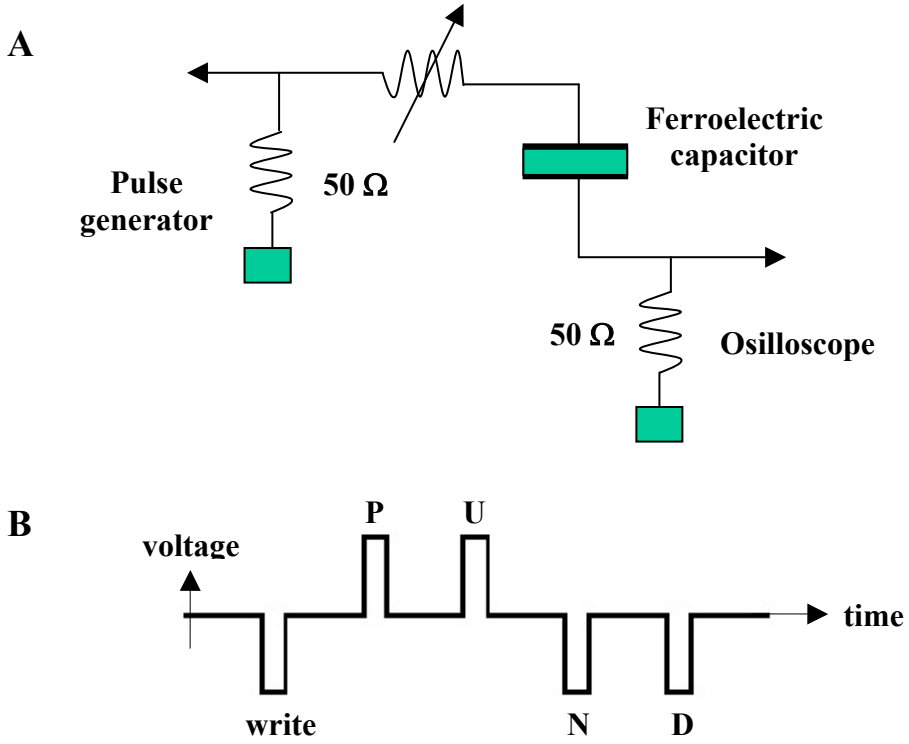

Fig.2.7 Schematic of the experimental set-up for ferroelectric measurements. A. Schematic of electric set-up; B. Pulse train for switching measurements.

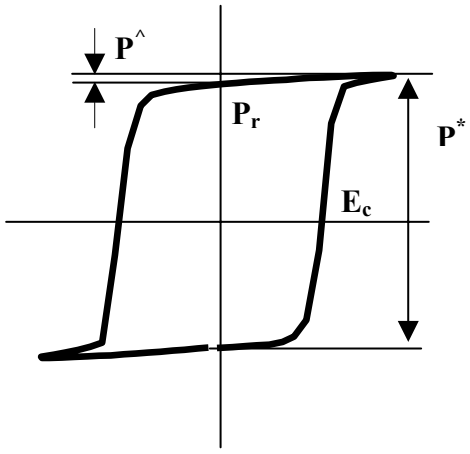

Fig.2.8 A typical ferroelectric hysteresis loop. P^* switched polarization, $P^{\wedge}$ non-switched polarization, P_r remanent polarization, and E_c coercive field.

Piezoelectric measurements were carried out using a technique based on AFM set up [77, 78, 79]. Both "piezo response" domain imaging and quantitative d_{33} measurements were conducted. A schematic experimental setup for these techniques is illustrated in Fig.2.9. An external voltage with a frequency ω was applied through the tip, which causes the ferroelectric sample under the electric field to vibrate at the same frequency due to the converse piezoelectric effect. This vibration then forces the AFM tip to oscillate, and the modulated deflection signal is detected using the lock-in amplifier. During measurement, the frequency of the applied voltage was much lower than the cantilever resonant frequency in order to avoid mechanical resonance of the cantilever.

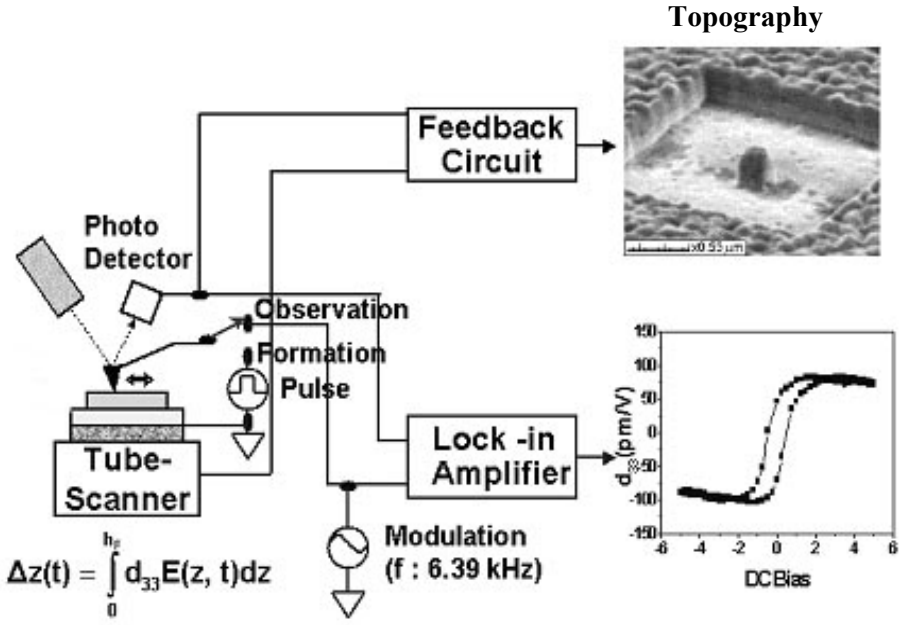

Fig.2.9 Schematic of the experimental setup for piezoelectric measurements.

In piezoelectric imaging, the voltage is applied through the conducting tip, which is used as a movable top electrode. By scanning along the sample surface, the domain configuration of the sample can be mapped out.

In a quantitative d_{33} measurement, the voltage is applied on the capacitor through the tip to Pt top electrode. This ensures a homogenous electric field under the electrode; it also prevents the build up of electrostatic interaction between the cantilever and the sample. We used standard silicon tips coated with a Pt/Ir alloy for electrical conduction. The typical force constant of these tips was 5 N/m, and the resonance frequency (as specified by the manufacturer) was 60-80 KHz. The contact force was ~ 70 to 100 nN. The measurement frequency used was 6.39 KHz. Each capacitor was driven at particular DC voltage to study the field dependence.

2.4 Magnetic measurement

2.4.1 Vibration Sample Magnetometer

A Vibrating Sample Magnetometer (VSM) was used to measure the magnetic properties of the films. The principle of this measurement is very simple. When a sample is placed in a homogenous magnetic field, a magnetic moment is induced in the sample. If this sample is made to undergo sinusoidal motion (i.e. mechanically vibrated), the vibration induces a magnetic flux change. This in turn induces a voltage in the pick-up coils. The magnetic moment determined by the VSM is related to the magnetization of the sample, its susceptibility. Fig.2.10 shows a typical VSM set up. The sample is suspended from a vibrating drive head by a non-magnetic rod and placed between two electromagnets which produce a magnetic field. The vibrator generates a vertical sinusoidal vibration with a frequency of 82 Hz. Therefore, the sample experiences sinusoidal motion, which induces an electrical signal in the coils mounted on the pole faces of the electromagnets. The signal picked up by the coils is proportional to the frequency and amplitude of the sinusoidal motion, and the total

magnetic moment of the sample at the applied magnetic field. The frequency and amplitude of the sinusoidal motion are maintained constant by a capacitor (reference signal generator). By feeding the signals from the pick-up coils and the reference signal into a demodulator, the magnetic moment of the sample is extracted.

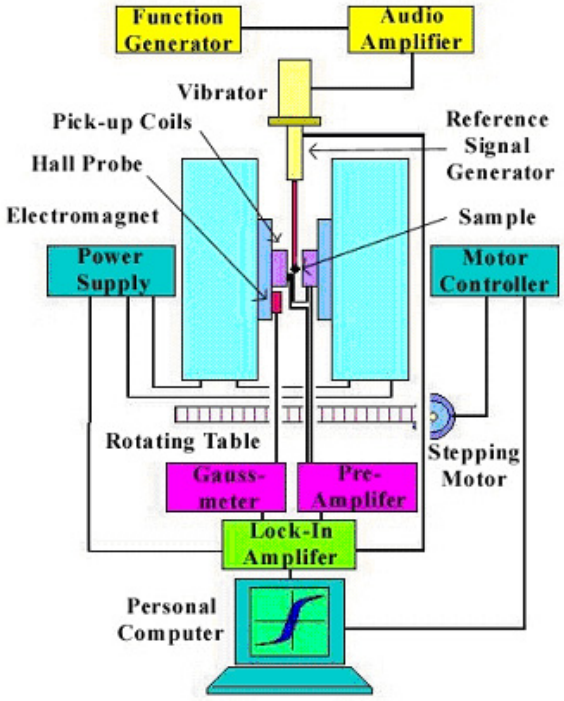

Fig.2.10 Schematic diagram of VSM system.

VSM provides a fast and easy technique for the measurement of the magnetic properties of a material. Furthermore, VSM has a high temperature capability. The M vs T measurements in this dissertation were conducted using VSM. However, the resolution (10^{-5} ~ 10^{-7} emu) is low compared with Superconducting Quantum Interference Device (SQUID) Magnetometer. For the thin film sample with signal smaller than 10^{-5} emu, SQUID is preferred. Most of the hysteresis loop data included in this dissertation were measured by SQUID. One reason is the small signal

generated by the thin film samples. Another reason is the limitations of magnetic field that our VSM supplied (7000 Oe max in VSM compared with – 5 T ~ + 5 T from SQUIDs). The multiferroic thin films nanostructures have large coercivity and anisotropy field. The VSM measurements normally gave small loops of the sample.

2.4.2 Superconducting Quantum Interference Device Megnetometer

SQUIDs are the most sensitive devices in the detection of magnetic flux. The resolution threshold for SQUID is ~10^{-14} T. A Superconducting Quantum Interference Device (SQUI D) uses the properties of electron-pair wave coherence and Josephson Junctions to detect very small magnetic fields.

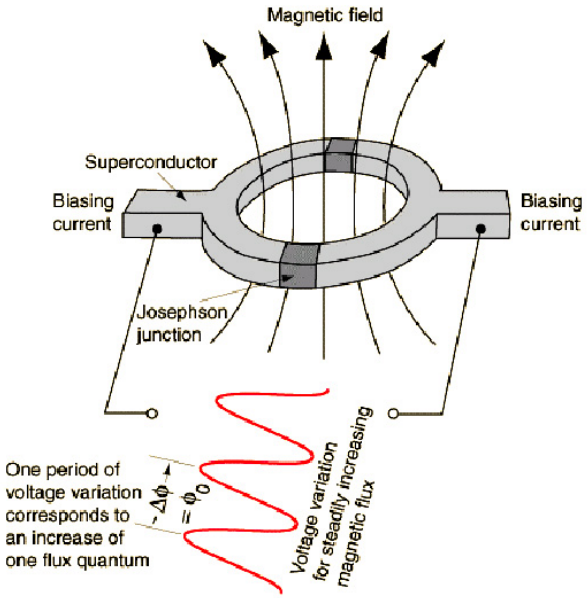

Fig.2.11 A Josephson device, which consists of two superconductors separated by thin insulating layers to form two parallel Josephson junctions.

The central element of a SQUID is a Josephson tunneling junction device, which acts as a flux-to-voltage transducer. A Josephson junction device consists of a

superconducing coil that is broken by one (RF SQUID) or two (DC SQUID) insulating layers. With no insulating layer flux cannot enter the superconducting ring. If the layer is too thick no supercurrent can flow. The superconductors separated by a thin insulating layer can experience electron tunneling through the junction. The presence of the insulating layer typically restricts the value of the supercurrent flowing in the coil to less than 10^{-5} A. Fig.2.11 shows a SQUID Josephson device with two parallel Josephone junctions.

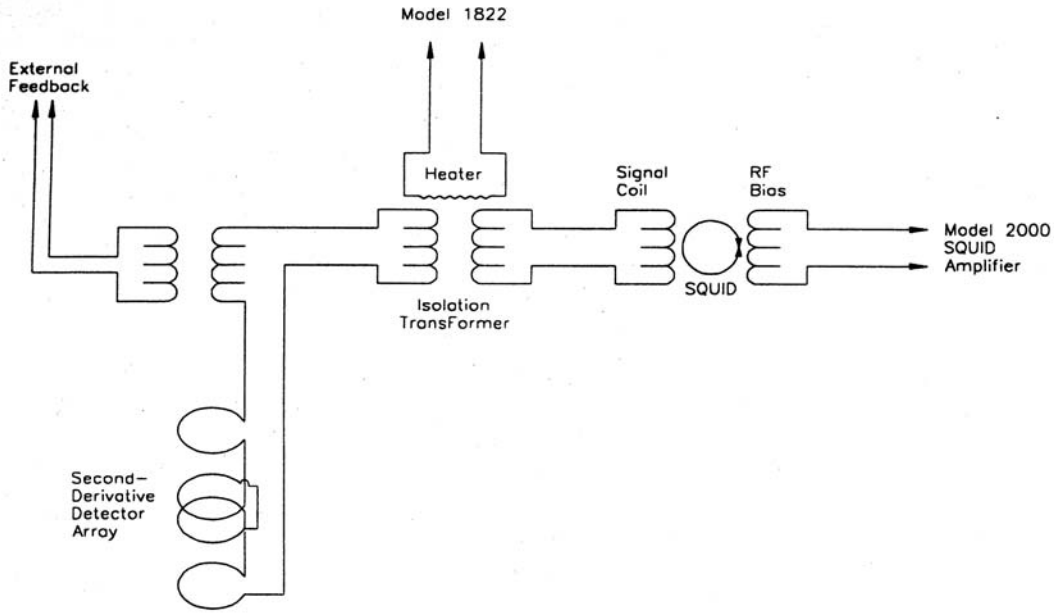

Fig.2.12 Schematic of a SQUID system.

The SQUID magnetometer utilizes the sensitivity of the SQUIDs and superconducting loops to an external magnetic field. Fig.2.12 is a schematic diagram of SQUID detection system. A set of superconducting sensing loops acts as detection gradiometer coils. They are accurately balanced and arranged in a configuration that only detects the magnetic flux induced by the magnetization of the sample (i.e. expels the uniform field applied to the sample by the superconducting magnet). As the

sample moves through the coils, the magnetic moment of the sample induces an electric current in the detection coils. Since the coils, the connecting wires and the SQUID input coil form a closed superconducting loop, this current is not damped so that any change in magnetic flux in the detection coils produces a proportional change in the persistent current in the detection circuit.

2.4.3 Magnetic Force Microscopy

Magnetic Force Microscopy (MFM) was used to observe the local magnetization near the sample surface. Like an AFM, a sharp probe is attached to the bottom of a cantilever. As it is scanned over the sample surface a laser is bounced off the top of the cantilever. In MFM, however, the probe must have a magnetized tip. The magnetic probe is standard silicon cantilever (or silicon nitride cantilever) coated with a magnetic thin film. The interaction of the tip with various magnetic domains on the surface results in cantilever deflection. The microscope can sense the deflection of the cantilever, which will result in a force image in a static mode. Or, it can sense the resonance frequency change of the cantilever, which will result in a force gradient image. A mapping of the magnetic forces or force gradients above the sample surface can be achieved when a sample is scanned under the tip.

Therefore, MFM is a variation of the Atomic Force Microscope (AFM), capable of providing images of magnetic domains. The mode of operation is essentially non-contact imaging. The force gradient (F′) detected contains information from both the surface structure and surface magnetization:

$$F' = F'_{surface} + F'_{magnetic} \qquad \text{Eq.2.13}$$

where $F'_{surface}$ is the surface component of the gradient and $F'_{magnetic}$ is a magnetic component of the gradient. Signals from surface topography dominate at a distance close to the surface while, at a distance further away from the surface (typically beyond 100 nm), the magnetic signal dominates. Consequently, depending on the distance between the surface and the tip, normal MFM images may contain a combination of topography and magnetic signals. Topographic and magnetic details from the same scan can be related to each other. However, methods have been developed to separate topography and magnetic features, which allow pure magnetic images to be achieved.

MFM is capable of imaging magnetic domains of several tens of nanometers. The fact that no sample preparation is necessary and that a lateral resolution of 10~50 nm is achievable make it a powerful tool for investigation of magnetization nanostructures.

Chapter 3 Multiferroic $BaTiO_3$-$CoFe_2O_4$ nanostructures

3.1 Introduction

Nanostructured materials have recently attracted considerable attention for fundamental scientific exploration as well as various applications. They have shown significant promise in a wide range of applications in electronic, optoelectronic and magnetic devices. The typical scale for nanostructures is less than 100 nm along one or more of the dimensions. To achieve the nanometer-scale features, advanced sample growth and patterning techniques beyond the capabilities of conventional photolithography are necessary. An enormous number of techniques have been developed to fabricate nanostructures. First of all, advanced lithographic techniques that use radiation with much smaller wavelength have been developed. These methods include electron beam (E-beam) lithography[80], x-ray lithography with synchrotron light sources[81], and focused ion beam[82] and atom beam lithographies[83]. Such techniques yield lateral resolution down to a few tens of nanometers and offer almost infinite design variations. However, these techniques involve a high number of technological processes and high costs of equipment.

A technique based on the scanning probe microscope (SPM) has been developed as an alternative to the concept of optical lithography. Atomic scale nanostructures are achieved by either manipulating single atoms[84] or by using the SPM tip as a stylus or pen to "write" nanoscale structures on a substrate[85]. Although the "writing speed" of these procedures has been greatly increased, long processing time is still the main drawback of this technique.

The formation of nanostructured materials by self-assembly is an attractive method. In contrast to the artificially ordered schemes, the process of self-assembly holds promise to enable the creation of complex, next generation device architectures that would rely on the system's intrinsic ability to organize itself into ordered patterns. Thus, the formation of nanostructures through self-assembly has been a topic of recent experimental and theoretical study.

The concept of spontaneous nanostructure formation has been extensively studied in metals[86,87,88,89] and in semiconductor systems[90,91,92,93,94,95]. Considerable research has been conducted on the self-organization of nanostructures on semiconductor surfaces during epitaxial growth. Nanostructures can form by surface reactions[96] during epitaxial growth and even during erosion of surfaces by ion bombardment[97]. The spontaneously formed nanostructures can be categorized into five classes[90] as shown in Fig.3.1. These nanostructures are periodically faceted surfaces (Fig.3.1A), periodic structures of planar domains, e.g. monolayer high islands (Fig.3.1B), ordered arrays of three-dimensional coherently strained islands in lattice-mismatched heteroepitaxial systems (Fig.3.1C), multisheet arrays of two-dimensional islands (Fig.3.1D), and multisheet arrays of three-dimensional islands (Fig.3.1E).

Fig.3.1 E presents a particular interesting mode of self-organized growth. Structures with such organization were reported in InAs on GaAs (100)[98], $PbSe/Pb_{1-x}Eu_xTe$ ($x \sim 0.05$ to 0.1)[99] and other systems. It was observed that dots from successive layers show a tendency to stack vertically due to lateral modulation of strain. The initial 2D in-plane self-assembly therefore evolves progressively into 3D self-organization. The in-plane self-organization can also lead to the formation of the nanopillar structures, which is observed in Co-C films on Si[100], Co pillars on

Au(111)[101], α-Fe nanowires in $La_{1-x}Sr_xFeO_3$ matrix films[102], 3-D nanoscale columns of La-Ca-Mn-O embedded in an MgO matrix[103], etc. These bottom-up nanostructures are particularly interesting for high-density data storage as well as other magnetic device applications. In this work, we report the growth processing conditions and properties of $BaTiO_3$-$CoFe_2O_4$ nanostructure thin films that are vertically aligned through self-organization.

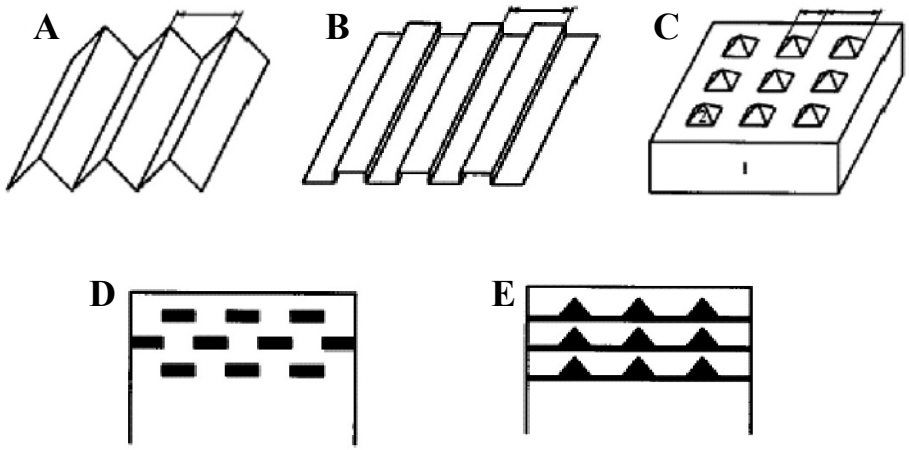

Fig.3.1 Five classes of spontaneously ordered nanostructures[90]: A. periodically faceted surfaces; B. surface structures of planar domains; C. ordered array of three-dimensional coherently strained islands lattice-mismatched to the substrate 1; D. cross-sectional scheme of a multisheet array of two dimensional islands; E. cross-sectional scheme of a multisheet array of three-dimensional islands.

Although fabricating vertically aligned nanostructures by self-assembly is not a completely new idea, it is a challenge to synthesize such nanostructures in complex oxides. Little work has been reported on self-organized vertically aligned nanostructures in complex oxides. Furthermore, the mechanism of the in-plane self-

organization in the simplest semiconductor thin film system, i.e., AB system, is still not clear.

In this chapter, the formation of $BaTiO_3$-$CoFe_2O_4$ nanostructures by self-assembly is reported. The thermodynamics and kinetics of the growth of $BaTiO_3$-$CoFe_2O_4$ nanostructures are discussed. This study includes the dependence of nanostructures on substrate temperature, growth rate, and film thickness as well as the effect of lattice mismatch strain with the substrate and the effect of annealing on the nanostructures. The $BaTiO_3$-$CoFe_2O_4$ nanostructure is a model system in which two complex oxides spontaneously separate and form nanostructures during heteroepitaxial growth.

3.2 Three-dimensional heteroepitaxy in self-assembled $BaTiO_3$-$CoFe_2O_4$ nanostructures

The formation of three-dimensional heteroepitaxy in $BaTiO_3$-$CoFe_2O_4$ involves two aspects. The first is the intrinsic similarity in crystal chemistry between perovskites and spinels, both of which have octahedral oxygen coordination. This leads to crystal lattice parameters that are reasonably commensurate. At room temperature, $BaTiO_3$ has a perovskite structure with lattice parameters of a = 0.399 nm and c = 0. 404 nm, while $CoFe_2O_4$ has a spinel structure with a lattice parameter of a = 0.838 nm or approximately twice the basic building block of $BaTiO_3$. There is a ~5% lattice mismatch between the two structures. The second key aspect is the fact that although many of these complex oxides can accommodate considerable cationic solid solution solubility, the perovskite/spinel system behaves like line compounds. In other words, these compounds have very little solid solubility into each other. These two aspects present an interesting opportunity to create perovskite-spinel

nanostructures through a spontaneous phase separation process. The two phases in the nanostructure can be epitaxial simultaneously with respect to each other as well as with respect to a common substrate. By selecting a suitable substrate with similar crystal structure, such as $SrTiO_3$, we present the tantalizing possibility of heteroepitaxy in three-dimensions (i.e. both in-plane as well as out-of-plane) in the film. Fig.3.2 shows a schematic of three-dimensional heteroepitaxy of spinel $CoFe_2O_4$ (top left) and perovskite $BaTiO_3$ (top right) on a perovskite substrate (bottom).

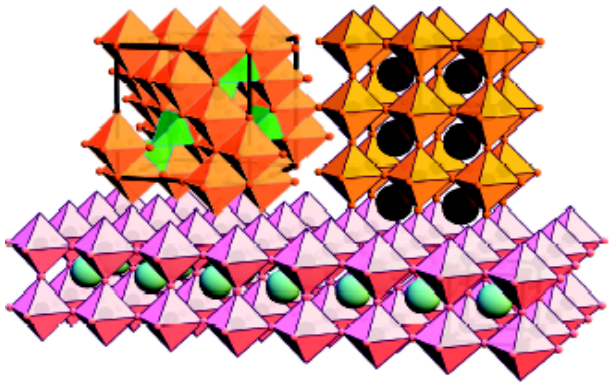

Fig.3.2 Schematic of three-dimensional heteroepitaxial growth of spinel $CoFe_2O_4$ (top left) and perovskite $BaTiO_3$ (top right) on a perovskite substrate.

To achieve $BaTiO_3$-$CoFe_2O_4$ nanostructures by self-assembly, a single target with molar ratio of 62:48 ($BaTiO_3$:$CoFe_2O_4$) was used during the PLD growth process. (001) $SrTiO_3$ substrates with and without a $SrRuO_3$ bottom electrode were used. For these particular studies the films were deposited at 920~950 ºC.

A typical X-ray θ-2θ diffraction spectrum (Fig.3.3A) of the film shows that the film has (00*l*) oriented structure with high crystallinity. Fig.3.3A contains four sets of diffraction peaks that can be assigned, respectively, to (00*l*) spinel $CoFe_2O_4$ and (00*l*) perovskite $BaTiO_3$ in addition to (00*l*) reflections from the $SrTiO_3$ substrate

and (00*l*) reflections from $SrRuO_3$ bottom electrode. The observation of distinct peaks for $BaTiO_3$ and $CoFe_2O_4$ indicates that the two phases coexist in the film. The ϕ-scans of the (202)-peak of $BaTiO_3$ phase and (404)-peak of $CoFe_2O_4$ phase in the film as well as (202)-peak of $SrTiO_3$ and (202)-peak of $SrRuO_3$ are presented in Fig.3.3B. The four-fold symmetry indicates a "cube-on-cube" epitaxy of both $BaTiO_3$ and $CoFe_2O_4$ on $SrRuO_3/SrTiO_3$, as well as an in-plane epitaxy between the two phases in the film. Therefore, $CoFe_2O_4$ and $BaTiO_3$ have been spontaneously separated into two phases during deposition. And, the films have three-dimensional epitaxial relationships between the two phases in the film as well as with respect to the substrate.

Atomic force microscopy (AFM) image (Fig.3.4A) shows a very interesting morphological microstructure consisting of a nearly periodic pattern. The statistical size distribution of the features (Fig.3.4B) shows that about 94% of the features are within the range of 25~35 nm. Transmission electron microscopy (TEM) studies resolve the features to be arrays of vertical $CoFe_2O_4$ pillars with 20-30 nm diameters embedded in a $BaTiO_3$ matrix. TEM plan view images (Fig.3.5A) show that the $CoFe_2O_4$ nanopillars are homogeneously distributed in the $BaTiO_3$ matrix. The volume fraction of the nanopillars calculated from the plan view TEM image is about 40%, which is in agreement with the 38% fraction of $CoFe_2O_4$ in the target. The selected area diffraction (SAD) pattern (Fig.3.5B) shows the in-plane epitaxial relationship of the two phases, which is consistent with the XRD results. High resolution TEM images illustrate that all the pillars are single crystalline with sharp interfaces with the matrix. Fig.3.5C is a high resolution TEM image of an individual $CoFe_2O_4$ pillar embedded in the $BaTiO_3$ matrix. A periodic dislocation array was found at the interface (Fig.3.5D), which relaxes the lattice mismatch strain between

the two phases. It is interesting to note that the nanopillars have fairly circular cross section with small microfaceting even at the high growth temperature of 920 ºC. Faceting does not occur in this system because of the increase in interfacial energy that would be produced by sharp corners.

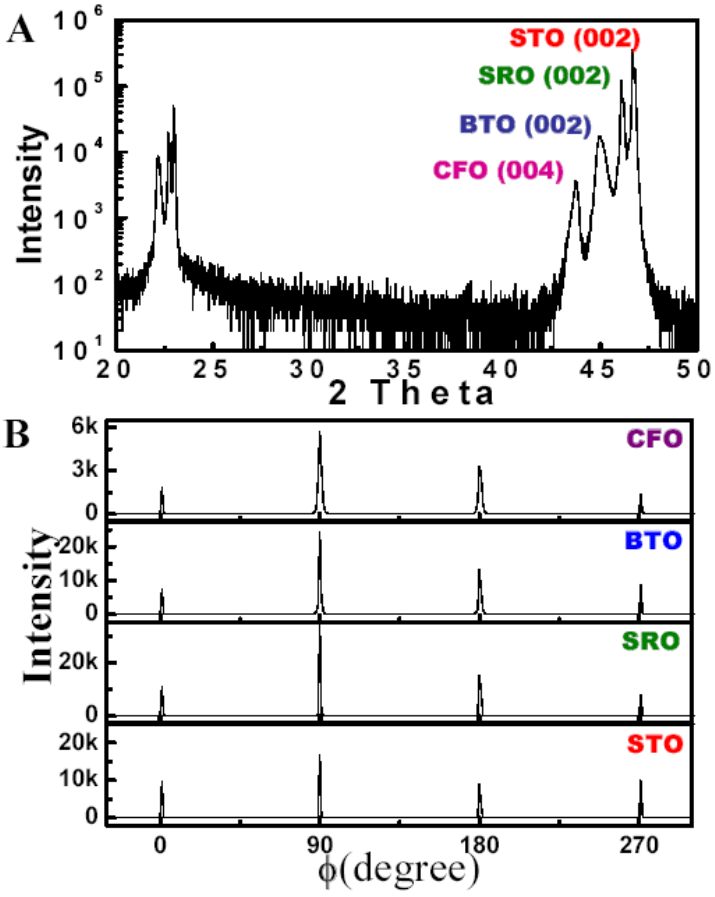

Fig.3.3 XRD spectra from a film grown at 920 °C with a thickness of 400 nm. A. X-ray θ-2θ scan showing (00*l*) families of peaks, which can be assigned to $CoFe_2O_4$ (CFO), $BaTiO_3$ (BTO), $SrRuO_3$ (SRO) and the $SrTiO_3$ (STO) substrate. B. ϕ-scans using (202) reflection of $BaTiO_3$, (404) reflection of $CoFe_2O_4$, (202) reflection of $SrRuO_3$ and (202) reflection of $SrTiO_3$ substrate from the same sample.

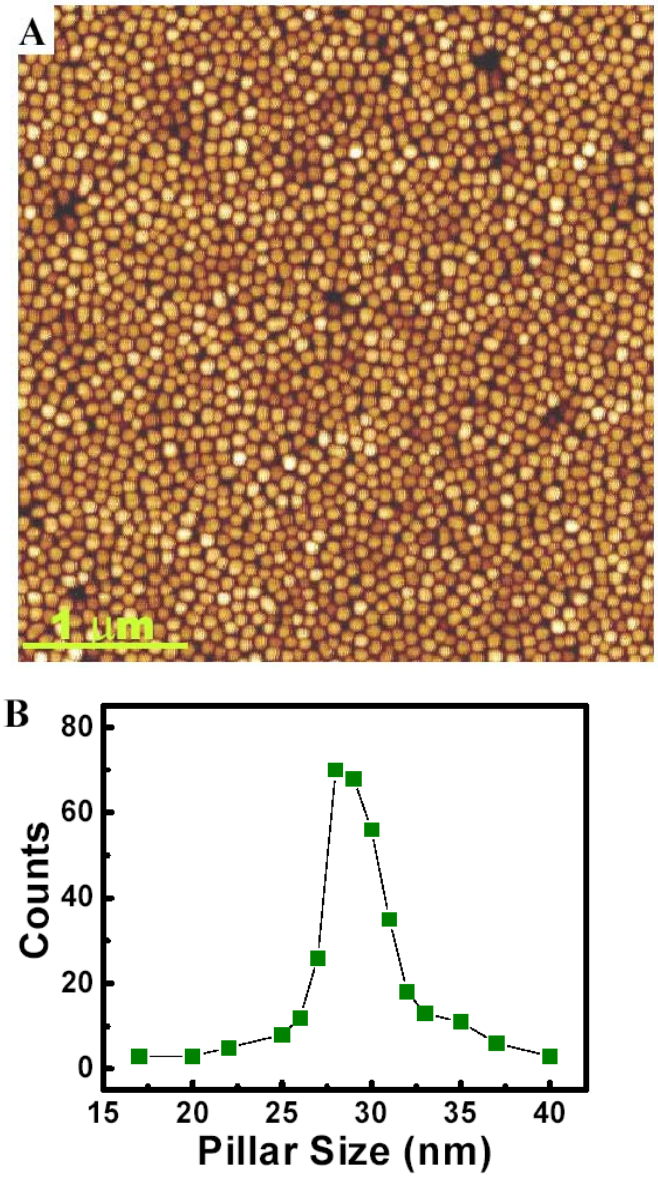

Fig.3.4 A. AFM topography image of the film; B. Statistical size distribution of the features.

Fig.3.6 is a dark field TEM image obtained using the $CoFe_2O_4$ $(\bar{2}60)$ spot from a cross-sectional sample. The image shows the columnar structure of the

$CoFe_2O_4$ phase. Pillars with an aspect ratio of about ~12 extend through the whole film from the film/substrate interface to the surface. It is interesting that all the pillars grow out of the matrix, forming islands that extend above the surface of the $BaTiO_3$ matrix with a height of 10-15 nm as can be seen in Fig.3.6B. This can be explained by the heteroepitaxial growth feature of the film. Namely, the *c* lattice parameters of $BaTiO_3$ and $CoFe_2O_4$ calculated from the XRD and electron diffraction patterns are *c* = 0.404 nm for $BaTiO_3$ and *c* = 0.834 nm for $CoFe_2O_4$. There are about 990 unit cells of $BaTiO_3$ along the film growth thickness of 400 nm. It is assumed that there are approximately 990/2 units of $CoFe_2O_4$ along the pillars. Therefore, the calculated height of $CoFe_2O_4$ pillars is ~412.8 nm, which is in agreement with the experimentally observed value (410-415 nm). The cross sectional high resolution TEM image shown in Fig.3.6C, shows that dislocations form at the interface between the $CoFe_2O_4$ pillars and the $BaTiO_3$ matrix, which partially relax the lattice mismatch strain between the two phases. However, a residual strain of 0.4% in the $CoFe_2O_4$ pillars still remains, which was calculated from both x-ray and TEM diffraction patterns.

Composition analysis of the nanostructure thin films was conducted using Energy Dispersive Spectrometry (EDS). A spot beam size down to ~1 nm diameter was used on a plan view TEM sample. Fig.3.7A and B are the spectra taken from the $BaTiO_3$ matrix and a single $CoFe_2O_4$ pillar, respectively. Dominant peaks from Ba and Ti, which completely overlap with each other, have been detected from $BaTiO_3$ matrix. On the other hand, primarily Co and Fe peaks are seen in the $CoFe_2O_4$ pillars. The spectra show small amounts of Co and Fe in the matrix and Ba and Ti in the pillar, which may be due to the beam spreading inside the sample. Both spectra show strong Cu peaks from the TEM sample supporting Cu grid.

Our X-ray and TEM results show that self-organized $CoFe_2O_4$-$BaTiO_3$ nanostructures exhibiting three-dimensional heteroepitaxy have been successfully synthesized. $CoFe_2O_4$ nanopillar arrays are embedded in a $BaTiO_3$ matrix. Detailed phase separation mechanisms and growth kinetics are discussed in the following section.

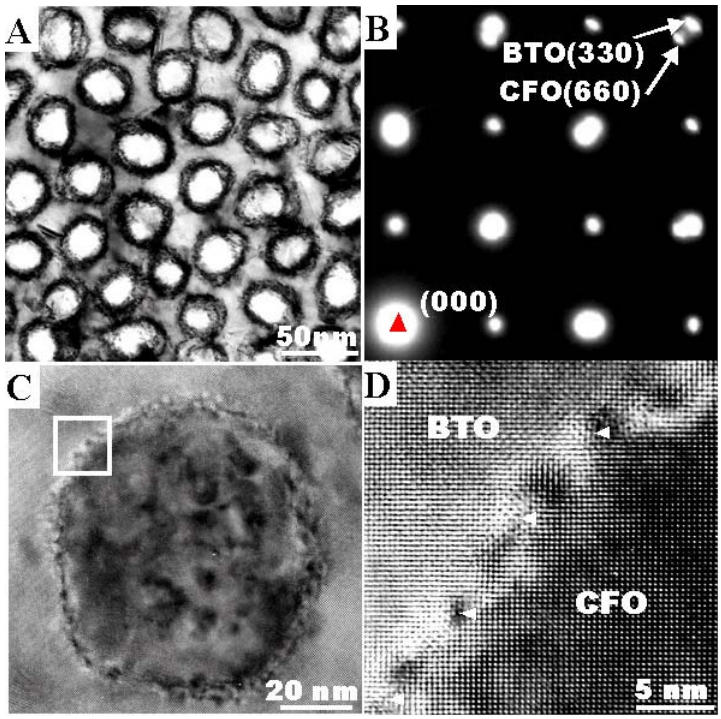

Fig.3.5 A. Plan-view TEM image of the film grown at 920 °C; B. Selected area diffraction pattern from A showing the epitaxial relationship of the two phases; C. High resolution TEM image of a single $CoFe_2O_4$ pillar in the $BaTiO_3$ matrix; D. Magnified segment of the interface between the $CoFe_2O_4$ pillar and the $BaTiO_3$ matrix from C.

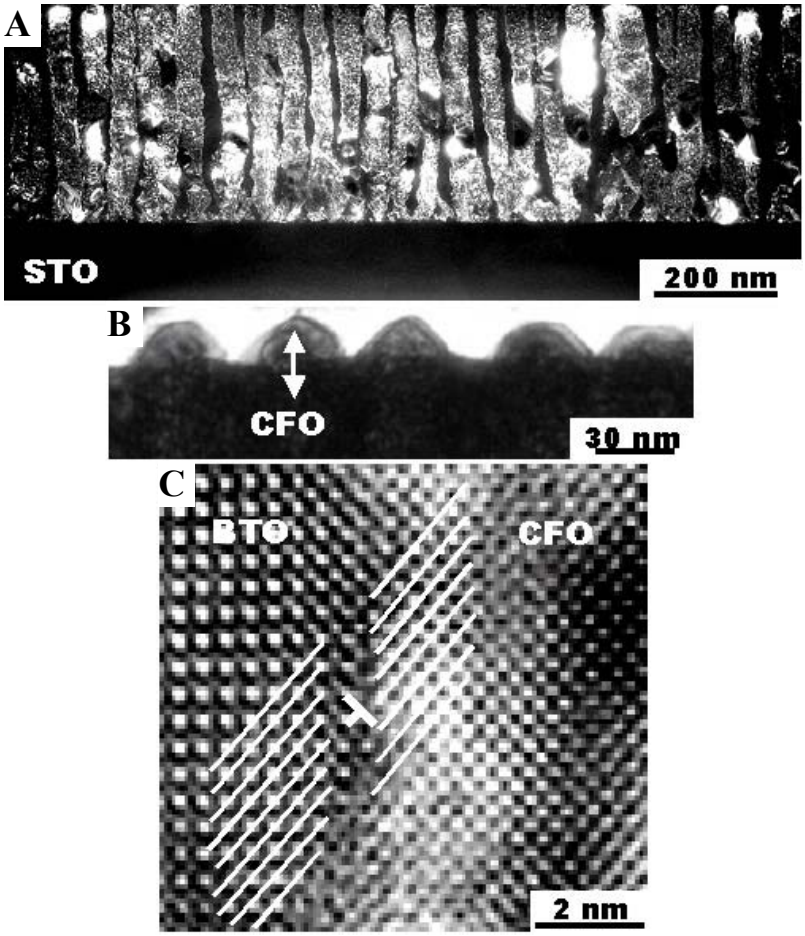

Fig.3.6 A. Dark field TEM image taken from a cross-section sample using g = [$\bar{2}$60] of $CoFe_2O_4$; B. bright field TEM image from a cross section sample showing the outgrowth of the $CoFe_2O_4$ nanopillars; C. cross-section high resolution TEM image showing dislocations formed at the interface between a $CoFe_2O_4$ pillar and the $BaTiO_3$ matrix.

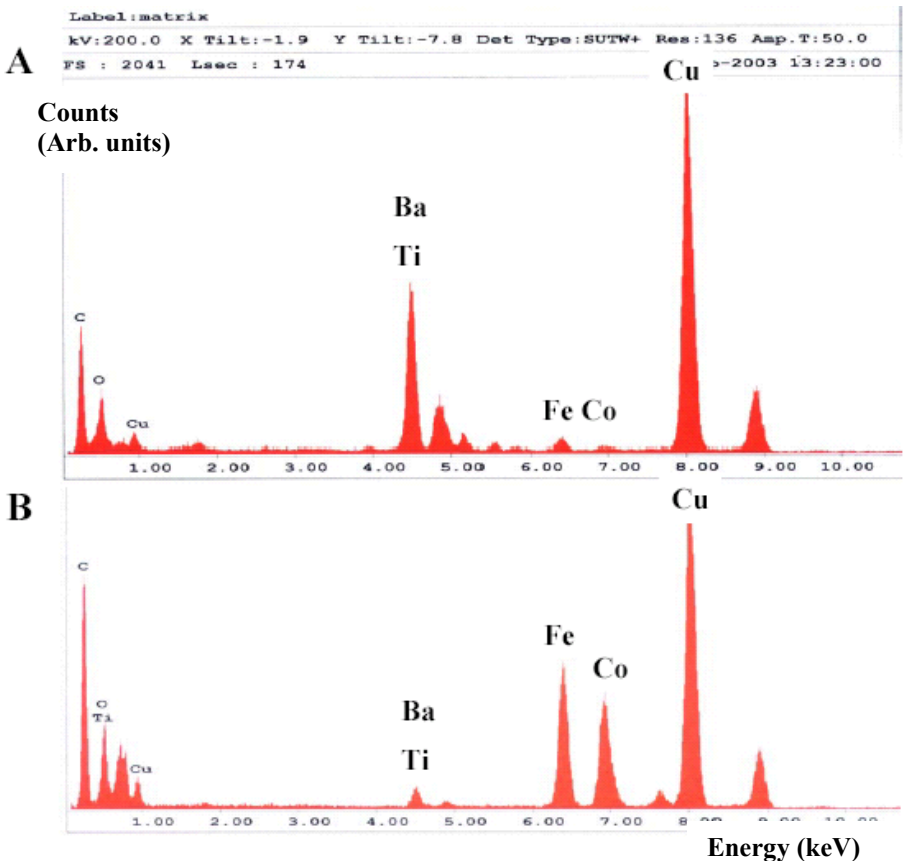

Fig.3.7 EDS spectrum from A. the $BaTiO_3$ matrix and B. a single $CoFe_2O_4$ pillar.

3.3 Growth kinetics of $BaTiO_3$-$CoFe_2O_4$ nanostructures

3.3.1 Temperature dependence

$BaTiO_3$-$CoFe_2O_4$ thin films with a thickness of 400 nm were deposited at various substrate temperatures (500 - 950°C) at a constant growth rate of 8 nm/min to investigate the role of growth temperature on the formation of the nanopillars. The as-deposited films formed $BaTiO_3$-$CoFe_2O_4$ nanostructures at growth temperatures above 750 °C. The results show that the lateral dimensions of the $CoFe_2O_4$ nanopillars increase systematically, from ~9 nm to ~70 nm as the growth temperature increases from 750 °C to 950 °C. As the lateral size of the pillars increases the spacing between the pillars also increases to keep the constant volume ratio of the two phases. Deposition temperatures in this study were restricted to ≤950 °C due to the operating temperature limit of the vacuum chamber heater. No phase separation was observed at temperatures below 700°C. Fig.3.8A through C are the plan view TEM images taken from the samples deposited at 850 °C, 900 °C and 950 °C, respectively. Distinct differences in the size and spacing of the pillars are observed. As the growth temperature increases both size and spacing between the pillars increase, which leads to almost constant volume fraction of the $CoFe_2O_4$ phase. The temperature dependence of the lateral dimensions of the nanopillars can be fitted to an Arrhenius behavior as seen in **Fig.3.9**. The average lateral size (represented by diameter, *d*) of the pillars was plotted as a function of inverse temperature. The associated activation energy was calculated to be 0.75 eV. This result was compared with the self-diffusion value of Co, Fe, and Oxygen. We believe that surface diffusion is the main contribution in the formation of $BaTiO_3$-$CoFe_2O_4$ phase separation in this system.

The lattice parameter (c) of $CoFe_2O_4$ pillars calculated from XRD is plotted in Fig.3.10 as a function of the growth temperature. Fig.3.10 shows that the c axis of the $CoFe_2O_4$ pillars increases as the growth temperature increases. Correspondingly, as the growth temperature increases the lateral dimension of the pillars also increases, and more dislocations form at the pillar-matrix interface. High density of dislocations are identified at the interface from the sample grown at 950 °C (Fig.3.5D) while fewer dislocations are shown at the interface from the sample grown at 850 °C (Fig.3.11). It is believed that dislocations partially relax the compressive strain from the matrix along the $CoFe_2O_4$ pillars, which induces an increase in the c axis lattice parameter of $CoFe_2O_4$. It is noticed that the c lattice parameter of $BaTiO_3$ remains almost constant (c ~ 0.404 nm) for the films grown in the temperature range of 800~900 °C. Thus, it is reasonable to believe that most of the strain induced by the lattice mismatch between $CoFe_2O_4$ pillars and $BaTiO_3$ matrix is accommodated in the $CoFe_2O_4$ pillars. This is probably due to the smaller volume fraction and smaller Young's modulus of the $CoFe_2O_4$ phase.

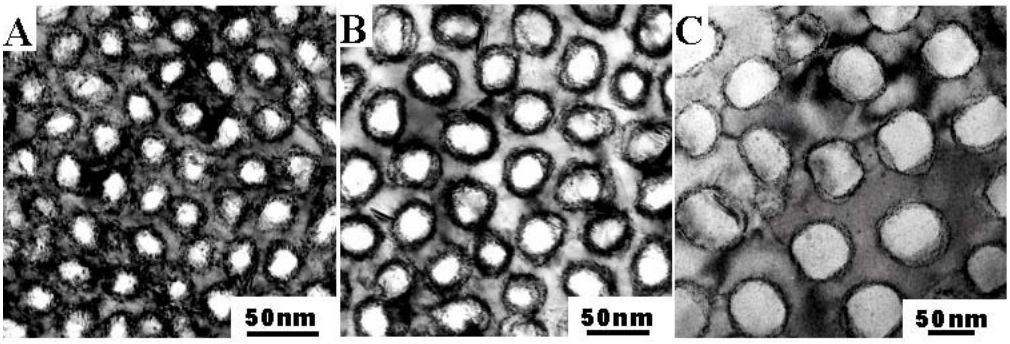

Fig.3.8 Plan view bright field TEM images of the film grown at A. 850 °C; B. 900 °C; and C. 950 °C.

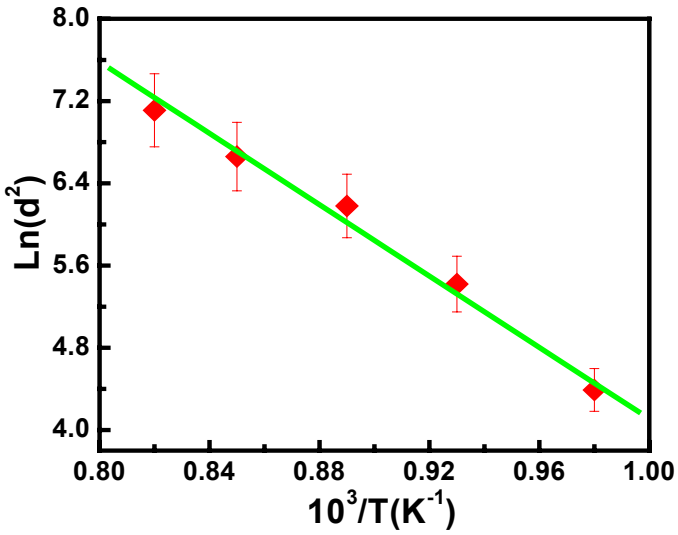

Fig.3.9 Plot of lateral dimension of the $CoFe_2O_4$ nanopillars ($ln(d^2)$) vs. temperature

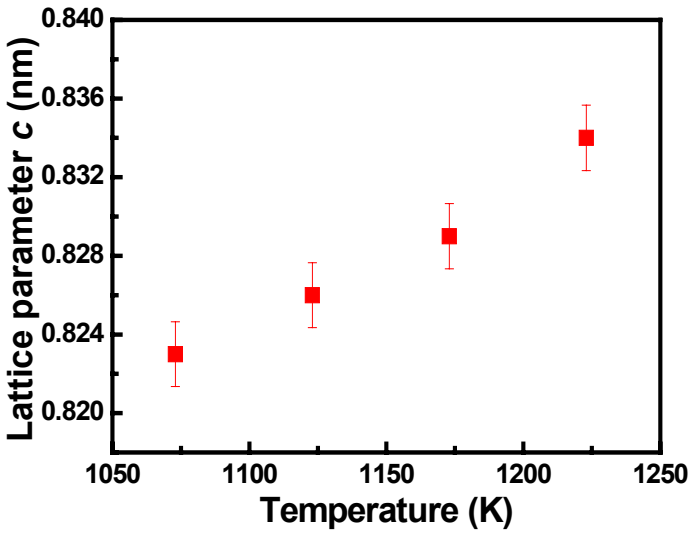

Fig.3.10 Lattice parameter (*c*) of $CoFe_2O_4$ pillars vs. growth temperature.

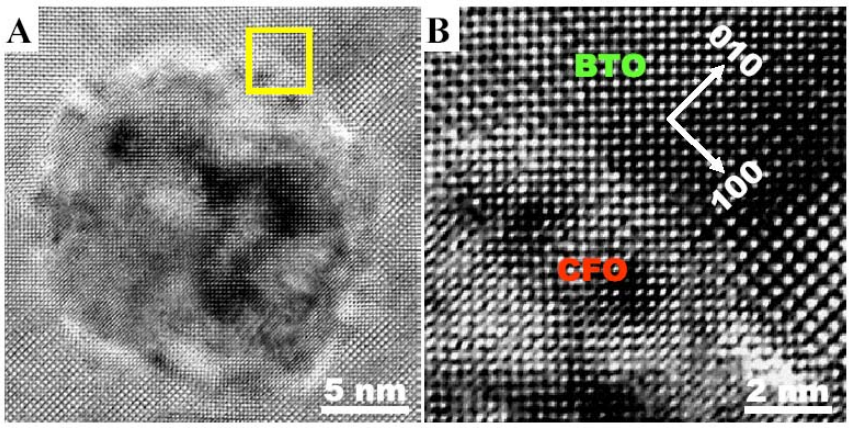

Fig.3.11 Plan view HRTEM images of the sample grown at 850 °C: A. A single $CoFe_2O_4$ pillar embedded in $BaTiO_3$ matrix; B. Magnified segment in A showing the sharp interface between the pillar and matrix. A low dislocation density was identified at the interface.

As it was mentioned above, no phase separation was observed at growth temperatures below 700 °C for a growth rate of 8 nm/min. Both XRD and TEM analyses of the films grown at temperature below 750 °C show that the films have a considerably supersaturated $BaTiO_3$ structure. A relatively large lattice constant was calculated (a = 0.406 nm at 750 °C and 0.408 nm at 700 °C). Lattice distortion and defects such as antiphase domain boundaries (ADBs) were observed in the films grown at low temperatures. The antiphase domain boundaries may provide a diffusion path during the formation of nanostructure array. The diffusion and the role of antiphase domain boundaries are discussed in section 3.3.3 and section 3.4.

3.3.2 Growth rate dependence

The formation of $BaTiO_3$-$CoFe_2O_4$ nanostructures is strongly dependent on the growth rate of the film. As the growth rate increases, the onset temperature for phase separation of $BaTiO_3$ and $CoFe_2O_4$ also increases. Fig.3.12 A and B are selected area diffraction patterns taken from the plan view TEM samples grown at 700 °C with the growth rates of ~8 nm/min and ~1.5 nm/min, respectively. In Fig.3.12A, a single set of spots is observed which is indexed according to a supersaturated perovskite $BaTiO_3$ structure. Comparatively, two sets of spots corresponding to perovskite $BaTiO_3$ and spinel $CoFe_2O_4$ are clearly identified in the diffraction pattern from the sample grown at a much lower growth rate of ~1.5 nm/min (Fig.3.12B). The supersaturated $BaTiO_3$ has a relatively large lattice parameter, a ~ 0.408 nm. As the $CoFe_2O_4$ nanopillars form the $BaTiO_3$ matrix relaxes and its a lattice parameter reduces to ~ 0.404 nm as calculated from the XRD and electron diffraction patterns.

The effect of growth rate on $BaTiO_3$-$CoFe_2O_4$ nanostructures is also observed by comparing samples grown at 900 °C with a growth rate of ~8 nm/min (Fig.3.12C) and ~16 nm/min (Fig.3.12D). As the growth rate is increased, considerable increase in generation of defects was observed in the nanostructures. As shown in Fig.3.12D, both $BaTiO_3$ and $CoFe_2O_4$ spots have arc shapes in the high index spots, i.e. $BaTiO_3$ (220) and $CoFe_2O_4$ (440). High resolution TEM studies show that there is a slight misorientation between individual $CoFe_2O_4$ pillars although each ipillar itself is still single crystalline. These films also show a high-density of antiphase domain boundaries in the $BaTiO_3$ matrix. The lateral size of the $CoFe_2O_4$ pillars is slightly smaller in the sample grown at high growth rate compared with the one grown at

lower growth rate, which implies that an increase in growth rate has the similar impact on the lateral dimensions of the pillars as a decrease in the growth temperature.

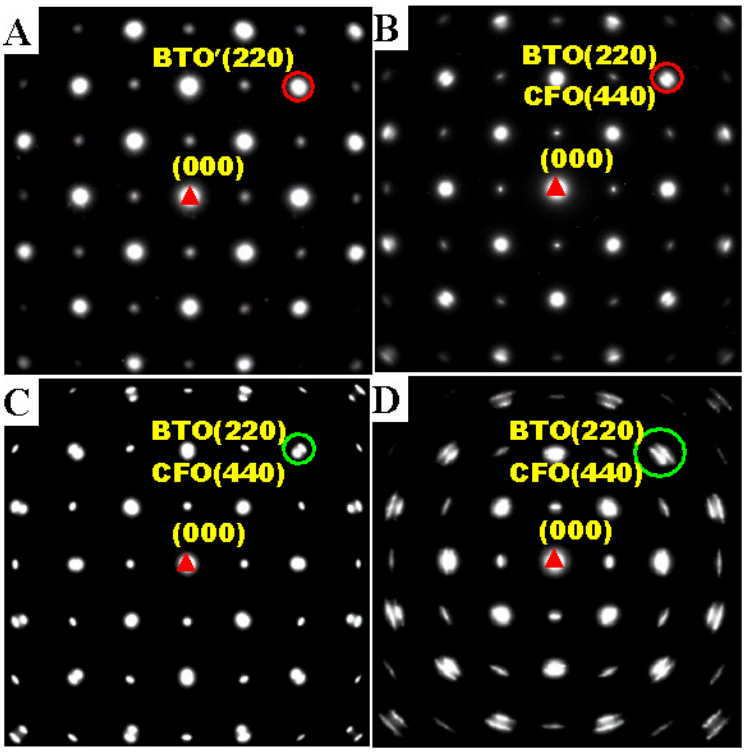

Fig.3.12 Selected area diffraction patterns taken from plan view TEM samples grown at A. 700 °C with a grow rate of ~8 nm/min; B. 700 °C with a grow rate of ~1.5 nm/min; C. 900 °C with a grow rate of ~8 nm/min; and D. 900 °C with a grow rate of ~16 nm/min. Only one set of spots is observed in A, which is indexed according to a supersaturated $BaTiO_3$ (BTO′).

3.3.3 Phase separation and surface diffusion

Phase separation can occur in thin films as well as in bulk materials. The phase separation process in bulk materials is well understood[104]. These processes

include spinodal decomposition, lamellar growth, and second phase coarsening (Ostwald ripening). The phase separation process in thin films is more complicated because of two unique features: (1) deposition occurs at a fixed externally imposed growth rate; and (2) atomic transport occurs preferentially along the advancing surface. Therefore, phase separation during thin film growth is directed by surface diffusion, and bulk interdiffusion is in general negligible. This feature is associated with the fact that activation energies for surface diffusion are typically smaller than those for bulk diffusion at low temperatures. Therefore, the evolution of the microstructure of the film is the result of the freezing-in of the structure that existed at the film surface. Understanding the surface diffusion of different chemical species is crucial in order to understand the mechanism of phase separation during film deposition.

In order to describe the temporal evolution of the surface composition profile *c (x, y; t)*, it should be considered that Fick's diffusion is along the surface (*x*-*y* plane) and the surface is constantly being buried and incorporated into the bulk as more material is deposited during film growth. The film is assumed to be flat, growing with a velocity *v* in the *z* direction as the result of a spatially and temporally uniform flux of atoms with average composition c_0. Assuming the interdiffusion coefficients are $\tilde{D}_s$ along the surface and $\tilde{D}_B$ in the bulk of the film, the composition *c(x, y, z; t)* in the frame of the advancing surface along the z direction must satisfy the following equations[107]:

$$\frac{\partial c}{\partial t} = \tilde{D}_s \nabla_s^2 c - \frac{\tilde{D}_B}{\delta}\frac{\partial c}{\partial z} + v\frac{c_0}{\delta} - v\frac{c}{\delta} \quad \text{(surface, } z = vt\text{)} \qquad \text{Eq.3.1a}$$

$$\frac{\partial c}{\partial t} = \tilde{D}_B \nabla_s^2 c + v\frac{\partial c}{\partial z} \quad \text{(bulk, } z < vt\text{)} \qquad \text{Eq.3.2b}$$

where δ is the width of the surface diffusion layer (normally a few atomic spacings), and $\nabla_s^2 = (\frac{\partial^2}{\partial x^2} + \frac{\partial^2}{\partial y^2})\big|_{z=vt}$ where z = *vt* implies that the derivatives are to be evaluated on the surface. Eq.3.1a makes use of the assumption that the rate at which atoms diffuse across the boundary separating the surface region and the bulk region is determined by the bulk interdiffusion $\tilde{D}_B$. Since the surface is assumed to remain flat during the deposition, we can get: $\nabla_s^2 = (\frac{\partial^2}{\partial x^2} + \frac{\partial^2}{\partial y^2})\big|_{z=0}$.

For small $\tilde{D}_B$, Eq.3.1b reduces to $\frac{\partial c}{\partial t} \approx v\frac{\partial c}{\partial z}$, which implies that $c(x, y, z; t) \approx c(x, y, 0; t + z/v)$. Therefore, the bulk composition profile is simply a history of the surface composition profile. With this approximation, Eq.3.1a becomes:

$$\frac{\partial c}{\partial t} \cong \frac{\tilde{D}_s \nabla_s^2 c + v[(c_0 - c)/\delta]}{1 + (\tilde{D}_B / v\delta)} \cong \tilde{D}_s \nabla_s^2 c + \frac{v}{\delta}(c_0 - c) \qquad \text{Eq.3.3}$$

In Eq.3.2, we assume $\tilde{D}_B / v\delta \sim 0$ since $\tilde{D}_B \le v\delta$ and $\tilde{D}_B / v\delta \sim 10^{-9}$ for typical deposition[106] conditions.

Eq.3.2 was employed by Cahn[105] 30 years ago in an analysis of eutectoid decomposition process. A similar mechanism was used to understand the phase separation in Al-Ge films by Atzmon and co-workers[106,107,108,109]. The Al-Ge system has a simple eutectic phase diagram with low mutual solubilities. The lateral phase separation induced domains with distinct difference in composition when the film was deposited by electron beam evaporation onto oxidized Si substrates. Phase separation in this system results in a regular array of cylindrical α-domains embedded in a β matrix. Two-dimensional analysis[106,107] using the composition profile given by Eq. 3.2 yielded a steady state domain with a radius *R* proportional to $\rho = \sqrt{\tilde{D}_s \delta / v}$,

where ρ is the interdiffusion distance during the deposition of a layer of thickness δ. These results suggested that the steady state domain radius is determined by the diffusion equation alone, which is independent of the initial conditions. The same analysis can qualitatively explain the results that were obtained in the $BaTiO_3$-$CoFe_2O_4$ system presented in this work.

As it was discussed in section 3.3.1, the lateral dimensions of the $CoFe_2O_4$ pillars increased by either raising the growth temperature or decreasing the deposition rate. Since for a thickness of 400 nm the nanostructured thin films have already reached a steady state pillar size (as can be seen from the cross section TEM images in Fig.3.6), the diameter of the pillars can be interpreted to be proportional to the surface chemical interdiffusion distance ρ in this system. The only parameter in the expression for ρ, that varies with temperature is the surface diffusion coefficient $\tilde{D}_s$. It is expected that the diameter of the pillars have the same temperature dependence as $(\tilde{D}_s)^{1/2}$. Both raising the growth temperature (increases $\tilde{D}_s$) and decreasing the deposition rate ν increase the interdiffusion distance ρ. Thus the lateral size of the pillars increases in both cases. This surface diffusion model qualitatively explains the experimental results that we discussed before.

Although the model can explain the experimental results in the present system, its limitations have to be considered. First of all, this is a simple model developed for binary alloys. The surface diffusion is expected to be more complicated in the $BaTiO_3$-$CoFe_2O_4$ system due to the multiple components involved in the deposition process. Differences in the structure between the perovskite and spinel phases, multi-element diffusion and possible interactions should all be considered in the complex oxide system. Furthermore, the assumption that the film surface remains flat

throughout deposition is not completely valid during the PLD growth of $BaTiO_3$-$CoFe_2O_4$ films. As it was shown in Fig.3.6B, surface roughness with preferential outgrowth of $CoFe_2O_4$ pillars was observed. Therefore, surface roughness and strain relaxation must also be considered in a quantitative model. Moreover, the high density of antiphase domain boundaries observed in some of the films, may provide diffusion paths for the nanostructure formation. An advanced model needs to be developed to more fully describe the present complex oxide system.

3.4 The role of antiphase domain boundaries

Antiphase domain boundaries are characterized by two neighboring domains shifted by half a lattice unit cell with respect to one another. The boundary that separates the two domains is called antiphase domain boundary (ADB). A high density of ADBs was observed in the samples grown at low temperatures or with a relatively high growth rate. Fig.3.13A is a plan view TEM image taken from a sample grown at 700 °C with the grow rate of ~8 nm/min. A high density of intertwined ADBs are observed. Selected area diffraction pattern (Fig.3.13B) shows that the film is single phase with perovskite type structure, which corresponds to a highly supersaturated $BaTiO_3$ phase. The high resolution TEM image shown in Fig.3.13C shows the microstructure of the ADBs with a half unit cell shift between the neighboring domains as schematically illustrated in Fig.3.13D. The dimension of the antiphase domains varies from a few nanometers to tens of nanometers.

Fig.3.14 is a high resolution TEM image taken from the sample grown at 850 °C, which shows two $CoFe_2O_4$ pillars connected by ADBs. Fig.3.14 also shows an array of edge dislocations that probably formed at the vanishing of an ADB. Our TEM results suggest that the $CoFe_2O_4$ phase preferentially precipitates at the high

curvature regions of the ADBs and the ADBs may provide a diffusion path for the subsequent growth of the $CoFe_2O_4$ pillars.

The density of the ADBs decreases with the increase of deposition temperature. Fig.3.15A and B are plan view TEM images taken from the samples grown at 850 °C and 950 °C, respectively. A relatively high density of ADBs is observed in the sample grown at 850 °C, while the density of ADBs is reduced considerably in the sample grown at the higher temperature. It is important to note that a decrease in the growth rate can also considerably decrease the ADB density. These results indicate that ADBs are formed in the $BaTiO_3$ matrix when surface diffusion is limited.

The formation of the antiphase domains in the present films most likely results from lattice distortions due to local composition inhomogeneities. When Co and Fe incorporate into $BaTiO_3$ and form a supersaturated $BaTiO_3$ phase, normally, Co and Fe take the Ti sites due to the similar size of their ionic radii. However, some of them must also take the Ba sites in order to keep the stoichiometry in the system. Consequently, ADBs are induced due to the neighboring domains with Co and Fe taking different lattice sites.

The fact that ADBs are closely correlated to the nanostructure formation suggests the important role of ADBs in the diffusion process necessary for the nanostructure formation. There have been some discussions on the role of ADBs on phase transformations in bulk materials. By using a Ginzburg-Laudau model, Allen and Cahn [110] first discussed the motion of solitary ADBs to explain the composition instability resulting in ADBs wetted by a disordered phase. Matsmura et al[111] studied the kinetics of segregation of solvent atoms into the ADBs using a Landau-type free energy expansion. Chen and Khachaturyan[112] discussed the precipitation of ordered

intermetallics through ADBs. It was concluded that segregation at ADBs is a barrierless process. In the formation of $BaTiO_3$-$CoFe_2O_4$ thin film nanostructures, it is expected that ADBs provide not only the nucleation site but also the diffusion path for the growth of the $CoFe_2O_4$ nanopillars. Antiphase domain boundaries are in general non-equilibrium features. They have a positive excess free energy. Thus, they will migrate to reduce the total amount of boundary area by a thermodynamic driving force. Resistance to the motion of the ADBs is often diffusional. In thin film growth, the surface interdiffusion dominants over bulk diffusion. Therefore, the mobility of ADB at the surface of a thin film is expected to be high. The precipitated $CoFe_2O_4$ phase at ADBs tends to be carried along as ADBs move. Thus, ADBs serve as diffusion paths in the growth of $CoFe_2O_4$ nanopillars. As the ADB moves and vanishes, dislocations can easily form (see Fig.3.14). When diffusion is limited, for instance at a low growth temperature or with high growth rate, mobility of ADBs at film surface is small. ADBs can be frozen into the bulk of the film, which induce a high density of ADBs in the films grown at low temperatures or with high growth rates.

In conclusion, ADBs formed in the $BaTiO_3$-$CoFe_2O_4$ thin films. ADBs are closely related to the formation of the $BaTiO_3$-$CoFe_2O_4$ nanostructures. For the above discussion, it is evident that ADBs play an important role in the nucleation and subsequent growth of the $CoFe_2O_4$ nanopillars.

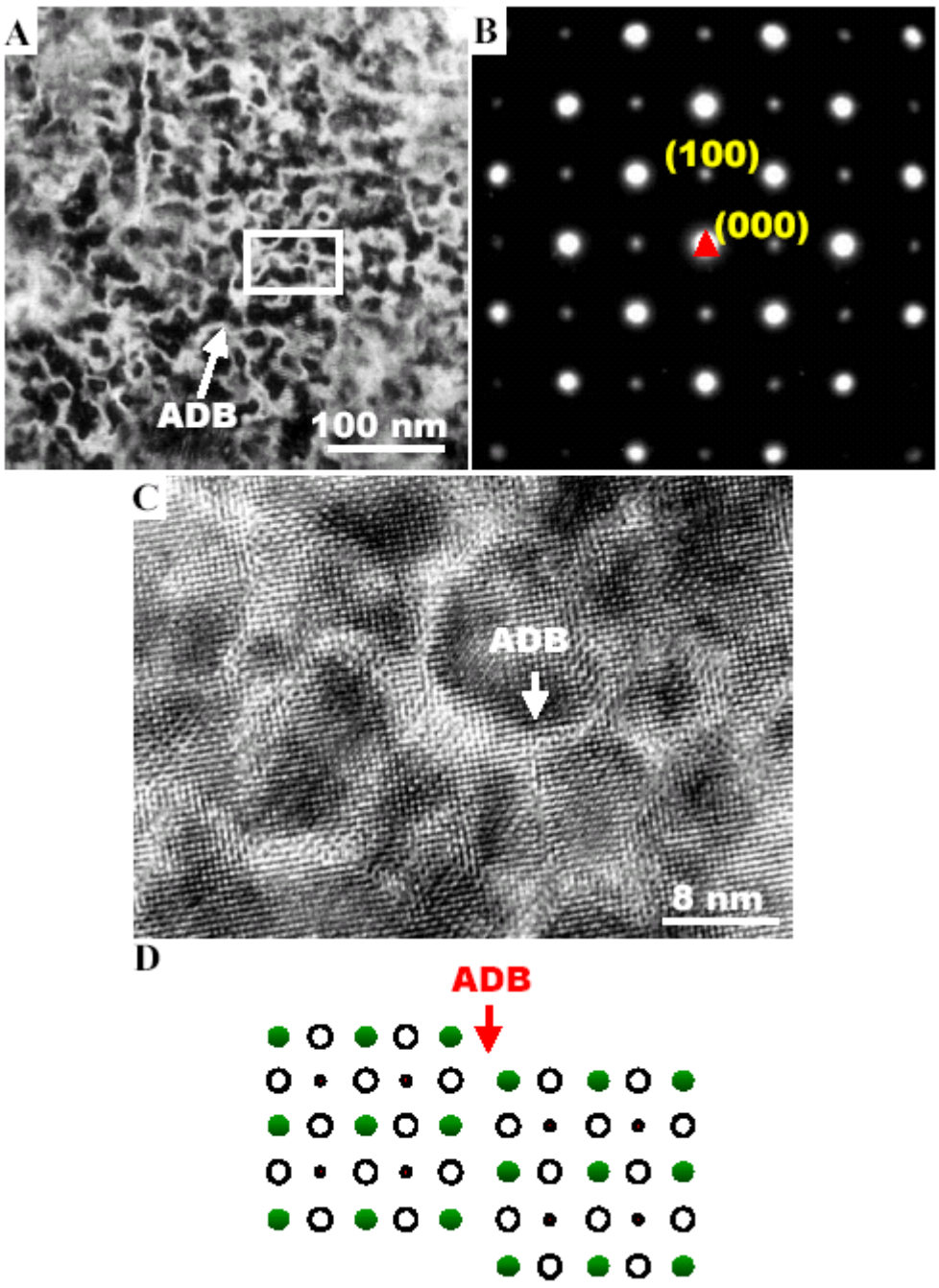

Fig.3.13 A. Plan view TEM image taken from the sample grown at 700 °C with a grow rate of about 8 nm/min; B. Corresponding selected area diffraction pattern; C. High resolution TEM image taken from the area marked in A; D. Schematic of an antiphase domain boundary (APB).

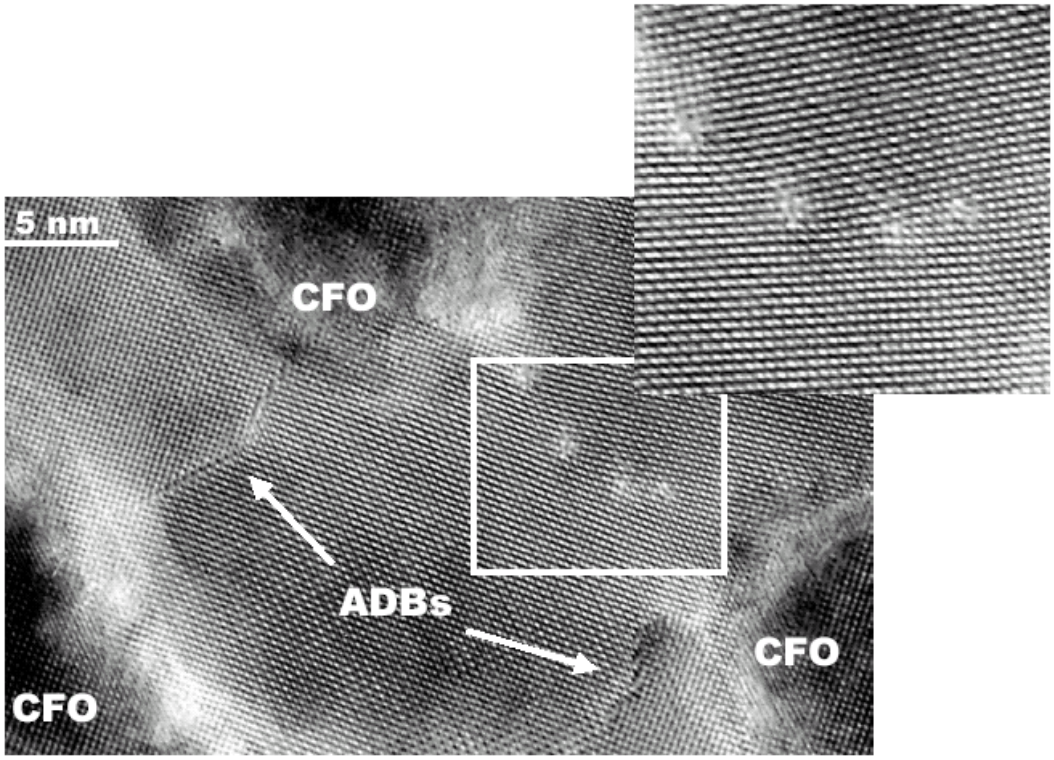

Fig.3.14 High resolution TEM images taken from a film grown at 850 °C with a thickness of 400 nm. It shows antiphase domain boundaries (ADBs) in the $BaTiO_3$ (BTO) matrix phase, which link the $CoFe_2O_4$ (CFO) pillars. The inset is a magnified image showing the dislocations formed at the dissolution of an ADB.

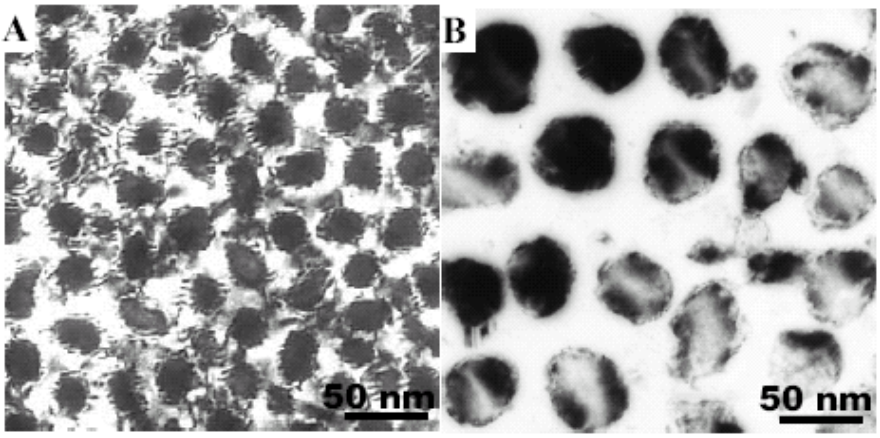

Fig.3.15 Plan view dark field TEM images taken from the samples grown at A. 850 °C; B. 950 °C.

3.4 Thickness evolution of $BaTiO_3$-$CoFe_2O_4$ nanostructures

The spontaneous formation of $BaTiO_3$-$CoFe_2O_4$ nanostructured films is a process that involves rich thermodynamics and kinetics. In order to understand the kinetic and thermodynamic factors governing the nanostructure formation, it is necessary to conduct systematic studies by methodical variation of the growth conditions. For example, the thin films that were discussed in the previous sections, that evaluated the impact of growth temperature, growth rate, etc., are based on films with a fixed thickness of 400 nm. Interpretation of the film growth dynamics has been based on observations of the film surface at the final state and assisted by the cross-section TEM images. However, in order to better understand the growth evolution of the $BaTiO_3$-$CoFe_2O_4$ thin film nanostructure it is imperative to study the microstructure and morphology of films varying film thickness with special attention to the evolution at the film surface.

In this section, we discuss the thickness evolution of $BaTiO_3$-$CoFe_2O_4$ nanostructures. Each of the films can be interpreted as a frozen state with a different time intervals during the continuous growth of a thicker film. Fig.3.16A shows X-ray θ-2θ diffraction spectra from samples with different film thickness, from ~8 nm to ~400 nm. All the films were grown at a substrate temperature of 950 °C. The spectra show that films with thickness below 150 nm present extra peaks besides the expected (00*l*) peaks from the $BaTiO_3$ and $CoFe_2O_4$ phases from the film and $SrTiO_3$ substrate. The peaks were assigned to (111) $BaTiO_3$, (220) $CoFe_2O_4$ and some other unknown phases. As the thickness increases to ~400 nm, spectra show only (00*l*) peaks from $BaTiO_3$ and $CoFe_2O_4$ phases in the film. The small extra peaks that were observed the thinner films disappeared in thicker films. $BaTiO_3$ (002) and $CoFe_2O_4$ (004) peaks in

the XRD θ-2θ spectra from the sample with different thickness were plotted separately in Fig.3.16B. Films with thickness below 100 nm do not show a clear $CoFe_2O_4$ peak due to the low intensity of the peaks in the thin films. As the thickness of the film increases, the lattice constant of the $BaTiO_3$ phase first decreases with increasing film thickness. From 100 nm to 400 nm, the c axis of $BaTiO_3$ phase increases from 0.402 nm to 0.404 nm. In contrast, the lattice of the $CoFe_2O_4$ phase remains almost constant in the same range of film thickness. Considering the complex structure of the films such as the presence of other orientations and impurity phases interpretation of such changes in the lattices is difficult.

Fig.3.17A-F are plan view TEM images taken from the samples grown at 950 °C with thickness of about 8 nm, 20 nm, 50 nm, 150 nm, 250 nm, and ≥400 nm, respectively. Striking changes are observed in the patterns as the film thickness increases. Fine ripples appear in the morphology in the 8 nm thin film (see Fig.3.17A). The wavelength of the ripples is only 4-6 nm, which correlates with the surface interdiffusion distance. As the growth temperature decreases, the wavelength of the ripples decreases as well. Complex intermediate phases other than $BaTiO_3$ and $CoFe_2O_4$ were identified in the film, which will be discussed below in more detail. As the thickness of the film increases intertwined microstructures form (see Fig.3.17B). More clearly defined $CoFe_2O_4$ domains form which grow rapidly with increasing film thickness. At the film thickness reaches about 50 nm, irregularly-shaped $CoFe_2O_4$ domains and length of over 200 nm are observed (Fig.3.17C). As the thickness is increased further, the irregular $CoFe_2O_4$ domains gradually break up to form domains and gradually form domains with finite size and with fairly circular shape (see Fig.3.17D-F). Films reach a steady state with uniform $CoFe_2O_4$ domains size and

spacing when the film thickness is over 400 nm (Fig.3.17F). Such films show three-dimensional heteroepitaxy with $CoFe_2O_4$ pillars embedded in a $BaTiO_3$ matrix.

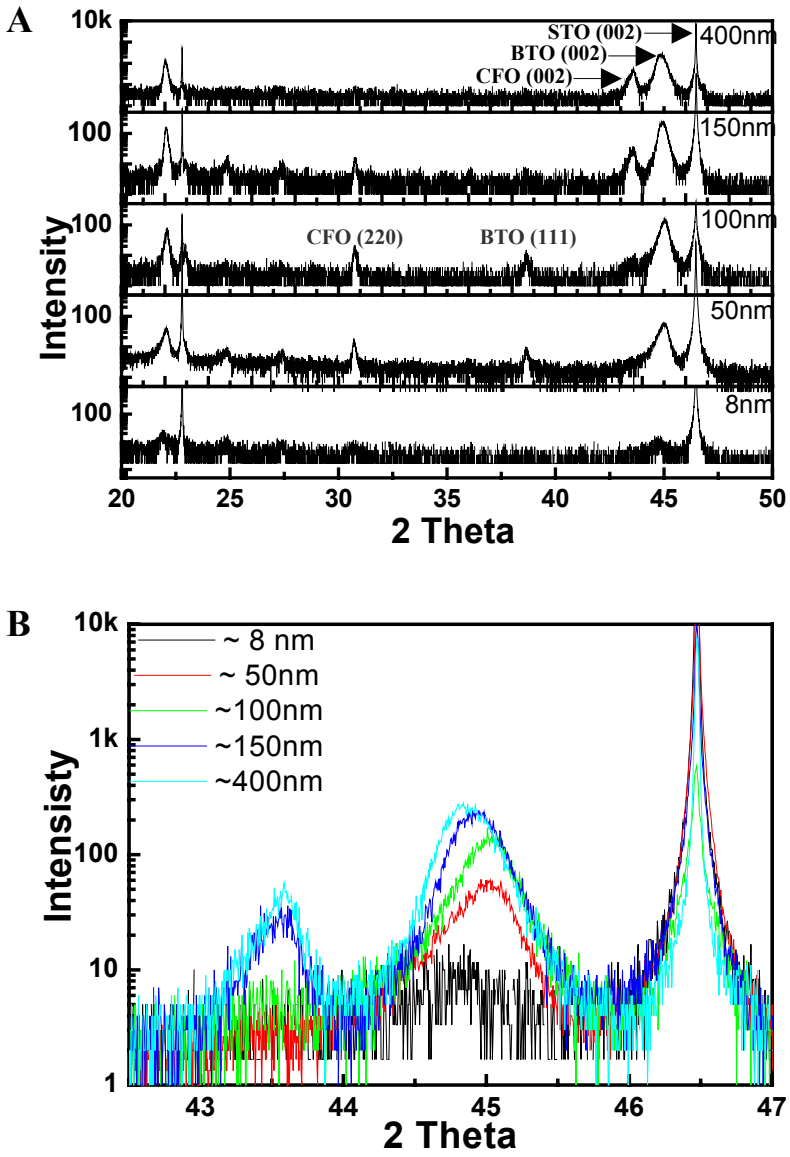

Fig.3.16 A. X-ray θ-2θ diffraction spectra from the films with various thickness: 8 nm; 50 nm; 100 nm; 150 nm; 400 nm. All the films were grown at 950 °C. B. $BaTiO_3$ (002), $CoFe_2O_4$ (004) and $SrTiO_3$ (002) peaks of the samples with different thickness.

Special attention was given to the initial growth of the films in order to understand how the films evolved into fine well-ordered nanopillar structures. Fig.3.18 A and B are plan view high resolution TEM images taken from the sample grown at 950 ºC with a thickness of about 8 nm. Complex intermediate phases are shown in the image. Local ordered domains are clearly visible in these images. Selected area diffraction pattern (Fig.3.18C) form this sample shows a set of weak spots in addition to the set of $SrTiO_3$ spot from the substrate (since the film is very thin). Some of the weak spots may be due to multiple diffraction during TEM imaging. Thermodynamically unstable intermediate phases may also correspond to the weak spots formed at this initial non-equilibrium state. As shown in the images in Fig.3.18 A and B, there are considerable local structural inhomogeneities in the film. Note that the selected area diffraction pattern reflects the average structure of only about a 1 μm diameter area in the film.

As the growth of the film continues to about a thickness of 20 nm, (001) $BaTiO_3$ and (001) $CoFe_2O_4$ domains as well as (220) $CoFe_2O_4$ and (111) $BaTiO_3$ domains can be distinguished within the intermediate phase structure. Fig.3.19 is a plan view TEM image taken from the 20 nm thick sample, which shows the (001) $BaTiO_3$ and neighboring intermediate domains. The subsequent formation and growth of $BaTiO_3$ and $CoFe_2O_4$ domains are at the expense of the intermediate phases. When the film reaches a thickness of 400 nm, all the intermediate phases have disappeared and only epitaxial $BaTiO_3$ and $CoFe_2O_4$ phases are observed in the diffraction patterns and TEM images. Fig.3.20 is a cross section TEM image from a sample with film thickness of about 400 nm. It shows only (001) $BaTiO_3$ and (001) $CoFe_2O_4$ phases with a sharp interface with the substrate. No intermediate phases and no phases with other orientations are observed in the film. It is very interesting to note that $CoFe_2O_4$

pillars have a V shape at the film-substrate interface. One reason may be the large lattice mismatch between the $CoFe_2O_4$ phase and $SrTiO_3$ substrate, which makes the direct growth of $CoFe_2O_4$ on $SrTiO_3$ unfavorable.

The structural and pattern evolution observed in the $BaTiO_3$-$CoFe_2O_4$ system as a function of film thickness is dramatic and to our knowledge has not been reported in any other system. Films with a composition within the $BaTiO_3$-$CoFe_2O_4$ two-phase region in the bulk phase diagram, we are expected to have phase separation during deposition. The ripple morphology and metastable phases observed at the initial stages of growth result from phase separation and are nucleation-driven. The subsequent formation of $BaTiO_3$ and $CoFe_2O_4$ phases follows the ripple morphology and forms large domains. The growth of the domains is at the expense of the local inhomogeneous intermediate phases. Phase separation through intermediate ordered phases has been reported in bulk intermetallics[113]. As the thickness of the film increases further, the elastic contribution of the two phases to the total energy becomes important. In this stage, the straight interfaces become unstable[114] resulting in break up of the large domains into a much finer domain structure. Therefore, the elastic interaction between the pillars plays an important role in driving the system to form well-organized structures.

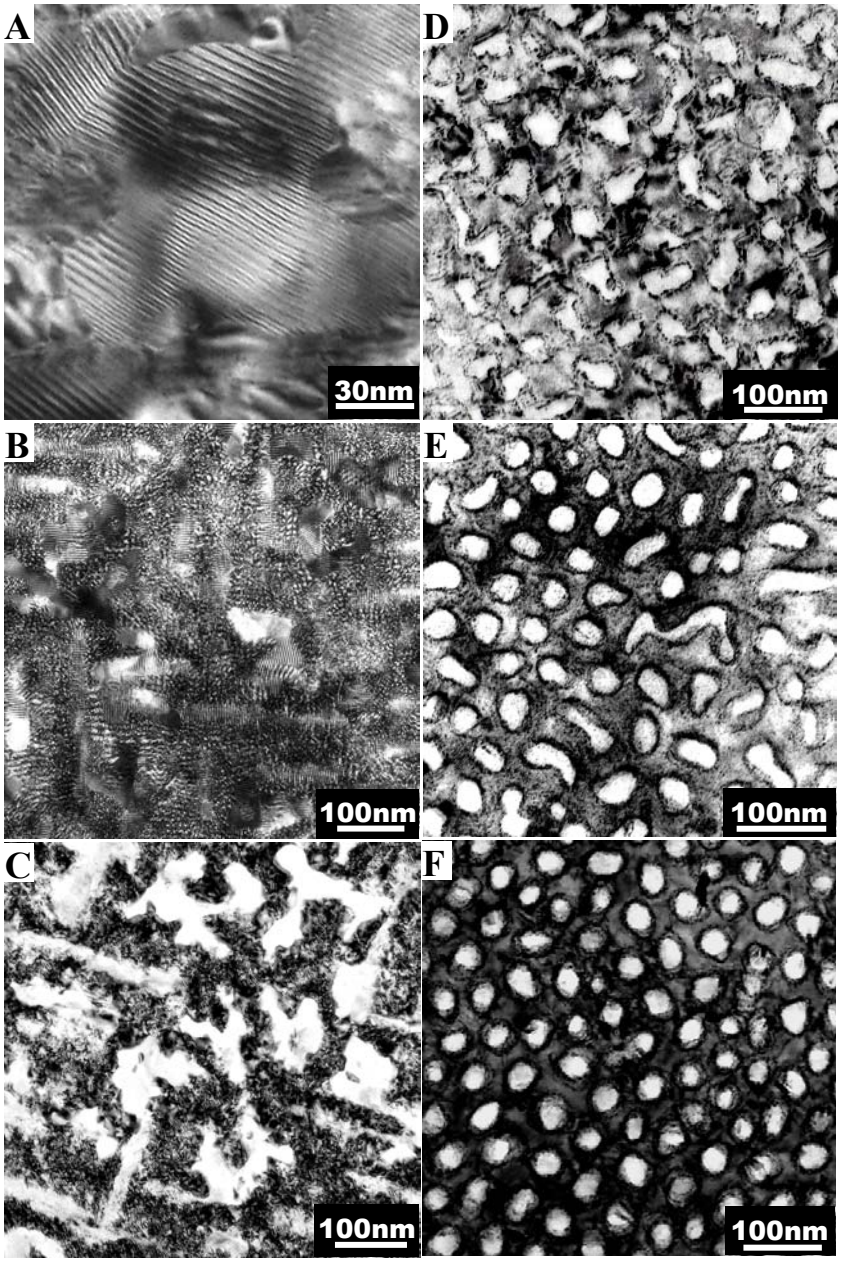

Fig.3.17 Plan view TEM images taken from the samples grown at 950 °C with thickness of about A. 8 nm; B. 20 nm; C. 50 nm; D. 150 nm; E. 250 nm; and F. 400 nm. In images of C-F, the features in white contrast are $CoFe_2O_4$ while the phase in dark contrast is $BaTiO_3$.

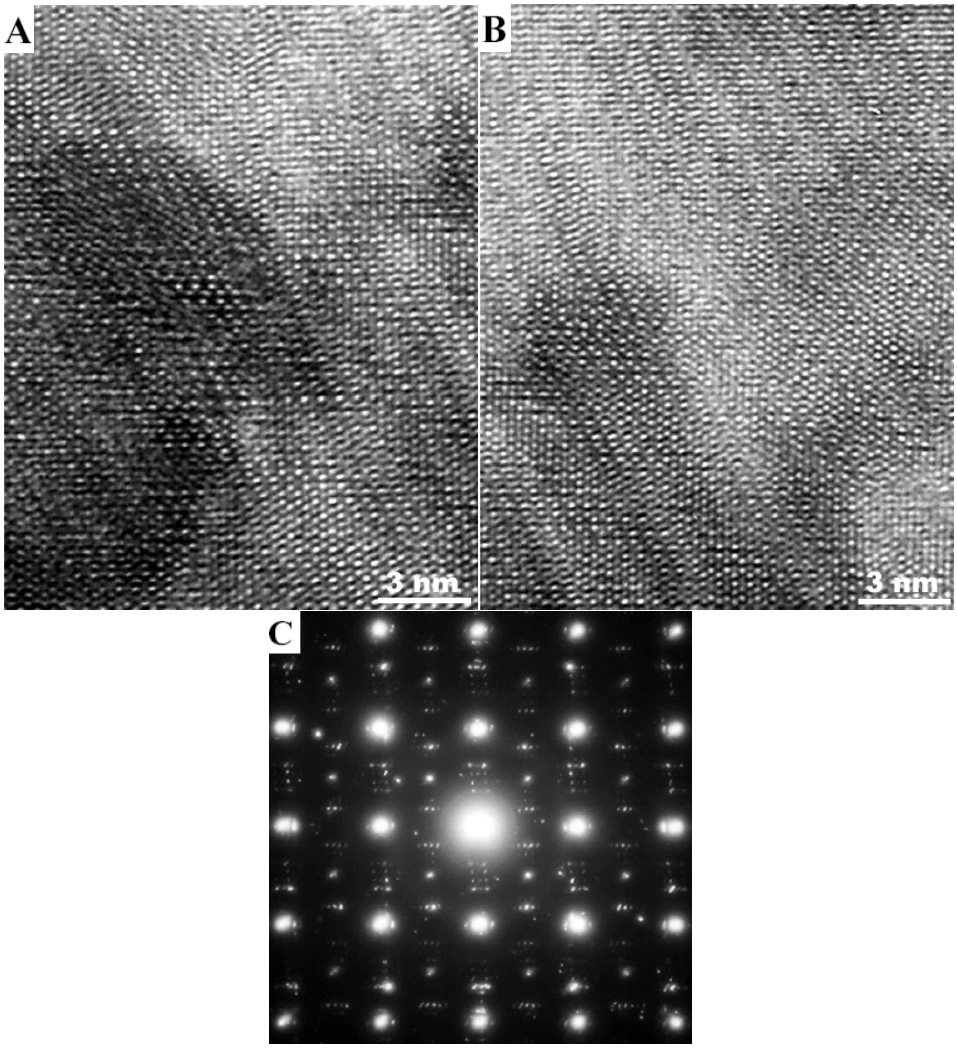

Fig.3.18 A and B Plan view high resolution TEM images taken from the sample grown at 950 ºC with a thickness of ~8 nm, showing intermediate ordered domain structures; C. selected area diffraction pattern from the same sample.

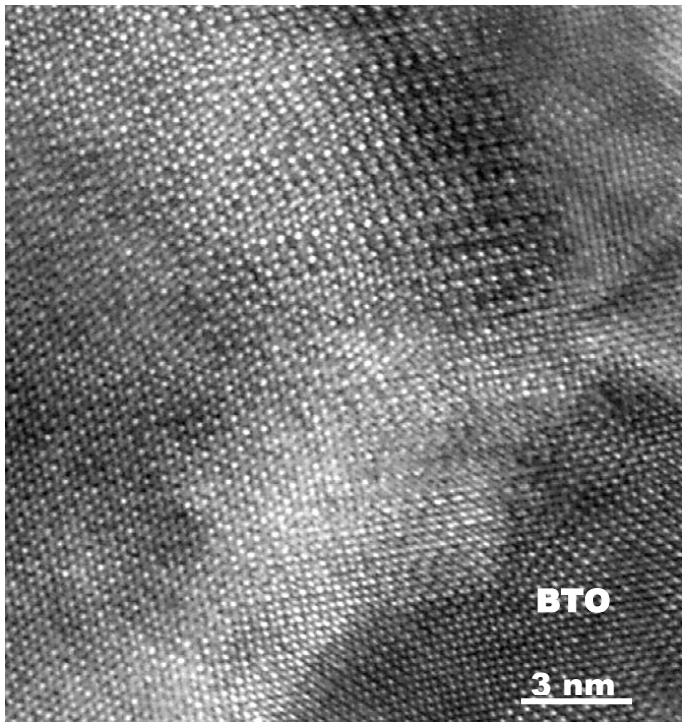

Fig.3.19 Plan view high resolution TEM image taken from the sample grown at 950 ºC with a thickness of ~20 nm.

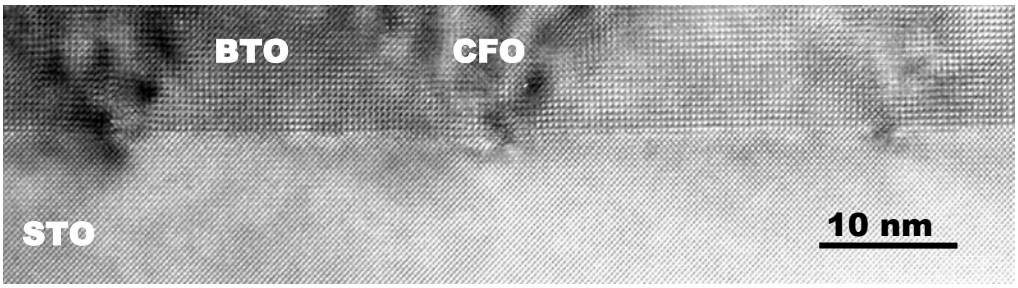

Fig.3.20 High resolution cross section TEM image taken from the sample grown at 950 ºC with a thickness of ~400 nm.

3.5 The growth of $BaTiO_3$-$CoFe_2O_4$ nanostructures on different substrates

In order to study the effect of lattice mismatch strain on the formation of the nanostructure array, $BaTiO_3$-$CoFe_2O_4$ thin films were deposited on various substrates: $LaAlO_3$ (001), $MgAl_2O_4$ (001), MgO (001), and $SrTiO_3$ (001). The structures of the substrates and lattice mismatch with respect to $BaTiO_3$ and $CoFe_2O_4$ are listed in Table 3.1. As listed in the table, there is considerable variation in the lattice mismatch strain between the two compounds in the film ($BaTiO_3$ and $CoFe_2O_4$ phases) and the four different substrates. To ensure that the films had the same growth conditions on the different substrates, films were deposited on the four different substrates during the same deposition run.

Table 3.1 Lattice parameters and lattice mismatch in the films.

Substrate	Structure	Lattice parameter a (Å)	Lattice mismatch (%)with $BaTiO_3$ (a=3.99 Å; c=4.04 Å)	Lattice mismatch (%) with $CoFe_2O_4$ (a=8.38 Å)
$LaAlO_3$	perovskite	3.79	- 5.28	- 10.55
$SrTiO_3$	perovskite	3.905	- 2.18	- 7.30
$MgAl_2O_4$	spinel	8.08	+ 1.24	- 3.71
MgO	rock salt	4.213	+ 5.29	+ 0.55

* The lattice mismatch strain (ε) is calculated using: $\varepsilon = \frac{a_{sub} - a_{film}}{a_{sub}}$. For the lattice mismatch strain between $CoFe_2O_4$ and $LaAlO_3$, $SrTiO_3$ or MgO, we use $\varepsilon = \frac{2a_{sub} - a_{CoFe_2O_4}}{2a_{sub}}$.

Fig.3.21 shows X-ray θ-2θ diffraction spectra from the films grown on the different substrates at a temperature of 950 ºC. All the films have a thickness of 320 nm. The spectra from films grown on $SrTiO_3$, MgO and $MgAl_2O_4$ substrates show only (00*l*) peaks from $BaTiO_3$ and $CoFe_2O_4$ phases. Extra peaks such as $BaTiO_3$ (111), $CoFe_2O_4$ (220) were identified in the film grown on $LaAlO_3$ substrate. Both plan view and cross section TEM studies were conducted to resolve the differences in the nanostructures of the films.

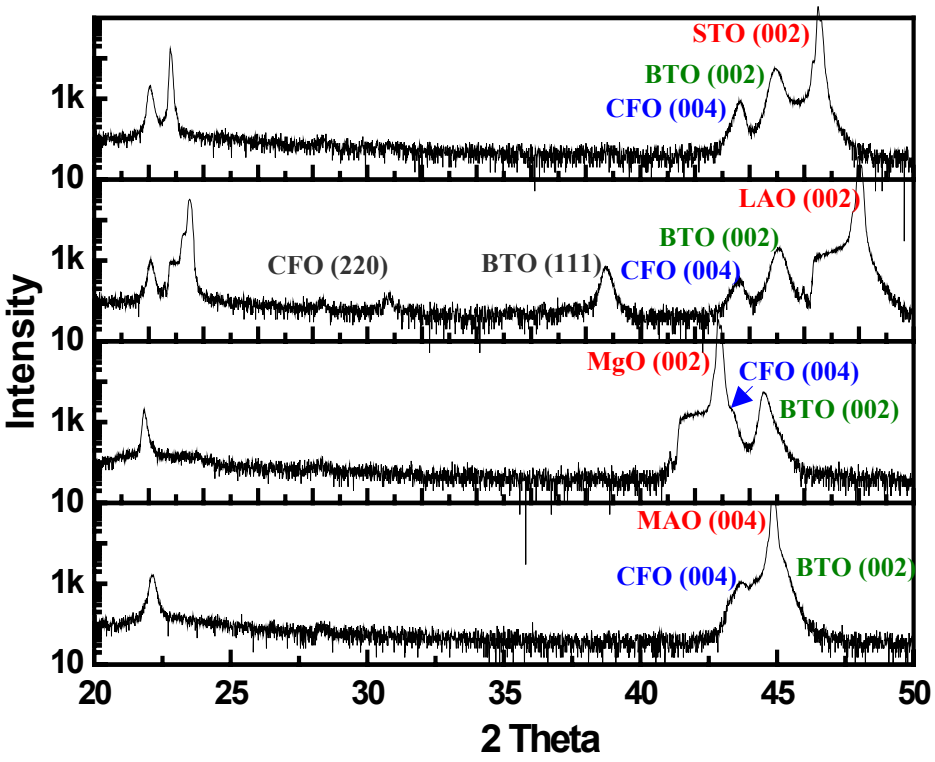

Fig.3.21 X-ray θ-2θ diffraction spectra of the films grown on various substrates: A. MgO; B. $SrTiO_3$; C. $MgAl_2O_4$; and D. $LaAlO_3$. All the samples were deposited at 950 ºC with a thickness of 300 nm. $CoFe_2O_4$ (CFO) (004) peak is overlap with MgO (002) and $BaTiO_3$ (BTO) (002) peak is overlap with $MgAl_2O_4$ (004).

Fig.3.22 A-D are plan-view TEM images taken from the samples grown on the different substrates. No significant morphological differences are observed in the TEM images from the samples grown on $SrTiO_3$, MgO and $MgAl_2O_4$ substrates. As shown in Fig.3.22 A-C, $CoFe_2O_4$ pillars with diameters of 30-40 nm are embedded in a $BaTiO_3$ matrix. By changing the growth temperature, the size of the pillar decreases as the growth temperature is reduced, which is similar to the behavior of the films deposited on $SrTiO_3$ substrates (see section 3.3). In contrast, the film grown on

$LaAlO_3$ shows a different morphology (see Fig.3.21D). Namely, $CoFe_2O_4$ pillars with a diameter of 60-70 nm are observed. In addition, (111) oriented $BaTiO_3$ and (220) oriented $CoFe_2O_4$ were observed in electron diffraction patterns from the sample grown on $LaAlO_3$ in agreement with the XRD results. The lattice parameters (c axis value) calculated from both electron diffraction patterns and XRD spectra are listed in Table 3.2.

Table 3.2 Lattice parameters calculated from XRD and TEM diffraction pattern.

Substrate	Structure	Calculated c of $BaTiO_3$ (±0.005 Å)	Calculated c of $CoFe_2O_4$ (±0.005 Å)
$LaAlO_3$	perovskite	4.02	8.30
$SrTiO_3$	perovskite	4.03	8.30
$MgAl_2O_4$	spinel	4.01	8.28
MgO	rock salt	4.06	8.34

As seen from the table, when there is compressive strain in both phases in the film, as in the film deposited on $SrTiO_3$ and $LaAlO_3$ substrates, the lattice parameter *c* values of the two phases in the film are smaller compared with their bulk values. The lattice parameter c values of the two phases in the film on MgO substrate show larger values than their bulk values, which indicate there is tensile strain in the film phases induced from the substrate. However, phases of the films on $MgAl_2O_4$ substrate show both tensile and compressive strain. It implies complex effects of lattice mismatch strain on the $BaTiO_3$-$CoFe_2O_4$ thin film nanostructures. The film on $LaAlO_3$ substrate lost epitaxial features because of the very large lattice mismatch strain between the film and the substrate.

It is worth mentioning that the interface in the film grown on the $MgAl_2O_4$ substrate is very rough. Fig.3.23 is a cross section high resolution TEM image taken from a sample grown at 950 ºC on an $MgAl_2O_4$ substrate. The interface has a zigzag

shape and the facets at the rough interface are identified as {111} type of planes. The formation of the {111} type facets is most likely due to its relatively low surface energy. The surface energies[115] for spinel $MgAl_2O_4$ are 1446 erg/cm^2 for {100}, 2702 erg/cm^2 for {110}, and 298 erg/cm^2 for {111}. Thus the {111} planes have much lower surface energy than the other main crystallography planes. At high temperature the surface of the $MgAl_2O_4$ re-structures and forms {111} type of facets in order to reduce the surface energy. The film close to the $MgAl_2O_4$ substrate shows intertwined banded $BaTiO_3$ and $CoFe_2O_4$ phases. However, the epitaxial orientation relationship of $(100)_{BaTiO3}//(100)_{CoFe2O4}//(100)_{MgAl2O4}$ remains. As the thickness of the film increases, the film forms well-organized $CoFe_2O_4$ pillars in a $BaTiO_3$ matrix.

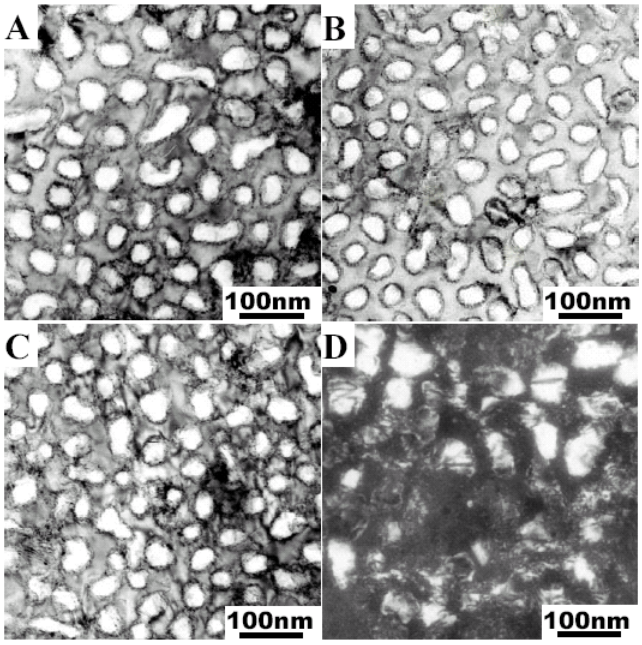

Fig.3.22 Plan view TEM images taken from the films grown on various substrates: A. MgO; B. $SrTiO_3$ (STO); C. $MgAl_2O_4$ (MAO); and D. $LaAlO_3$ (LAO). All the films were deposited at 950 ºC with a thickness of 300 nm.

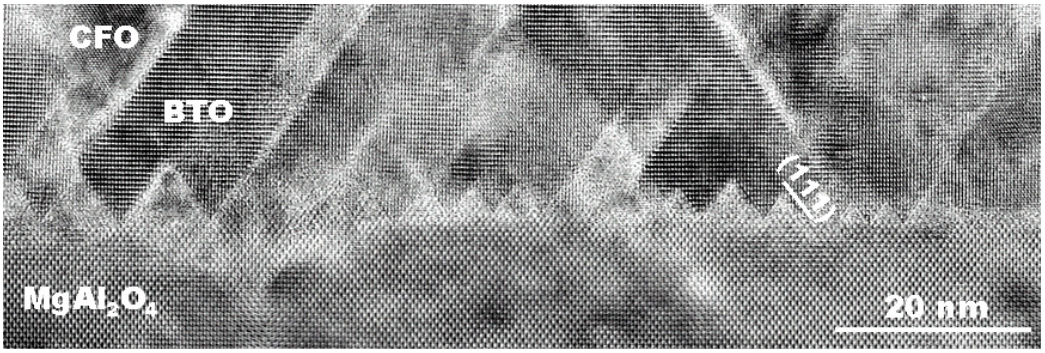

Fig.3.23 Cross-section high resolution TEM image taken from the film grown on $MgAl_2O_4$ substrate at 950 ºC.

In summary, the formation of $BaTiO_3$-$CoFe_2O_4$ nanostructures is intrinsic during heteroepitaxial growth and is fairly independent of the substrate within a certain range of lattice mismatch strain.

3.6 Annealing effect

$BaTiO_3$-$CoFe_2O_4$ nanostructures are very stable at room temperature. Furthermore, there was no obvious change of the microstructures when the films were annealed at temperatures below the growth temperature. However, when the films were annealed at a temperature higher than the film growth temperature, structural changes were observed. Films that were deposited on MgO substrates at 700 ºC and annealed at 950 ºC for 2 hours were studied using XRD and TEM. As we discussed in section 3.3 no separation of $BaTiO_3$ and $CoFe_2O_4$ phases was observed in films grown at temperatures below 700 ºC. These films have a supersaturated $BaTiO_3$ structure

with incorporation of $CoFe_2O_4$. After the samples were annealed, distinct $BaTiO_3$ and $CoFe_2O_4$ phases precipitated from the supersaturated phase.

Fig.3.24A is a plan view TEM dark field image using g = [100] from the $BaTiO_3$ phase, which was taken from the sample grown on an MgO substrate at 700 ºC and annealed at 950 ºC for 2 hours. The figure shows $CoFe_2O_4$ phase (in dark) embedded in the $BaTiO_3$ (in bright) matrix. In the annealed samples $CoFe_2O_4$ did not form nanopillars as we observed in the films deposited at high temperature without annealing. Selected area diffraction pattern (Fig.3.24B) shows extra sets of spots in addition to the ones from (001) $BaTiO_3$ and (001) $CoFe_2O_4$ phases from the film. The extra spots are indexed to be polycrystalline diffractions. Also, there is a slight misorientation of the phase observed from the broadening of the spots into arcs. The structure of the annealed sample is distinctly different from the structures grown directly at high temperature. Fig.3.24D and C are, respectively, a plan view TEM image and a selected area diffraction pattern taken from a sample grown on MgO substrate at 950 ºC. Well-organized $CoFe_2O_4$ pillars embedded in $BaTiO_3$ are observed in Fig.3.24D. Only two sets of spots corresponding to (001) $BaTiO_3$ and (001) $CoFe_2O_4$ phases are observed in the diffraction pattern, which shows the epitaxial features of the film.

The annealing results suggest that the formation of the three-dimensional epitaxial $BaTiO_3$-$CoFe_2O_4$ nanostructures is unique to the thin film deposition process. The formation of $CoFe_2O_4$ nanopillars in $BaTiO_3$ matrix is the consequence of phase separation within the film surface during film deposition.

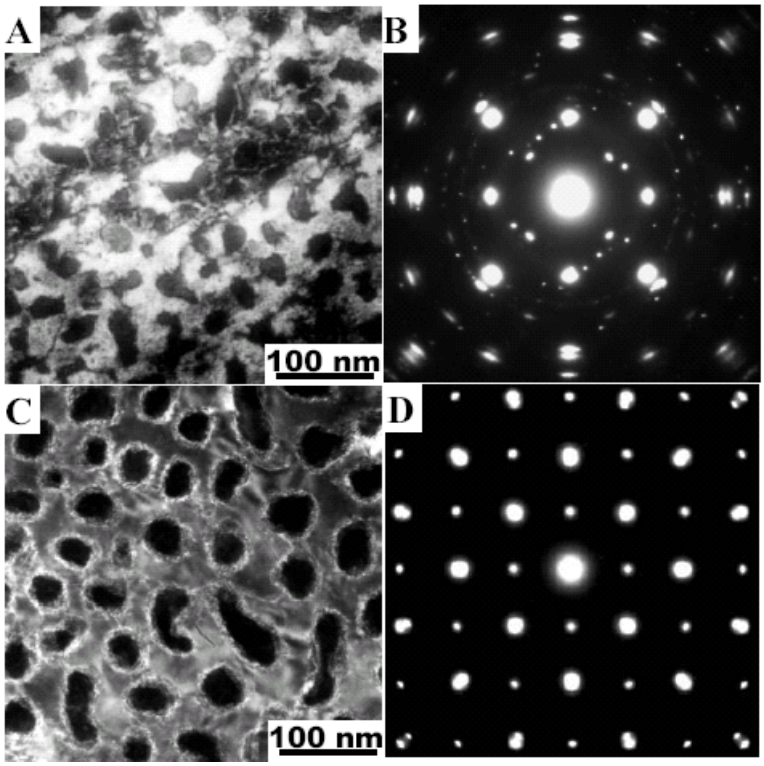

Fig.3.24 A and B. Plan view TEM dark field image using g = [100] from $BaTiO_3$ phase and selected area diffraction pattern, respectively, which were taken from the sample grown at 700 ºC and subsequently annealed at 950 ºC for 2 hours; C and D Plan view TEM dark field image using g= [100] from $BaTiO_3$ phase and selected area diffraction pattern, respectively, which were taken from the sample grown at 950 ºC without annealing. Both films were deposited on MgO substrates and have a thickness of about 300 nm.

Chapter 4 Electric and Magnetic properties

4.1 Ferroelectric/piezoelectric/dielectric properties in $BaTiO_3$-$CoFe_2O_4$ nanostructures

In chapter 3, we discussed the evolution $BaTiO_3$-$CoFe_2O_4$ nanostructures grown at various conditions. In this chapter, the ferroelectric and magnetic properties as well as the coupling effect of the two order parameters are reported. Since well-organized $CoFe_2O_4$ nanopillars formed only above a certain thickness during growth, the electric and magnetic properties as well as the magnetoelectric coupling effect in the nanostructures were carefully investigated on films with a thickness of 400 nm. The ferroelectric and magnetic properties of the films at various growth conditions, i.e., different growth temperatures, different thickness, etc. are also discussed.

The ferroelectric measurements of the nanostructured thin films were made on films deposited on (001) $SrTiO_3$ substrates with 200 nm $SrRuO_3$ as bottom electrodes and ~100 nm platinum top electrodes. Vertical transport measurement yields a resistivity of ~$6x10^9$ Ω-cm at zero bias for all films. This reasonably high value of the resistivity enables high field polarization measurements from the films. Fig.4.1 shows the ferroelectric P-E hysteresis loops obtained from a sample grown at 950 °C with a film thickness of 400 nm. The measurements were conducted with different applied voltages at a frequency of 15 kHz. The hysteresis loops demonstrate well-defined ferroelectric hysteresis with saturation polarization (P_s) of 23 μC/cm^2, which was normalized to the volume fraction of $BaTiO_3$ (~65%). The remanent polarization P_r was 8 μC/cm^2 and the coercive field E_c was 6.2 MV/m.

Both piezoelectric force microscopy (PFM) and d_{33} measurements were conducted to study the piezoelectric properties of the nanostructures. Switching of

polarization was clearly observed in the PFM images. Quantitative piezoelectric measurements of d_{33} reveal a clear hysteresis loop as shown in Fig.4.2 The hysteresis in the piezoresponse signal is directly associated with the polarization switching and ferroelectric properties of the sample. A maximum piezoelectric coefficient d_{33} value of 50 pm/V was observed from films grown at 950 °C, compared to the bulk value of 130 pm/V for single crystal $BaTiO_3$. This decrease is believed to be primarily due to clamping effects from both the substrate and the $CoFe_2O_4$ nanopillars[69]. The decrease in d_{33} at high electric fields is a consequence of the field-induced lattice hardening, which is typical of perovskite piezoelectrics[116].

The nonlinear dielectric properties of the $BaTiO_3$-$CoFe_2O_4$ nanostructures were studied by plotting the variation of dielectric constant at different applied voltages. A small signal with 50 mV amplitude and frequency of 100 kHz was applied across the film thickness while a dc field was swept from positive bias to negative bias and back again. A maximum dielectric constant of ~220 was observed from films grown at 950 °C in Fig.4.3A. Normalization to the volume fraction of $BaTiO_3$ yields a dielectric constant value of ~338. A relatively small coercive field of only 1 MV/m was obtained from the capacitance data, which does not agree with the value obtained from the P-E loops. This discrepancy is probably due to the fact that these two measurements were performed at different frequencies[117]. The dielectric constant measurement was conducted at a frequency of 100 kHz, while the hysteresis loop was measured with two triangular waves of 0.06-1 msec corresponding to 1-15 kHz. Fig.4.3B depicts the frequency dependence of the dielectric constant in the frequency range of 50 kHz to 1 MHz. The frequency dependence measurements are restricted to less than 1 MHz due to the limitation of the equipment.

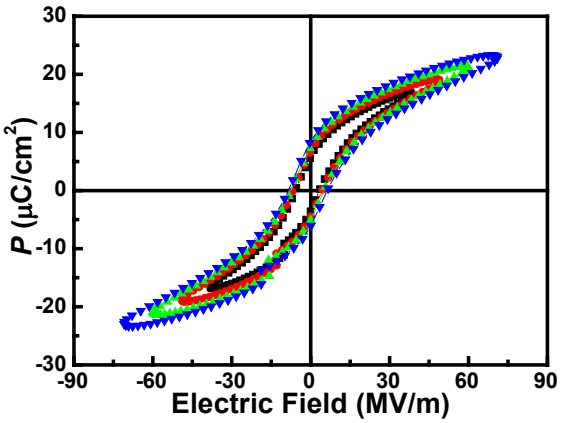

Fig.4.1Polarization-electric field (P-E) hysteresis loop of $BaTiO_3$-$CoFe_2O_4$ nanostructures grown at 950 °C with a thickness of 400 nm.

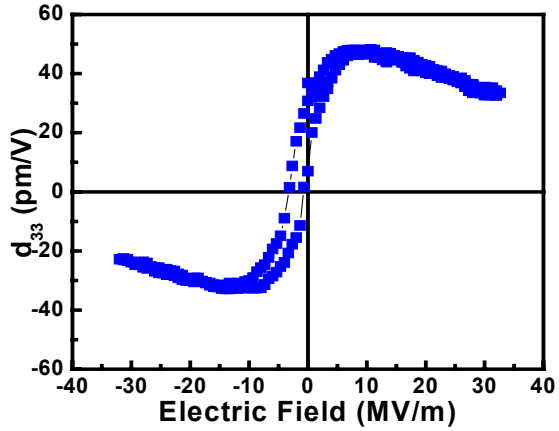

Fig.4.2 Small signal piezoelectric d_{33} hysteresis loop for a 50 μm diameter capacitor from a film grown at 950 °C with a thickness of 400 nm.

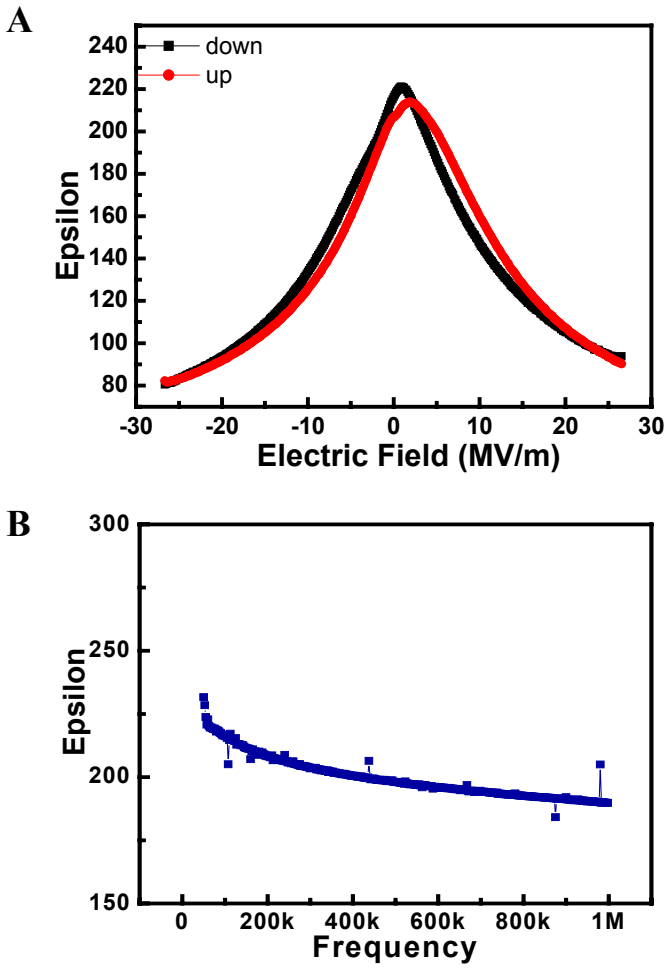

Fig.4.3 A. Dielectric constant (ε) vs electric field (V); B. Frequency dependence of dielectric constant at V=0 of a film grown at 950 °C with a thickness of 400 nm.

The effect of thickness on the ferroelectric properties was studied in the $BaTiO_3$-$CoFe_2O_4$ nanostructures. Fig.4.4 shows the remanent polarization (P_r), coercive field (E_c) and dielectric constant (ε) at various film thickness. The figure shows that as the film thickness increases, the remanent polarization and dielectric constant increase while the coercive field decreases. The thickness dependence of the

coercive field (E_c) can be well explained by the semi-empirical law[118,119], $E_c(d) \propto d^{-\frac{2}{3}}$. This semi-empirical scaling law has been used successfully to describe the thickness dependence of the coercive field in ferroelectric films ranging from 200nm to 100 μm. In the derivation of this scaling, it is assumed that there is no internal electric field in the ferroelectric film so that the coercive field measured in the external circuit is identical to that in the film itself. In reality, screening charges in the electrode are always distributed over a small but finite region, resulting in incomplete compensation.

The thickness dependence of the electric properties of $BaTiO_3$-$CoFe_2O_4$ nanostructures is consistent with the "size effects" on continuous thin film ferroelectrics that have been reported in the literature[120,121,122,123]. There are two models that have been traditionally used to describe the size effect, namely an "intrinsic" effect[124,125,126] and a "depoling field" effect[121, 127,128,129,130]. The "intrinsic" effect includes internal strain effects, surface/interface effects, and effects from defects such as dislocations, non-stoichiometric phases, etc. The main contribution to the intrinsic effects comes from internal stress that changes the ferroelectric properties of the films[131,132]. The stress state in the $BaTiO_3$-$CoFe_2O_4$ nanostructures as a function of film thickness is difficult to describe due to the different crystal orientations and phases presented in the film when the film is very thin (see section 3.4). The second intrinsic contributing factor comes from surface and interface effects, such as the space-charge layer induced by an applied electric field. Fujii and Sakudo[133] reported that the external electric fields produced some kind of surface layer that decreased the dielectric constant of $KTaO_3$. Roberts[134] also reported that the dielectric constant of $BaTiO_3$ ceramics was halved with the application of an electric field. The surface/interface to volume ratio increases dramatically as the film thickness

decreases in our $BaTiO_3$-$CoFe_2O_4$ nanostructures and this effect can account for the thickness dependence of the electric properties observed in our films. Lastly, prominent defects in our films such as dislocations and nonstoichiometric phases can also suppress the polarization and dielectric constant while increasing the coercive filed.

The thickness dependence of the ferroelectric properties in the $BaTiO_3$-$CoFe_2O_4$ system can also be explained by a "depoling field" effect. This effect consists of a depolarizing electrostatic field caused by dipoles at the ferroelectric – electrode interface[121]. This effect is more prominent at small thickness, which can lead to the disappearance of ferroelectricity. Since ferroelectricity is a cooperative phenomenon, it is reasonable that it is suppressed at small film thickness.

The ferroelectric properties of $BaTiO_3$-$CoFe_2O_4$ nanostructure at various growth temperatures were also studied. Our results show that polarization increases with the increase of growth temperature. This is due to the increase in lateral dimensions of the $BaTiO_3$ phase as the spacing between $CoFe_2O_4$ nanopillars increases at higher growth temperatures. Therefore, suppressed ferroelectric properties in films grown at low temperatures can be explained by a "size effect" as discussed above.

In summary, the ferroelectric properties of $BaTiO_3$-$CoFe_2O_4$ nanostructures were investigated as a function of film thickness and growth temperature. Films grown at high temperature and with large film thickness show superior ferroelectric properties in contrast to the thin films grown at low temperatures. "Size effect" such as internal stresses and surface/interface effects are believed to be the primary sources of degradation of the ferroelectric properties of the films.

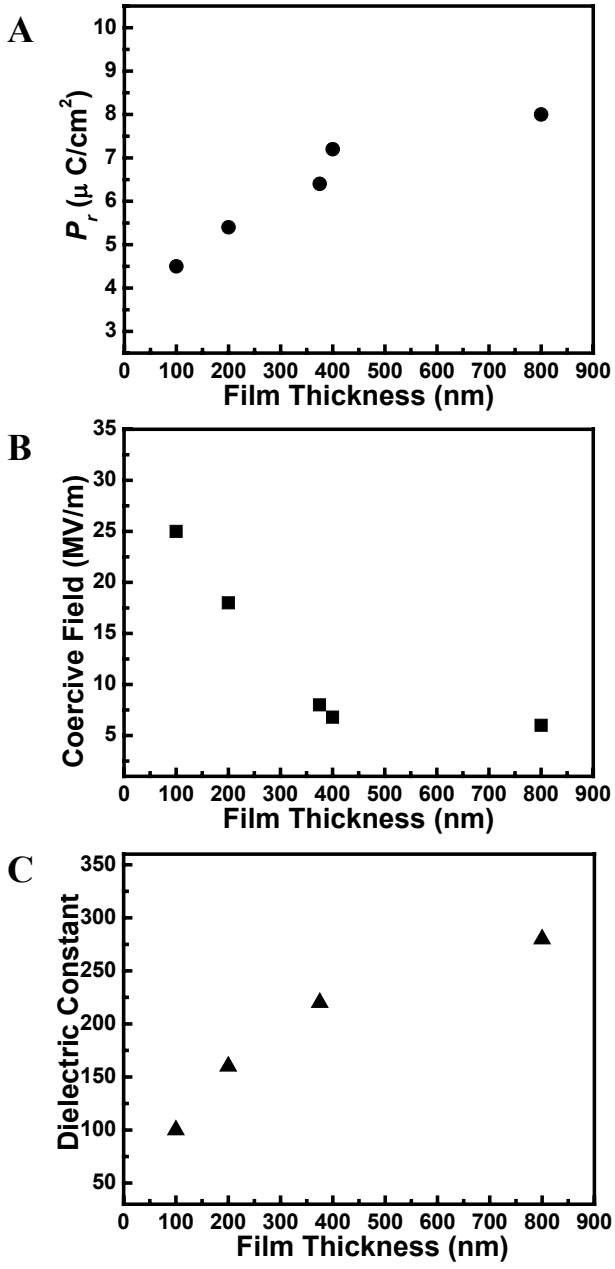

Fig.4.4 Thickness dependence of A. polarization (P_r); B. coercive field (E_c); and C. dielectric constant (ε) measured at 100 kHz in $BaTiO_3$-$CoFe_2O_4$ nanostructures.

4.2 Magnetic properties of $BaTiO_3$-$CoFe_2O_4$ nanostructures

4.2.1 Magnetic properties and magnetic anisotropy in $BaTiO_3$-$CoFe_2O_4$ nanostructures

$CoFe_2O_4$ has the highest values of magneto-crystalline anisotropy and magnetostriction of all spinel ferrites[135]. As it is discussed in chapter one, $CoFe_2O_4$ is a cubic ferrimagnetic material with an inverse spinel structure. The octahedral B sites are shared between 8 Co^{2+} and 8 Fe^{3+} cations, while the tetrahedral A sites are occupied by the remaining 8 Fe^{3+} cations. When transition metal ions with an orbitally degenerate ground state, such as Fe^{2+} ($3d^6$) and Co^{2+}($3d^7$), are incorporated into the ferrite lattice, the degeneracy of the ground state is lifted by both local crystalline field and the spin-orbit coupling. This lifting of degeneracy leads to energy levels that depend on the direction of magnetization. Such effects enhance magnetocrystalline anisotropy and the anisotropy of the magnetostriction[136], as exhibited in bulk $CoFe_2O_4$. Due to its large magnetic anisotropy and magnetostriction, $CoFe_2O_4$ has potential use in magnetic media applications. It was also reported that the high value of magnetic anisotropy in epitaxial $CoFe_2O_4$ thin films makes it suitable as an exchange bias layer to stabilize the domain state of magnetically soft ferrites[137]. There has been extensive research on $CoFe_2O_4$ thin films, i.e. polycrystalline[138], nanoparticle[139, 140], and epitaxial[136,141,142,143] thin films grown by various methods. However, to our knowledge the magnetic properties in the present nanostructure of $CoFe_2O_4$ thin films have not been reported prior to this work.

The magnetization (*M*) vs field (*H*) loops were measured using Superconducting Quantum Interference Device (SQUID) magnetometry. Fig.4.5 shows the hysteresis loops with magnetic field applied in the plane of the film along [100] and out of the plane along [001] from a 400 nm thick sample grown at 950 ºC. The sample was

deposited on a (100) $SrTiO_3$ single crystal substrate with a 200 nm $SrRuO_3$ bottom electrode. When normalized to the volume fraction of $CoFe_2O_4$, ~35%, the film has a saturation magnetization (M_s) of ~350 emu/cm^3. The magnetization loop along the [001] direction is almost square with a coercive field of ~5 kOe. The remnant magnetization is 297 emu/cm^3, which is about 85% of M_s. In contrast, the loop along the [100] direction is almost a straight line with near-zero remanence and coercivity. A strong magnetic anisotropy favoring the out-of-plane [001] direction against the in-plane [100] direction was observed. Linear extrapolation of the in-plane magnetization yields a uniaxial anisotropy field of ~35 kOe.

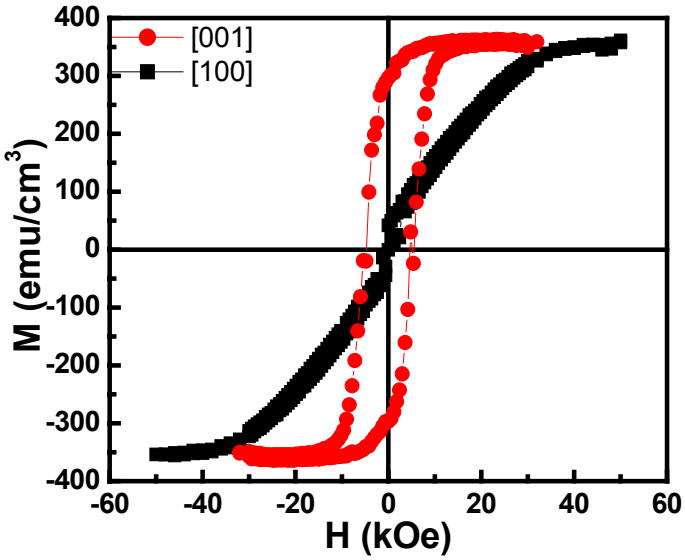

Fig.4.5 Out of plane [001] and in plane [100] magnetic hysteresis loops depicting a very large uniaxial anisotropy from a ~400 nm $BaTiO_3$-$CoFe_2O_4$ nanostructured film grown at 950 °C.

Magnetic anisotropy energy of the $CoFe_2O_4$ nanopillars may has the following contributions: (i) magnetocrystalline effects due to the crystal structure; (ii) shape

effects due to the nanopillar aspect ratio; (iii) magnetoelastic effects induced by strain; (iv) other effects, such as surface effects[144,145], configuration effects[146,147,148,149], or interactions between pillars[150,151,152].

Firstly, no magnetocrystalline anisotropy is expected between [001] and [100] directions for cubic $CoFe_2O_4$. Secondly, the shape anisotropy field of the $CoFe_2O_4$ nanopillars was calculated. Since the $CoFe_2O_4$ pillars have an aspect ratio of c/a ~10, the demagnetization factor[153] for a cylinder with aspect ratio of 10 is taken to be N_z = 0.0172. The associated anisotropy energy is: $E_{shape} = 2\pi(N_x - N_z)M_s^2$, where $N_x = (1-N_z)/2$. For a saturation magnetization (M_s) of ~350 emu/cm^3 the shape anisotropy field is calculated to be: $H_{shape} = 2E_{shape}/M_s$ ~ 2.1 kOe, which is significantly smaller than the experimentally observed value. Thus the strong perpendicular anisotropy can be explained in terms of a strong contribution of stress anisotropy. The present film has a compressive strain of ε = 0.8% along the growth direction [001] of the $CoFe_2O_4$ pillars as determined from XRD and TEM analysis. There are two possible sources that may induce such compressive stain in the nanostructures. The first source is the mismatch between the $CoFe_2O_4$ and $BaTiO_3$ lattices at the growth temperature ($\Delta\varepsilon_T$). High resolution TEM images (Fig.3.6C) show that part of this mismatch is accommodated by the formation of interface dislocations. The second source is the lattice distortion in the $CoFe_2O_4$ as a consequence of the cubic-tetragonal structural distortion in the $BaTiO_3$ matrix below the ferroelectric Curie temperature T_c = 390 K ($\varepsilon_0^P(P)$). This contribution decreases the compressive strain along the axis of the $CoFe_2O_4$ nano-pillars. The compressive strain in the $CoFe_2O_4$ lattice is related to the magnetic anisotropy through its magnetostrictive effect and gives rise to a magnetoelastic energy as calculated below. The stress in the $CoFe_2O_4$ is given by: $\sigma_{001} = Y\,\varepsilon_{001}$, in which Y is Young's modulus (~141.6 GPa[154]) and ε_{001} is the

experimentally obtained strain along the [001] direction. The magnetoelastic energy associated with this stress is $e = -3\lambda_{001}\sigma_{001}/2$, where λ_{001} is the magnetostriction coefficient of $CoFe_2O_4$ (taken to be $\lambda_{001} \sim -350\times10^{-6}$)[154], leading to a magnetoelastic anisotropy energy of 5.95×10^6 erg/cm^3. The anisotropy field is given by $H_{stress} = 2e/M_s$ = 34 kOe, which is in very good agreement with our experimentally observed value of ~35 kOe. Therefore, our results show that the magnetic anisotropy in the $BaTiO_3$-$CoFe_2O_4$ nanostructures is dominated by stress-induced anisotropy.

Magnetic force microcopy (MFM) images confirmed the perpendicular anisotropy in the nanostructures. Fig.4.6 shows the topography and MFM image of a $BaTiO_3$-$CoFe_2O_4$ film grown at 950 °C. The sample was poled along [001] (Fig.4.6 A, B) and $[00\bar{1}]$ (Fig.4.6 C, D) directions respectively before imaging. The images were taken from a 2 μm × 2 μm area. The lateral resolution of the AFM image (10~20 nm) is higher than the tip curvature (~50 nm). In the MFM images, the dark-colored areas correspond to attraction of the tip, whereas the light-colored areas correspond to repulsion. Areas with the same color present similar response to the tip. Domain-like areas of up to a few hundred nanometers in size with alternated contrast are observed in the MFM images. Continuous magnetized areas are observed in such highly discontinuous system. This is probably because of the difference in spacing between the nanopillars. It is possible that the high density of the $CoFe_2O_4$ nanopillars induced dipolar interaction[155,156]. Groups of closely packed neighboring pillars behave like single domains because their magnetizations are coupled through an exchange interaction mechanism. Switching of the magnetization was clearly observed in the MFM images. Since the sample was measured at the remanent state, the

magnetization was relaxed in some regions during the measurement, and thus only some of the nanopillars remain switched in the MFM images.

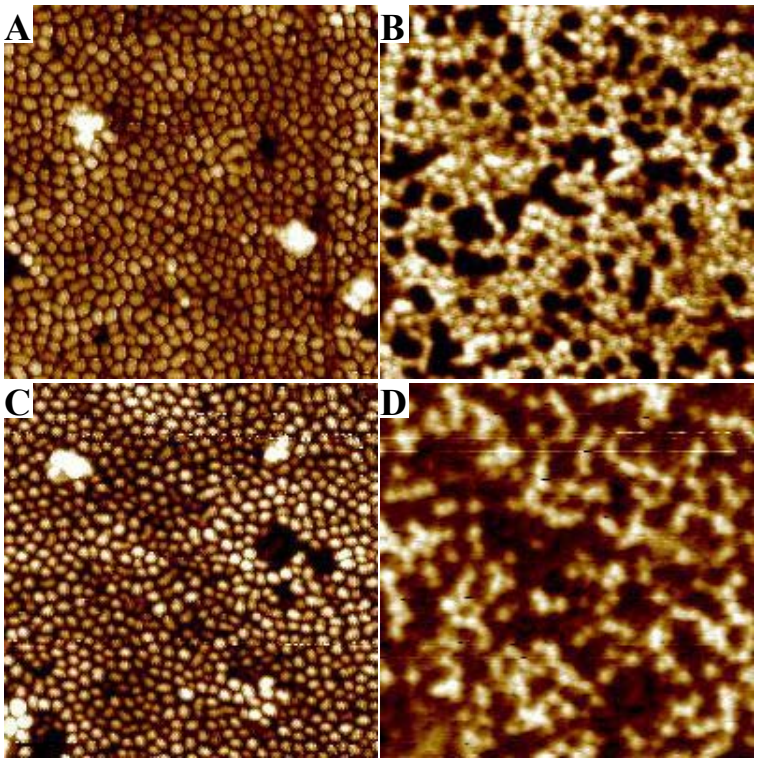

Fig.4.6 AFM and MFM images taken from a film grown at 950 °C with a thickness of about 400 nm. A. 2 × 2 μm AFM image; B. MFM image corresponding to A.; C. 2 μm × 2 μm AFM image; D. MFM image corresponding to C. The sample was poled along [001] direction (B) and $[00\bar{1}]$ direction (D) respectively before imaging.

One of the possible applications of this nanostructured films is as a perpendicular storage medium. However, the observed interaction between nanopillars indicates that the magnetic field is not localized in a single pillar. Therefore, it is not possible to record information on the present array configuration unless the spacing between individual nanopillars is increased via higher growth

temperatures or via reducing the volume ratio of the $CoFe_2O_4$ phase. This would give a more diluted array of nanopillars in which interaction between neighboring pillars are eliminated due to large interpillar spacing.

4.2.2 Growth temperature dependence of the magnetic properties in $BaTiO_3$-$CoFe_2O_4$ nanostructures

In order to further investigate the role of the stress in the magnetic anisotropy of the nanostructures, magnetic measurements were taken from films grown at different temperatures. As discussed in section 3.3.1, the residual strain in the $CoFe_2O_4$ pillars is different for nanostructures grown at different temperatures. The compressive strain along the $CoFe_2O_4$ pillars decreases as the growth temperature increases. The strain relaxes at higher growth temperatures by forming interface dislocations between the pillars and the $BaTiO_3$ matrix.

Table 4.1 The magnetic anisotropy of the films grown at various temperatures.

Growth Temperature (°C)	Strain (ε) (%)	Stress Anisotropy (kOe)	Anisotropy (Experimental) (kOe)
800	-1.6	106	85
850	-1.4	63	68
920	-1.1	45	51
930	-0.8	34	35

We measured magnetic properties of the films grown at various temperatures. Fig.4.7 shows the magnetization (*M*) vs field (*H*) loops taken from samples grown at 920 ˚C, 850 ˚C and 800 ˚C, respectively. All samples were deposited on (001) $SrTiO_3$ directly. Magnetization data shows a uniaxial easy axis in the out of plane [001] direction for all samples. Since the anisotropy fields are larger than the largest applied field of 5 Tesla, the anisotropy fields were obtained by linear extrapolation from the in-plane and out-of-plane loops (as shown in Fig.4.7).

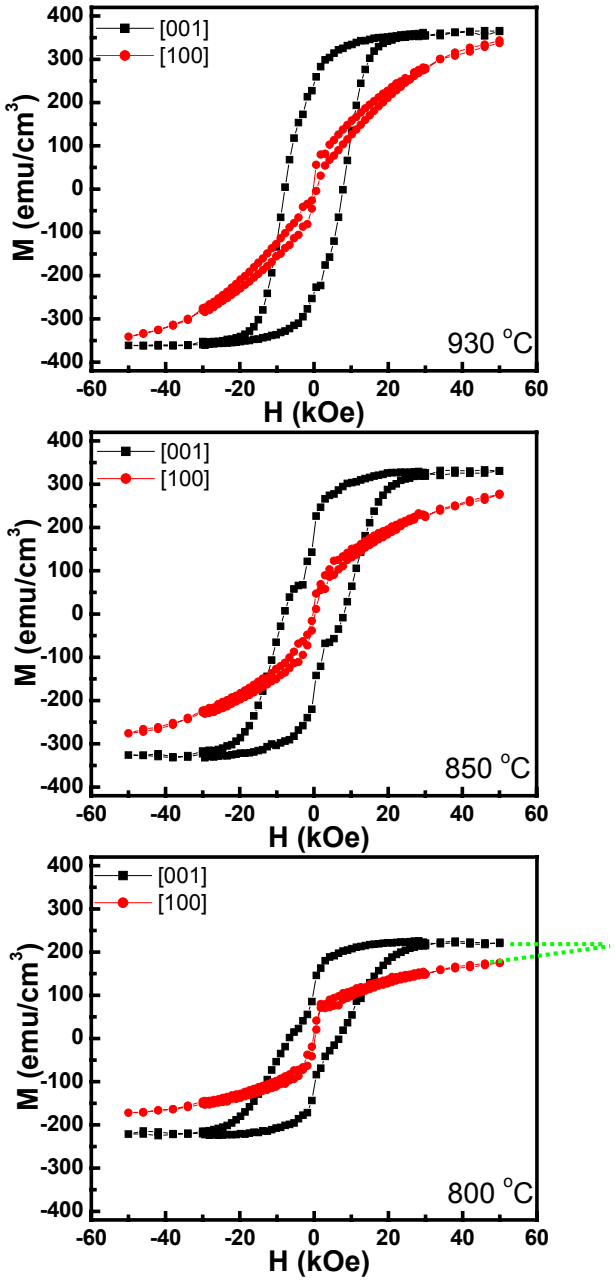

Fig.4.7 Out of plane [001] and in plane [100] magnetic hysteresis loops taken from the samples grown at various temperatures: 930 ˚C, 850˚C and 800 ˚C. All the samples were deposited directly on (001) $SrTiO_3$.

Fig.4.7 shows that as the growth temperature increases the anisotropy field decreases. We attribute the decrease in the anisotropy to the decrease in the residual strain in the $CoFe_2O_4$ nanopillars, which in turn gives a lower stress anisotropy. Table 4.1 shows the strains estimated from our X-ray and electron diffraction data, as well as the estimated stress anisotropy and the experimentally observed anisotropy fields from the samples grown at various temperatures. The calculated stress anisotropy fields are very close to the experimentally observed values for films grown within the temperature range of 850 – 930 °C. In contrast, there is a relatively large difference between the calculated and experimental values for the film grown at 800 °C. One possible reason for this discrepancy is the larger error involved in the calculation due to the linear extrapolation. Another reason may be more complex phenomena involved in the film grown at 800 °C due to the twisting of the $CoFe_2O_4$ pillars and the smaller spacing between the pillars.

The saturation magnetization (M_s), coercive fields and remanent magnetization values along the [001] direction for the films grown at different temperatures are graphed in Fig.4.8. This figure shows that M_s and the remanence increase with increasing growth temperature. However, the M_s is still lower than the bulk value of the $CoFe_2O_4$ (~410 emu/cm^3) even at 930 ˚C. We attribute the reduction of magnetization in $CoFe_2O_4$ nanopillars to the defects in the nanostructures, such as surface spin effect or a dead layer at the interface. Spin canting[157,158,159] as well as spin relaxation[160] at surface/interface can reduce the magnetization and the remanence. In the $CoFe_2O_4$ nanopillar structures there is a large surface to volume ratio that could enhance the effect of spin relaxation. The effect of the surface and interfaces is greater at lower growth temperatures, due to the decrease of the diameter of the pillars. Moreover, the pillars are somewhat twisted and have more steps at the interfaces at

lower growth temperatures as observed in cross-section TEM images. Therefore, a significant decrease in the saturation magnetization is expected for samples grown at low temperatures. coercive fields for the samples grown in the range of 850-930 ˚C are the same regardless of the increasing of lateral size of the nanopillars (from ~25 nm to ~40 nm in diameter) with increasing temperature. In addition to the depressed saturation magnetization, there is a slight decrease of the coercivity in the films grown at 800 ˚C. This is probably due to an increase in dipolar interaction[161] between pillars due to the shorter spacing between the nanopillars when the growth temperature is low.

It is interesting to note that there are distinct kinks in each of the out-of-plane hysteresis loops in Fig.4.7. Also, sudden changes in the magnetization are observed in the in-plane hysteresis loops. The changes of the magnetization are more pronounced in the samples grown at lower temperatures. Several possibilities have been considered that may contribute to the formation of the anomalous hysteresis loops as explained below.

The first possible explanation is that defects in the material, such as surface roughness, crystalline misorientations and impurities can create a multivalleyed and degenerate energy landscape. As a consequence, the system can have different ways to overcome the energy barrier. When an external field is applied to take the hysteresis loop, the system randomly chooses a path through the energy landscape[162].

A second possible explanation for the anomalous hysteresis loops is the presence of impurity magnetic phases in the film. The shape of the loops can be fitted to two magnetic phases in a material, i.e. one harder magnetic phase and one much softer magnetic phase. However, our systematic and careful XRD and TEM analyses did not provide evidence for any second structural phases.

A third possibility could come from a fanning and/or vortex formation of the moments[163,162,164,165]. Namely, at the edge of a circular particle, the spins are not collinear with the bulk magnetization of the particle and they may reverse via the formation of fanning or vortex patterns on lowering the external field. In order to test these possibilities we attempted to obtain MFM images from $CoFe_2O_4$ nanopillar arrays. However, due to the relatively small spacing between the nanopillars in our samples MFM images of individual pillars are hard to obtain (see Fig.4.6). Therefore, we do not have direct evidence of the nucleation of vortices in the nanopillar structures at present. The nucleation of the vortex phase is correlated to the exchange correlation length. Thus, it is normally suppressed in extremely small nanostructures. However, our results show that the nanopillars with smaller diameters have more obvious changes in magnetization.

The fourth possible explanation for the anomalous magnetization hysteresis loops is the magnetic exchange interaction[166,167] between the nanopillars. At low growth temperatures, the spacing between $CoFe_2O_4$ nanopillars is small which results in a strong interaction between pillars. The exchange interaction can explain the smaller coercive field observed in the sample grown at lower temperature such as the sample grown at 800 ˚C in Fig.4.7. Such a simple description is inadequate to parameterize the complex magnetic properties of the system, however.

We propose a fifth possible explanation consisting of a structure with two magnetic layers that can reasonably explain the magnetization behavior in this nanostructured system. As we discussed in chapter 3, there is an intertwined $CoFe_2O_4$ layer close to $SrTiO_3$ substrate interface. The magnetic behavior in the intertwined layer is expected to be different compared to the well-organized nanopillars in the upper part of the film. The magnetic hysteresis loops present the magnetization of the

two layers. Since the thickness of the intertwined layer decreases at higher growth temperatures, a change of magnetization in the hysteresis loop of the nanopillar layer is less obvious in the samples grown at high temperatures. Such speculation is reasonably confirmed by the analysis of the magnetic properties from the samples with different thickness, as discussed in the following section.

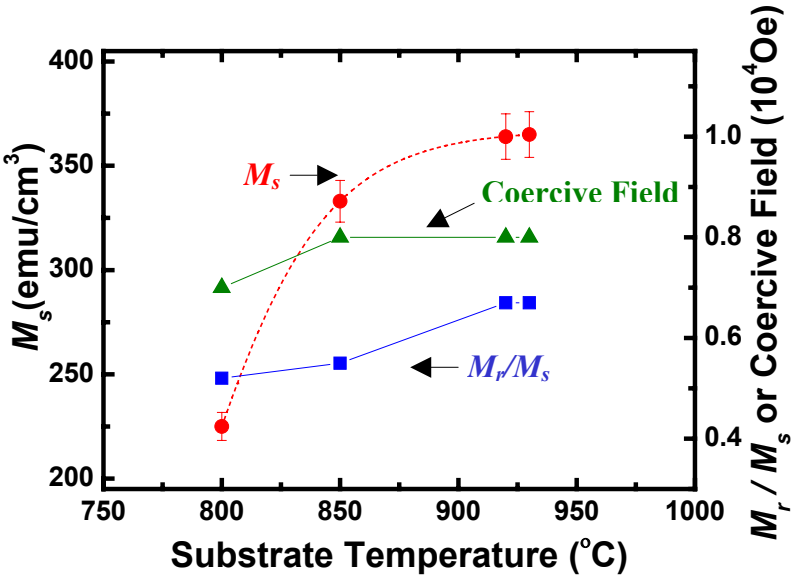

Fig.4.8 Saturation magnetization (M_s), coercive field along the [001] direction and the remanence ratio (M_r / M_s) along the [001] direction as a function of substrate temperature for films grown at 800-930 ˚C. All the films have a thickness of ~400 nm. The lateral size of $CoFe_2O_4$ nanopillars increases from 15 to 40 nm as temperature increases form 800˚C to 930 ˚C. The lines are guides to the eye.

4.2.3 Dependence of the magnetic properties of $BaTiO_3$-$CoFe_2O_4$ nanostructures on film thickness

The magnetic properties of films with various thicknesses were measured using SQUID magnetometry. The results show that films with a thickness less than 50

nm have an easy in-plane axis along the [100] direction. Fig.4.9 shows hysteresis loops for a 50 nm film grown at 930 °C with field applied in the plane along the [100] direction and out-of-plane along the [001] direction. The anisotropy, coercive field and shape of the loops obtained from the thin films are dramatically different from those obtained from the 400 nm thick film as shown in Fig.4.7. The out-of-plane hysteresis loop from the thin 50 nm film shows "bubble" loops, which could be due to the combination of vortex nucleation and domain wall movements. Considering the complex microstructure and the crystalline complexity of the film (see section 3.4), multiple contributions to the magnetization are possible i.e. dipolar interactions, shape effects, intermediate phases, etc.

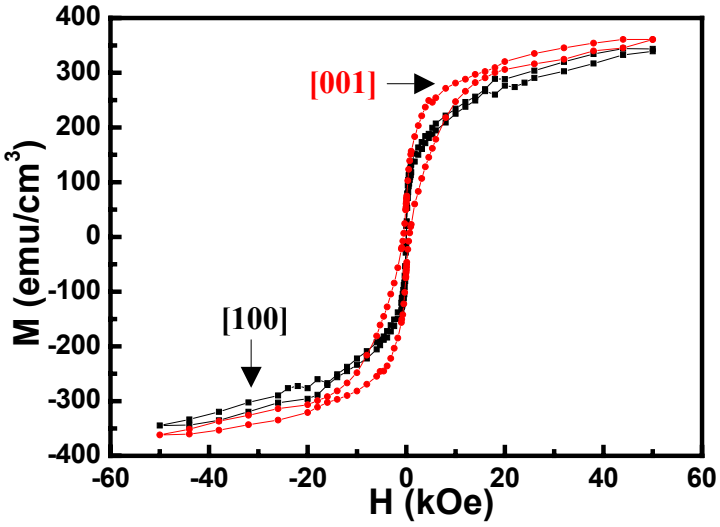

Fig.4.9 Out of plane [001] and in plane [100] magnetic hysteresis loops taken from a sample grown at 930 ˚C with a thickness of 50 nm.

As the thickness of the film increases, well-organized $CoFe_2O_4$ nanopillars form. We expect different magnetic behavior from the nanopillar arrays compared to the intertwined interfacial layer. Therefore, we propose a model consisting of two

magnetic layers in our films. The hysteresis loops from the samples with various thickness show that the easy axis changes from in plane along the [100] direction to out-of-plane along the [001] direction as the thickness of the film increases. Note that the critical thickness is between 50 and 100 nm, and kinks in the hysteresis loops are observed when the film thickness is above 100 nm.

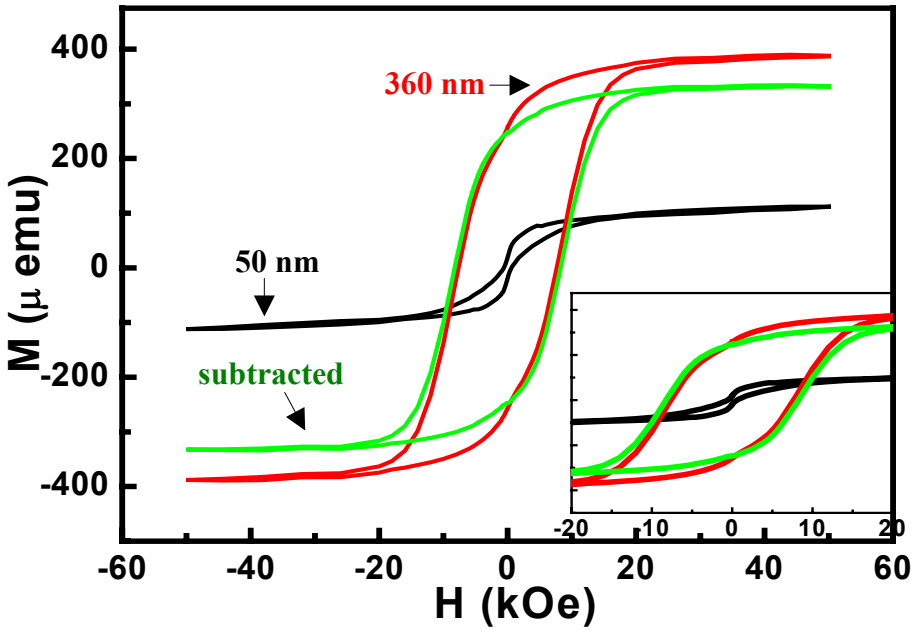

Fig.4.10 Out-of-plane hysteresis loops from the samples with a thickness of about 50 nm and 360 nm film. Subtracting the loop of the 50 nm film from the loop of the 360 nm film gives the subtracted loop. The insert shows the magnified section.

In order to extract the contribution from the upper layer of the film, we subtracted the hysteresis loop obtained from a thin film sample (50 nm) from that of a sample with a thickness of 360 nm in which kinks were observed. Fig.4.10 shows the out-of-plane hysteresis loops from the two samples as well as the subtracted curve between two curves. The subtracted loop is smooth and does not have kinks. Similar results were obtained for the in-plane hysteresis loops. The subtracted hysteresis loop

is considered to have only contributions the $CoFe_2O_4$ nanopillar arrays in the film. As the thickness of the film increases, the volume ratio of the well-organized $CoFe_2O_4$ nanopillars to the intertwined layer increases. Therefore, thicker films have less local contribution from the intertwined interfacial layers that give rise to kinks in the magnetization. Although the magnetic behavior of the thin interfacial layer in a thin film sample could be somewhat different from that in a thicker film, the well-fitted results suggest that our two layers model is correct.

4.2.4 Magnetic properties of $BaTiO_3$-$CoFe_2O_4$ nanostructures grown on various substrates

The magnetic properties of the samples grown on various substrates were also measured. Fig.4.11 shows the out-of-plane and in-plane hysteresis loops taken from films grown at 920 ºC on (001) MgO, (001) $SrTiO_3$, (001) $LaAlO_3$, and (001) $MgAl_2O_4$ substrates. All films show a uniaxial out-of-plane easy axis along the [001] direction regardless of the difference in the substrates. However, the anisotropy, coercive field, and shape of the loops are distinctly different from each other.

The nanostructures on these various substrates were discussed in section 3.5. The heteroepitaxial features of the $CoFe_2O_4$ nanopillars embedded in a $BaTiO_3$ matrix were identified in films grown on MgO, $SrTiO_3$, and $MgAl_2O_4$ substrates, but were not observed in films grown on $LaAlO_3$. The residual strains in $CoFe_2O_4$ nanopillars from samples on MgO and $SrTiO_3$ are, respectively, 0.5% and 1.1% along the long axis of the nanopillars. A calculation of the anisotropy field induced by the magnetoelastic energy yields fields of 24 kOe for the films grown on MgO and 45 kOe for the films on $SrTiO_3$, which are reasonably close to the observed values of 25 kOe for MgO, and 45 kOe for $SrTiO_3$. Therefore, the smaller coercive field and

anisotropy observed from the films grown on MgO are due to the relatively small compressive stress in the nanopillars.

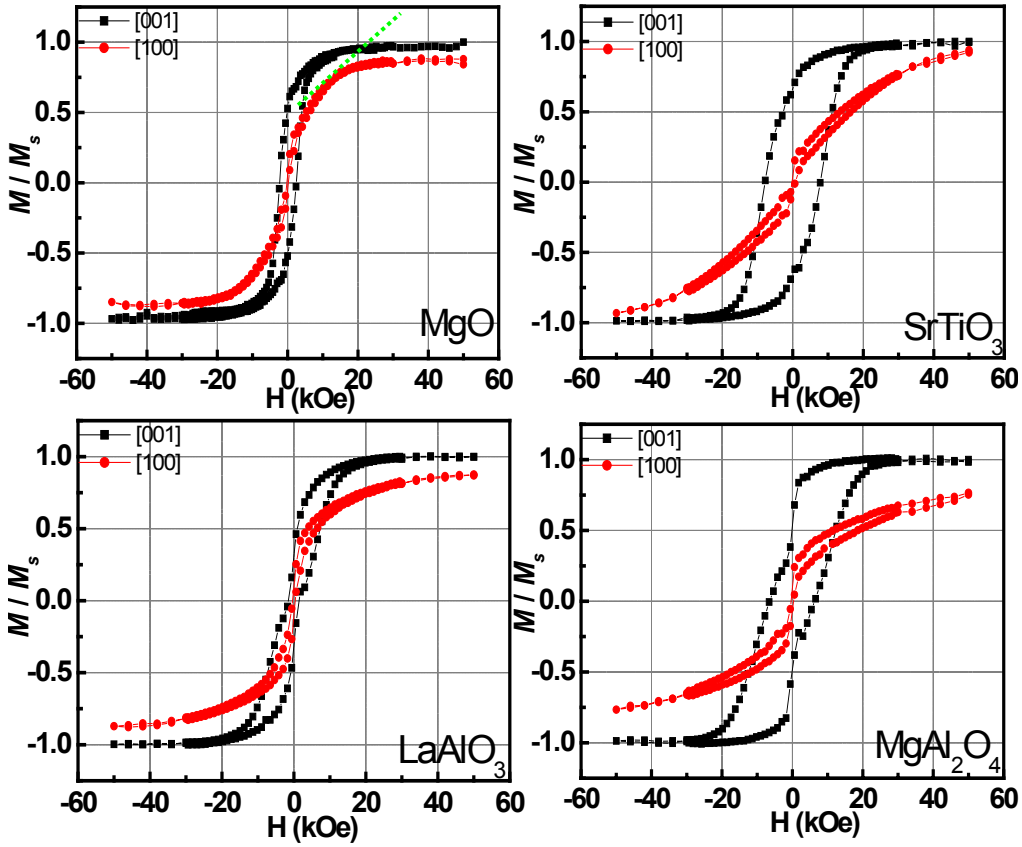

Fig.4.11 Out-of-plane and in-plane magnetic hysteresis loops taken from samples grown at 920 ºC on various substrates: MgO, $SrTiO_3$, $LaAlO_3$ and $MgAl_2O_4$.

The shape of the hysteresis loops from the films grown on $MgAl_2O_4$ is more complicated, and is similar to the loops that we observed from the films grown on $SrTiO_3$ substrate at low temperature (Fig.4.7C). Careful analysis of the nanostructure of the films grown on $MgAl_2O_4$ provides useful information to understand the magnetic behavior of these films. Cross-section TEM images from these samples show that the film on an $MgAl_2O_4$ substrate has a much thicker intertwined layer than

a similar film deposited on $SrTiO_3$. Also, the $CoFe_2O_4$ in the intertwined layer has many triangular shaped steps at the substrate interface as shown in Fig.3.23. The films grown on $MgAl_2O_4$ were the only films in this study that showed this irregular interface. In order to interpret the complex hysteresis loops in the films grown on $MgAl_2O_4$, in addition to the simple model with two magnetic layers (interfacial layer and layer with nanopillars), one must consider magnetic interactions amongst the pillars and the irregular film/substrate interface. In addition, the complex microstructure of the film grown on $LaAlO_3$ makes the interpretation of the magnetic behavior from these difficult to understand by a simple model.

4.3 Magnetoelectric coupling

4.3.1 Thermodynamic analysis of the magnetoelectric coupling in $BaTiO_3$-$CoFe_2O_4$ nanostructures

A thermodynamic analysis of the magnetoelectric (ME) coupling effect in $BaTiO_3$-$CoFe_2O_4$ nanostructures was conducted[54] in this work. For a two-phase magnetoelectric material such as the $BaTiO_3$-$CoFe_2O_4$ thin film system studied in this work, the elastic interactions between the two phases have to be considered in the free energy expression in addition to the ferroelectric and ferromagnetic contributions to the free energy.

Thermodynamic analysis of such a structure has shown that the energy (***e***) due to elastic interactions, including the direct interaction between the phases through the elastic field in the film and the in direct interaction through the substrate, can be given by[168,169,170]:

$$e = G(S_1, S_2, \alpha)(\Delta\varepsilon)^2 / 2 \qquad \text{Eq.4.1}$$

where S_1 and S_2 are the compliances of the two components in the film; α and (1-α) are the fraction of the two phases; G is the effective elastic modulus; and $\Delta\varepsilon$ is the strain. Minimization of the overall elastic energy determines the equilibrium configuration of the system. For rod-like architectures (Fig.1.8B) the main contribution to the elastic interaction energy due to the out-of-plane misfit ($\Delta\varepsilon_\perp$) is given by:

$$e = \frac{1}{2}\alpha(1-\alpha)Y_1Y_2(\Delta\varepsilon_\perp)/[(1-\alpha)Y_1 + \alpha Y_2] \qquad \text{Eq.4.2}$$

where $Y_i = 1/S_i$, is the Young's modulus. The elastic interactions that dictate the morphological configuration of the phases in the film simultaneously determine the coupling between the two order parameters in the phases. For a mixture of ferroelectric and ferro/ferrimagnetic phases this coupling is given by:

$$\Delta\varepsilon = \Delta\varepsilon_T + \varepsilon_0^P(P) + \varepsilon_0^M(M) \qquad \text{Eq.4.3}$$

where $\varepsilon_0^P(P) = QP^2$ is the spontaneous ferroelectric strain, $\varepsilon_0^M(M)$ is the spontaneous magnetostriction, $\Delta\varepsilon_T$ is the lattice misfit at the deposition temperature, (modified by the difference in thermal expansion coefficients) and Q is the electrostriction coefficient. The connection between polarization (*P*) and magnetization (*M*) as well as the dependences of the polarization on the applied magnetic field H *P*(*H*) and the magnetization on the applied electric field E, *M*(*E*), can be obtained from the minimization of the free energy,

$$F = (1-\alpha)[\varphi_P(P) - EP] + \alpha[\varphi_M(M) - HM] + e(\varepsilon_0^P(P), \varepsilon_0^M(M)) \qquad \text{Eq.4.4}$$

where φ_P (φ_M) is the specific free energy of a uniform ferroelectric (ferro/ferrimagnetic) material. It is clear from equation (4.4) that a strong magnetoelectric coupling requires a strong inter-phase elastic interaction.

4.3.2 Magnetoelectric coupling effect in $BaTiO_3$-$CoFe_2O_4$ nanostructures

In this work several experimental approaches to obtain an estimate for the magnetoelectric coupling effect in $BaTiO_3$-$CoFe_2O_4$ nanostructures were carried out. Both indirect measurements, i.e. magnetization vs temperature measurements, and direct measurements of dE/dH using a microwave microscope[171], the MFM imaging under switching of an external electric field[172] were performed.

The magnetization vs temperature measurements were performed with an external field of 100 Oe in the temperature range of 50 – 200 ºC using a vibrating sample magnetometer (VSM). The results are shown in the magnetization vs temperature curve in Fig.4.12. This figure shows a distinct drop in the magnetization of ~16 emu/cm^3 (~5% of the magnetization at 100 Oe external field) at the ferroelectric Curie temperature (T_c = 390 K) of the $BaTiO_3$ matrix. The drop of magnetization in the $CoFe_2O_4$ phase at the $BaTiO_3$ Curie temperature demonstrates that there is coupling between the electric and magnetic order parameters in the nanostructures. At temperatures higher than the ferroelectric Curie temperature, T_c, the $CoFe_2O_4$ is compressed due to the lattice mismatch with $BaTiO_3$. However, for T < T_c, the tetragonal distortion in the $BaTiO_3$ lattice decreases the compression in the $CoFe_2O_4$. Since $CoFe_2O_4$ has a negative magnetostriction, it results in a reduction of the magnetic moment, as observed in our experiments.

The change of magnetization near T_c can be estimated as $\Delta M / M \propto QP^2 Y(d\lambda / dM)/M$ from a minimization of the free energy given by Eq.4.4. However, a quantitative estimation of this change is difficult due to lack of information of the temperature dependence of $\lambda_{001}(M)$. In this case, this result proves that the coupling is dominated by the elastic interactions between the two-phases.

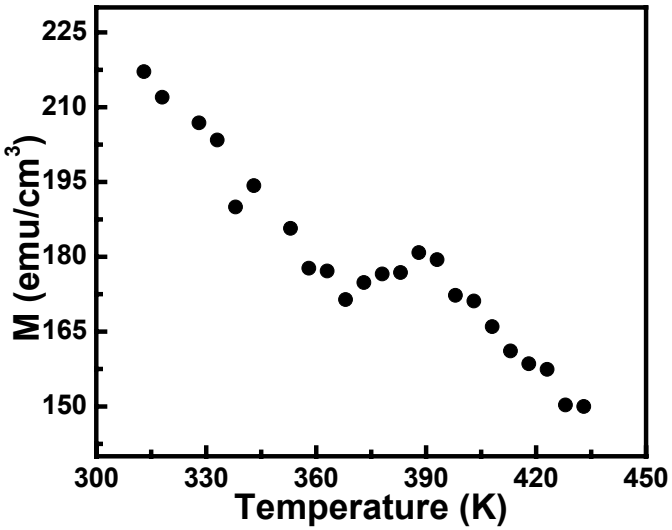

Fig.4.12 Magnetization vs temperature curve measured at H = 100 Oe, which shows a distinct drop of about 16 emu/cm^3 in magnetization at the ferroelectric Curie temperature. The sample was grown at 950 °C with a thickness of ~400 nm.

Direct measurements of the magnetoelectric coupling effect dE/dH were also conducted. Using a microwave microscope we measured the voltage changes under an ac magnetic field. A magnetoelectric coefficient of dE/dH 12 V/(cm·Oe) from a 400 nm films grown at 950 °C was obtained in our preliminary results[171]. This value is an order of magnitude lager than the values reported from the free-standing multilayer ceramics[35]. Careful experiments are in progress to confirm this result and the results will be published in future publications.

Chapter 5 $BaTiO_3$-$CoFe_2O_4$ multilayer structures

5.1 Introduction

As we discussed in Chapter one, $BaTiO_3$-$CoFe_2O_4$ composites can be created in a film-on-substrate geometry in two extreme forms. One is the vertical aligned nanostructures in which ferrimagnetic $CoFe_2O_4$ forms nanopillars embedded in the ferroelectric $BaTiO_3$ matrix (see Chapter 3), the other form is the "multilayer" geometry consisting of alternating layers of $BaTiO_3$ phase and $CoFe_2O_4$ phase. The ferroelectric-ferrimagnetic coupling effect in the nanostructure thin films is expected to be much higher than in the multilayer structure due to the clamping effect of the substrate in the multilayer structures[69]. Therefore, our effort in this work focused on the vertically aligned nanostructures. For comparison, $BaTiO_3$-$CoFe_2O_4$ multilayer structures were also deposited. In this chapter, we briefly discuss the microstructure and magnetic properties of $BaTiO_3$-$CoFe_2O_4$ multilayer thin films and compare them to the properties of the nanostructure arrays presented in Chapter 4.

The multilayer structures discussed in this chapter are different from the "free standing thick-film mutilayers" which have been used as an alternative to the sintered composites in bulk ceramics. Such "free standing thick-film multilayers" are laminates of alternating ferroelectric phase and ferro/ferrimagentic phase, i.e., Lead-zirconate titanate (PZT)/ (Terfenol-D) Tb-Dy-Fe alloy [36,37,52] or $Pb(Mg_{1/3}Nb_{2/3})O_3$-$PbTiO_3$ (PMN-PT)/Terfenol-D[38] prepared by stacking and bonding with silver epoxy, PZT/$La_{0.7}Sr_{0.3}MnO_3$ synthesized by tape casting[40], laminated composites of PZT/polyvinylidene-fluoride (PVDF) and Terfenol-D/PVDF prepared by a hot-molding technique[39], etc. The thickness of each layer in the bulk multilayers is in a

scale ranging from hundreds of micrometers to a few millimeters. These multilayer structures can eliminate leakage current through low resistivity ferrites, porosity, and any impurity or undesired phases at the interfaces. Therefore, it has been reported that such "free standing thick-film mutilayers" can enhance the piezoelectricity and the magnetoelectric effect[37,40, 173] . The magnetoelectric thin-film multilayer heterostructures studied in this work have thickness in the nanometer levels. Alternate piezoelectric $BaTiO_3$ and piezomagnetic $CoFe_2O_4$ layers were grown epitaxially on a (001) $SrTiO_3$ substrate. The microstructure of the multilayers was characterized using XRD and TEM. The magnetic properties were measured using SQUID and VSM. The coupling effect of the two order parameters in the multilayer structures was investigated from measurements of magnetization as a function of temperature.

5.2 $BaTiO_3$-$CoFe_2O_4$ multilayer structures

$BaTiO_3$-$CoFe_2O_4$ multilayer structures were synthesized using pulsed laser deposition. Two ceramic targets of $BaTiO_3$ and $CoFe_2O_4$ were used for the deposition. Nine layers of alternating $BaTiO_3$ and $CoFe_2O_4$ thin films with the first layer being $BaTiO_3$ were deposited on (001) $SrTiO_3$ substrates. $BaTiO_3$ layer is the first layer grown on the $SrTiO_3$ substrate due to its smaller lattice mismatch with the substrate to ensure epitaxial growth. Therefore, the $CoFe_2O_4$ layers were sandwiched between $BaTiO_3$ layers. During film growth, a substrate temperature of 700 °C and a dynamic O_2 partial pressure of 100 mTorr were maintained. Laser energy densities of ~1.0 J/cm^2 for $BaTiO_3$ growth and ~1.5 J/cm^2 for $CoFe_2O_4$ growth were used.

Fig.5.1A is a cross section TEM image taken from a sample with 4½ periods of alternating $BaTiO_3$ and $CoFe_2O_4$. The figure shows that the thickness of the

$BaTiO_3$ layers is ~25 nm and the thickness of $CoFe_2O_4$ is ~15 nm. The film shows epitaxial growth features. The selected area diffraction pattern (Fig.5.1B) shows two sets of spots, which were indexed to the spots in the (100) $BaTiO_3$ and (100) $CoFe_2O_4$ planes. The high resolution TEM image (Fig.5.1C) from one of the periods in Fig.5.3A presents fairly sharp interfaces between the $BaTiO_3$ and $CoFe_2O_4$ layers.

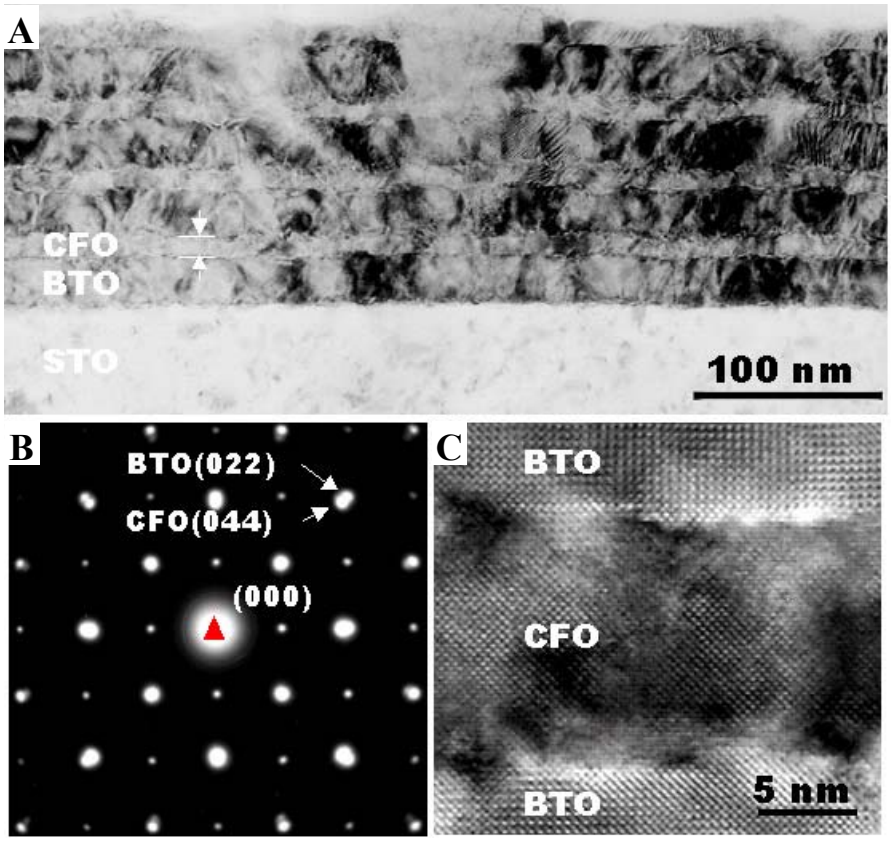

Fig.5.1 A. Cross section TEM image taken from the sample with 4½ periods of ~25 nm $BaTiO_3$ (BTO) and ~15 nm $CoFe_2O_4$ (CFO). The top $BaTiO_3$ layer was ion milled away during TEM sample preparation B. Selected area electron diffraction pattern showing the epitaxial relationship between the layers; C. High resolution TEM image showing the interfaces between two BTO and one CFO layer.

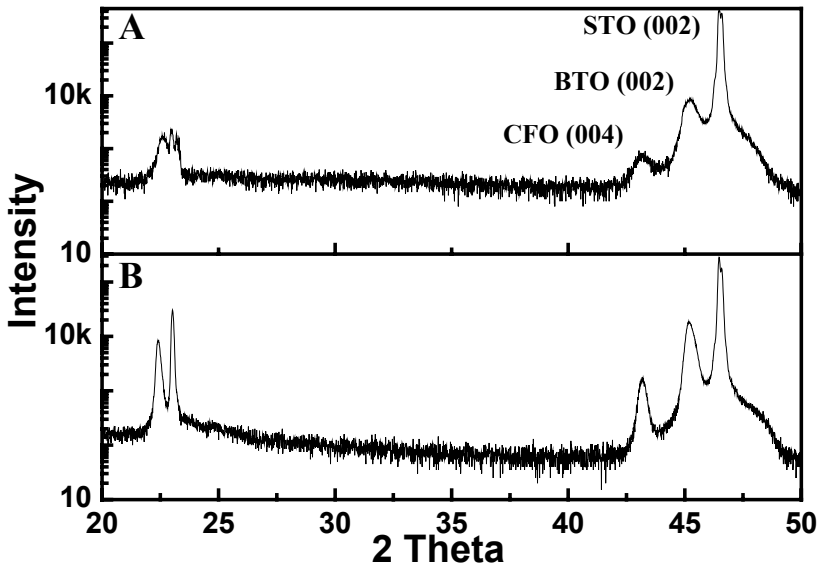

Fig.5.2 X-ray θ-2θ diffraction spectra taken from samples with 4½ periods of A. ~25 nm $BaTiO_3$ (BTO) and ~15 nm $CoFe_2O_4$ (CFO); and B. ~55 nm BTO and ~30 nm CFO.

Several $BaTiO_3$-$CoFe_2O_4$ multilayer structures with different thickness were synthesized for comparison. Fig.5.2 shows X-ray θ-2θ diffraction spectra taken from samples with 4½ periods of $BaTiO_3$ and $CoFe_2O_4$ with thickness of 25 nm and 15 nm respectively (A), and 55 nm of $BaTiO_3$ and 30 nm of $CoFe_2O_4$ (B). Both films show only (00*l*) oriented $BaTiO_3$ and $CoFe_2O_4$ peaks. Further TEM studies confirm that the films are epitaxial. As the thickness of the layers increases the intensity and sharpness of the diffraction peaks increase. Slight difference in the residual strains in the two multilayer films was obtained from the XRD spectra. A tensile strain of ~0.09 % in the $CoFe_2O_4$ phase perpendicular to the film plane was calculated in film A; while film B is fully relaxed with negligible out of plane strain. The strains relax by the formation of misfit dislocations, which were confirmed in high resolution TEM

studies. The thin film multilayers show stable microstructures. No interdiffusion was observed at the interface even after the sample was annealed at 950 °C for 10 hours.

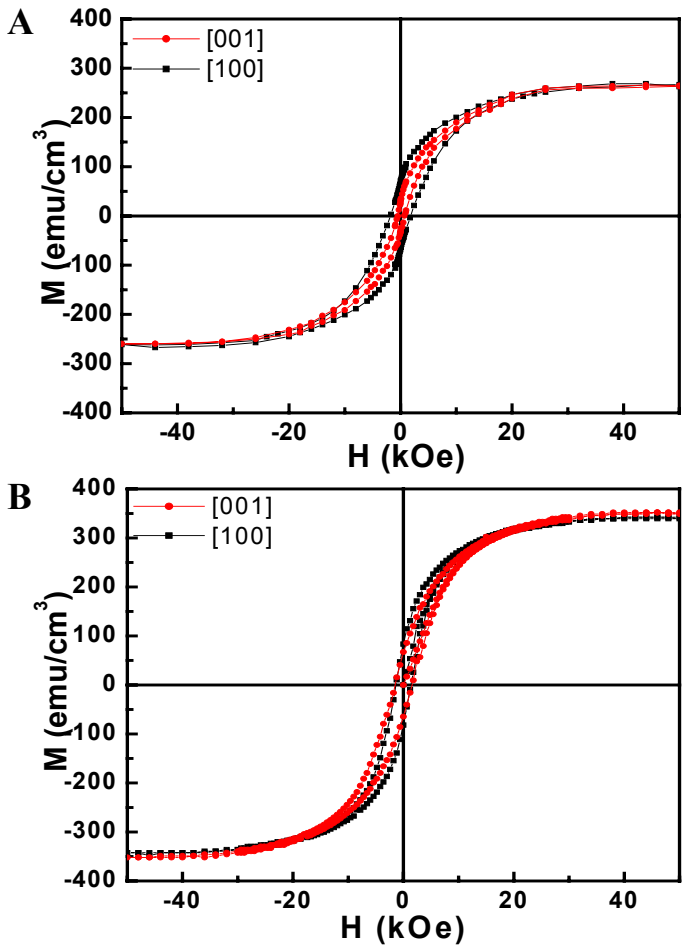

Fig.5.3 Magnetization (M) vs field (H) hysteresis loops of 4½ period multilayer thin films: A. ~25 nm of $BaTiO_3$ and ~15 nm of $CoFe_2O_4$; B. ~55 nm of $BaTiO_3$ and ~30 nm of $CoFe_2O_4$.

The magnetic properties of the multilayer thin films were measured by SQUID magnetometer. Fig.5.3A and B show the magnetization (M) vs field (H) hysteresis loops from film A and film B, respectively. Coercive field of ~1717 Oe for film A and ~1600 Oe for film B are observed. The two films show different saturation

magnetization values of M_s: ~270 emu/cm^3 for film A and ~350 emu/cm^3 for film B. These values were normalized to the volume fraction of $CoFe_2O_4$ phase in each multilayer structure. The suppression of the saturation magnetization (M_s) in film A is probably due to the higher interface to volume ratio involved in this film. The strain induced by lattice mismatch and difference in thermal expansion coefficients can also give rise to spin disordered regions at the interface, thus resulting in a reduced M_s[174]. Both multilayer films have low remnant magnetizations, ~70 Oe for film A (~26% of M_s) and ~83 Oe for film B (~24% of M_s). It has been reported that low magnetic remanence is due to the absence of large strains in the film[175].

Both films show a slight preferred direction of magnetization or an easier axis of magnetization in plane along the [100] direction as can be see in Fig.5.3. The anisotropy field is larger in the multilayer film with thinner $CoFe_2O_4$ layers. We believe that magnetic anisotropy in both films is dominated by shape anisotropy. The slightly larger anisotropy field in film A than film B is attributed to the tensile residual strain measured from film A while film B is essentially relaxed. Considering the fact that $CoFe_2O_4$ has a large negative magnetostriction, the out of plane tensile strain induces an easy axis in plane. The slight difference in residual strain in film A compared to film B also give rise to a slightly larger coercive field as observed in Fig.5.3.

The ferroelectric behavior of the multilayer films was demonstrated by a measurement of a high dielectric constant (ε). The dielectric constant measurements were conducted using microwave microscopy[176]. A value of ε ~220 was obtained from the multilayered film. The high value of the dielectric constant is a good indicator of ferroelectricity[177]. Direct measurement of P vs E ferroelectric hysteresis is

absent in the multilayer films because $CoFe_2O_4$ is insulating. Polarization from the $BaTiO_3$ layers is insulated in the $CoFe_2O_4$ sandwiched multilayer films.

5.3 Magnetoelectric coupling in $BaTiO_3$-$CoFe_2O_4$ multilayer structures

The temperature dependence of the magnetization was measured for the multilayer thin films with 55 nm of $BaTiO_3$ and 30 nm of $CoFe_2O_4$ (film B). Fig.5.4 shows the temperature dependent magnetization that was obtained from film B (black curve). The result is compared with that from $BaTiO_3$-$CoFe_2O_4$ nanostructures, in which $CoFe_2O_4$ pillars have the lateral dimension of 20-30 nm in a $BaTiO_3$ matrix (red curve). The magnetization vs temperature curve in the multilayer structure (black curve) shows almost a straight line, which considerably different from the temperature dependent magnetization curve from the $BaTiO_3$-$CoFe_2O_4$ nanostructures (red curve). This result indicates that the coupling effect in the $BaTiO_3$-$CoFe_2O_4$ multilayer structures is negligible. The negligible coupling effect in the multilayer structures is attributed to the clamping effect from the $SrTiO_3$ substrate[69]. As the temperature decreases from a temperature above the Curie temperature (T_c) of $BaTiO_3$ to a temperature below T_c, the stress due to the paraelectric/ferroelectric (cubic/tetragonal) transformation in the $BaTiO_3$ is almost fully clamped by the substrate. Therefore, no induced stress was expected in the $CoFe_2O_4$ due to the Curie transformation of the $BaTiO_3$ phase.

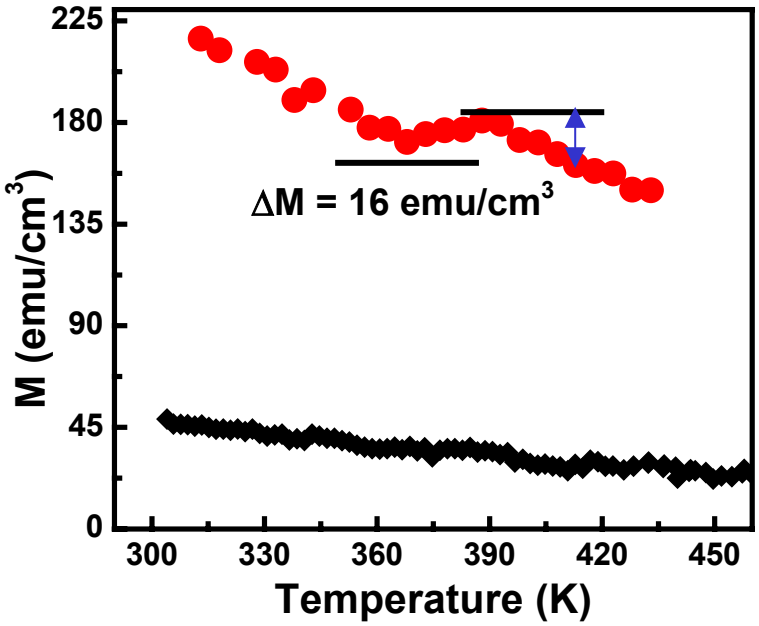

Fig.5.4 Magnetization vs temperature curves measured at H = 100 Oe, which show a distinct drop in magnetization at the ferroelectric Curie temperature (~390 K) for the self-assembled vertically aligned nanostructure (red curve) and negligible change in magnetization for the multilayered structure (black curve).

Chapter 6 Multiferroic $BiFeO_3$-$CoFe_2O_4$ nanostructures

6.1 Introduction

The self-assembled $BaTiO_3$-$CoFe_2O_4$ that was discussed in the previous chapters provides a model system for the growth of ferroelectric/ferromagnetic two-phase complex oxide nanostructures. We found similar self-assembly phenomenon in other spinel/peroskite oxides, i.e., $BaTiO_3$-$NiFe_2O_4$[70], $PbTiO_3$-$CoFe_2O_4$[71], $BiFeO_3$-$CoFe_2O_4$[178], etc. In this chapter, we present the growth and properties of self-assembled $BiFeO_3$-$CoFe_2O_4$ nanostructures.

Bulk $BiFeO_3$ is both ferroelectric and antiferromagnetic, exhibiting weak magnetism at room temperature due to a residual moment from a canted spin structure[12]. Pure $BiFeO_3$ itself is a material that has recently attracted considerable interest[179,180,181,182]. It is known that bulk $BiFeO_3$ is ferroelectric[183] with a Curie temperature (T_c) of about 1100 K. The structure of the ferroelectric phase, resolved experimentally using both X-ray and neutron diffraction on powder samples[184,185], can be understood as a highly distorted perovskite with the rhombohedral symmetry and with a space group of *R3c*. The primitive unit cell (10 atoms) contains 2 formula units as shown in Fig.6.1. The *R3c* symmetry permits the development of a spontaneous polarization along the [111] direction, in which Bi, Fe, and O are displaced relative to one another along this 3-fold axis. The largest relative displacements are those between Bi and O, consistent with a stereochemically active Bi lone pair. The polar displacements (relative to cubic perovskite) are extremely large compared with those in non-lone-pair-active perovskite ferroelectrics such as $BaTiO_3$ or $KNbO_3$, but are consistent with those observed in other Bi-based perovskites. Surprisingly, given the

large atomic displacements relative to the centrosymmetric cubic perovskite structure and the high ferroelectric Curie temperature, early measurements on bulk single-crystals yielded rather small polarizations. For example, Teague *et al.*[183] initially reported a polarization along [111] of 6.1 μC/cm^2. This small value is in sharp contrast with the recent experiments on epitaxial thin film samples of $BiFeO_3$, which were found to possess large polarizations. The first thin film measurements[179] yielded values of 50-90 μC/cm^2 on (100) oriented substrates, increasing to 100 μC/cm^2 for (111) orientations[180]. Both structural examinations and first principle calculations[186] have been conducted to seek plausible explanations for the large ferroelectric polarizations obtained experimentally.

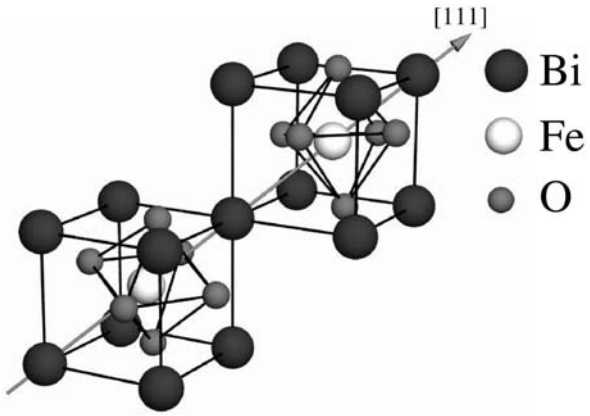

Fig.6.1 Schematic *R3c* $BiFeO_3$ structure[186]. Notice the position of the oxygen octahedra relative to the Bi framework; in the ideal cubic perovskite structure the oxygen ions would occupy the face-centered sites.

The magnetic behavior of $BiFeO_3$ is another intriguing issue that has been of intense research interest. Bulk $BiFeO_3$ has long been known as antiferromagnetic [187,183] with a Néel temperature of T_N ~ 643K. The magnetic moments of Fe are coupled ferromagnetically within the pseudocubic (111) planes

and antiferromagnetically between adjacent planes. If the magnetic moments are oriented perpendicular to the [111] direction, the symmetry also permits a canting of the antiferromagnetic sublattices resulting in a macroscopic magnetization; so called weak ferromagnetism[188,189]. Significant magnetization has been reported recently in high quality epitaxial $BiFeO_3$ thin films[179]. However, its origin is still not understood.

The selection for $BiFeO_3$ as the ferroelectric phase in the present multiferroic $BiFeO_3$-$CoFe_2O_4$ is driven by the large values of polarization and piezoelectricity reported in $BiFeO_3$[179]. Considering that $BiFeO_3$ is ferroelectric and antiferromagnetic, the possible coupling effects of ferrimagnetism/antiferromagnetism and ferrimagnetism/ferroelectricity between the two phases make $CoFe_2O_4$-$BiFeO_3$ an interesting system. In this chapter, the structure of nanostructured $BiFeO_3$-$CoFe_2O_4$ thin films, as well as their ferroelectric and magnetic properties are presented.

6.2 Self-assembled $BiFeO_3$-$CoFe_2O_4$ nanostructures

$BiFeO_3$-$CoFe_2O_4$ thin films were deposited on single crystal $SrTiO_3$ (001) substrates using pulsed laser deposition (KrF 248 nm laser). A thin layer of $SrRuO_3$ was deposited as bottom electrode for ferroelectric measurements. A single Bi-Co-Fe-Oxide ceramic target was used during deposition. A dynamic oxygen atmosphere pressure of 100 mTorr was maintained during deposition. The substrate temperature was varied in the range of 550~700 ºC. Films were deposited with a thickness of about 250 nm. The structure of the films were characterized using X-ray diffraction by CuK_α radiation in a Siemens D5000 four-circle diffractometer and transmission electron microscopy (TEM) using a JEOL 4000FX TEM operating at 300 kV.

The X-ray diffraction and TEM studies from the $BiFeO_3$-$CoFe_2O_4$ thin films indicate that two phases $BiFeO_3$ and $CoFe_2O_4$ spontaneously separated during growth.

The films are epitaxial with a relationship of (100) $SrTiO_3$ // (100) $SrRuO_3$ // (100) $BiFeO_3$ // (100) $CoFe_2O_4$ and [100] $SrTiO_3$ // [100] $SrRuO_3$ // [100] $BiFeO_3$ // [100] $CoFe_2O_4$. The results from the plan-view and cross-section TEM studies indicate that $CoFe_2O_4$ forms nanopillar arrays embedded in a $BiFeO_3$ matrix. Fig.6.2A is a plan-view TEM image taken from a $BiFeO_3$-$CoFe_2O_4$ (1:1) film grown at 700 °C with a thickness about 250 nm. $CoFe_2O_4$ pillars are in square shape with dimensions of ~150×150 nm. The selected area diffraction pattern from this sample, shown in Fig.6.2B, exhibits only two sets of spots that were indexed to be $CoFe_2O_4$ (001) and $BiFeO_3$ (001) patterns. This result confirms the epitaxial relationship of the two phases in the film. All the $CoFe_2O_4$ pillars are single crystalline with sharp interfaces with the $BiFeO_3$ matrix, see Fig.6.2C. The interfaces are {110} type of planes as shown in the high resolution image in Fig.6.2D. As the growth temperature decreases, the lateral size of the pillars also decreases. At a deposition temperature of 550 ºC, for example, the $CoFe_2O_4$ pillars have dimensions of ~10x10 nm. The epitaxial relationship remains the same as for the films grown at high temperatures as can be seen in the selected area diffraction pattern from this film (not shown). Similar to the $BaTiO_3$-$CoFe_2O_4$ nanostructures, the growth of the $CoFe_2O_4$ nanopillars in the $BiFeO_3$ matrix is kinetically diffusion controlled.

In both $BaTiO_3$-$CoFe_2O_4$ and $BiFeO_3$-$CoFe_2O_4$ systems the nanostructure array consists of spinel $CoFe_2O_4$ vertical nanopillars in a perovskite matrix. In order to understand why $CoFe_2O_4$ instead of $BiFeO_3$ or $BaTiO_3$ form pillars we conducted systematic studies. We believe that lattice mismatch strain, the elastic moduli of the two phases, the interface energy and molar ratio of the two phases play important roles in the growth dynamics leading to the nanoscale pattern formation. In order to achieve a desired pattern of matrix and pillars in a certain system, it is necessary to

find the favorable molar ratio of the two phases, suitable substrates that would lead to the desired structure and optimum growth parameters. In the $BaTiO_3$-$CoFe_2O_4$ system, we deposited the films on various substrates. The results show that there was no significant change of nanostructures at certain range of lattice mismatch strain (see section 3.5). For the $BiFeO_3$-$CoFe_2O_4$ system, we also changed the molar ratio of the two phases by using different composition targets in addition to selecting different substrates. Two more composition targets with the $BiFeO_3$:$CoFe_2O_4$ molar ratio of 65:35 and $\frac{1}{3}:\frac{2}{3}$ were used in addition to the 1:1 target.

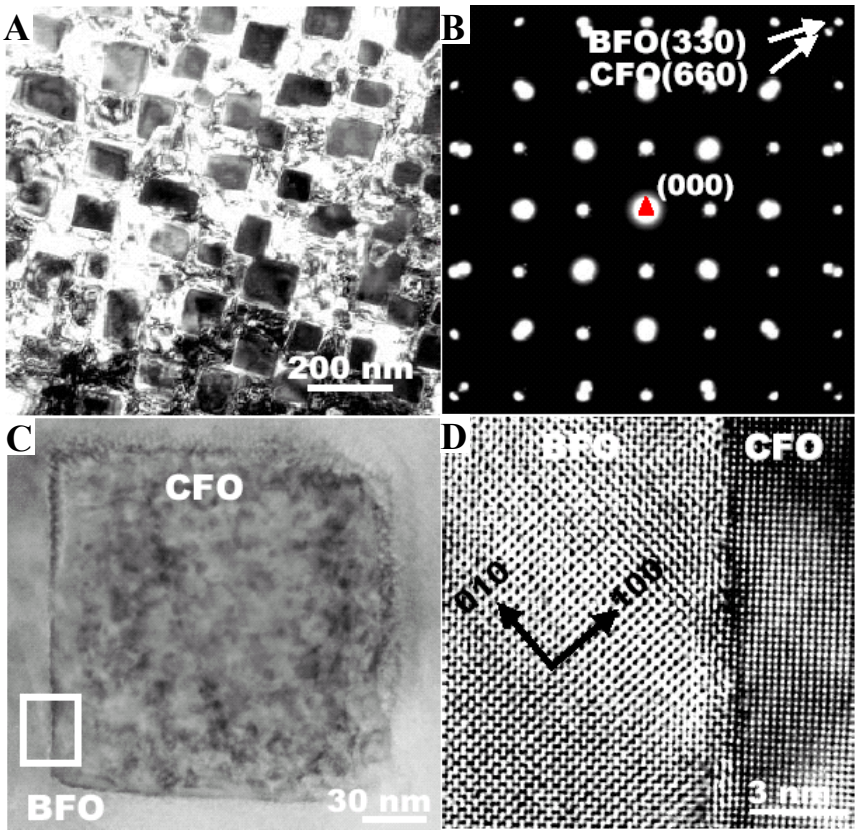

Fig.6.2 Plan-view TEM images taken from a $BiFeO_3$-$CoFe_2O_4$ (1:1 molar ratio) film grown at 700 °C with a thickness of about 250 nm. A. Bright field image; B. selected area diffraction pattern taken from A; C. high resolution image of one single $BiFeO_3$ pillar; D. magnified segment of the interface between the $CoFe_2O_4$ pillar and the $BiFeO_3$ matrix from C.

Detail studies of the microstructure in the $BiFeO_3$-$CoFe_2O_4$ system were concentrated on the films deposited using the ⅓ $BiFeO_3$: ⅔ $CoFe_2O_4$ target. Different substrates, $SrTiO_3$ (001), MgO (001) and $SrTiO_3$ (001) with two buffer layers of epitaxial $BaTiO_3$/$CoFe_2O_4$, were used. We did plan-view TEM studies on the films with a composition of $BiFeO_3$:$CoFe_2O_4$ = ⅓ : ⅔ grown on $SrTiO_3$ (001). Only two phases of $BiFeO_3$ and $CoFe_2O_4$ were identified in the diffraction pattern (Fig.6.3A). A dark field image taken with g = [100] of $BiFeO_3$ is shown in Fig.6.3B. It is interesting to note that $CoFe_2O_4$ (black regions) forms pillars with lateral square shape in a $BiFeO_3$ matrix. The size of the $CoFe_2O_4$ pillars is not as regular as in the 1:1 composition film probably due to the larger volume fraction of the $CoFe_2O_4$ phase. Similar morphology was observed in films grown on MgO (001) substrates and on $SrTiO_3$ (001) with a buffer layer of $BaTiO_3$/$CoFe_2O_4$.

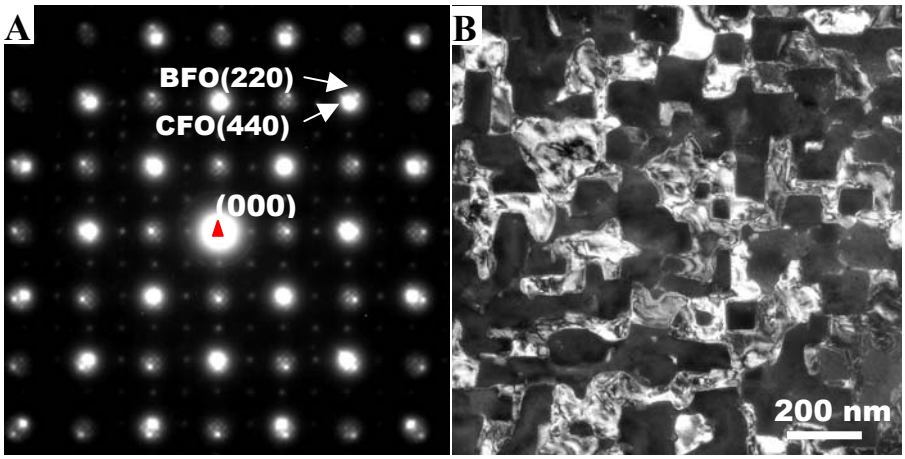

Fig.6.3 A. (001) selected area diffraction pattern taken from a plan view TEM sample from a film with the composition of ⅓ $BiFeO_3$: ⅔ $CoFe_2O_4$, showing the epitaxial relationship between $BiFeO_3$ and $CoFe_2O_4$. Notice that there are extra spots at half position of $BiFeO_3$ spots (weak set of spots) which are believed to be due to oxygen vacancy induced ordering in $BiFeO_3$; B. dark field image taken with g = [100] of $BiFeO_3$.

We propose two possible reasons for the formation of $CoFe_2O_4$ nanopillars instead of $BiFeO_3$ nanopillars in the $BiFeO_3$-$CoFe_2O_4$ system. One is the difference in Young's modulus of the two component phases. It has been reported that in semiconductor two-phase systems the softer phase prefers to wrap around the harder phase[190]. Unfortunately, the value of Young's modulus is not known for $BiFeO_3$. Therefore, this prediction needs to be proven in other systems. Another possible reason is $CoFe_2O_4$ has a larger lattice than $BiFeO_3$. During the growth of an epitaxial thin film, surface segregation prefers to nucleate at the surface undulation peaks due to the stress relaxation at the peaks[191]. We believe that $CoFe_2O_4$ forms pillars during the heteroepitaxial growth of $BiFeO_3$-$CoFe_2O_4$ because the stress is partially relaxed in such a film.

6.3 Magnetic properties of $BiFeO_3$-$CoFe_2O_4$ nanostructures

A Superconducting Quantum Interference Device (SQUID) was used to measure the magnetic properties of the films. Magnetic force microscopy (MFM) was conducted to study the magnetic domain structures in the films. A commercial Atomic Force Microscope (AFM) with a magnetic tip was used in MFM mode. The tip was magnetized with the magnetic poling field perpendicular to the cantilever. With this configuration, both topography and magnetic features were obtained simultaneously.

Magnetization (M) vs field (H) hysteresis loops from a $BiFeO_3$-$CoFe_2O_4$ film grown at 700 °C are shown in Fig.6.4. A saturation magnetization (M_s) of ~320 emu/cm^3 normalized to the volume fraction of $CoFe_2O_4$ (55%) was obtained. The remnant magnetization along the growth direction is about 60% of M_s. The curve

shows an anisotropy field of 10 kOe between the out-of-plane and in-plane magnetization, with an easy axis out-of-plane (along the film growth direction).

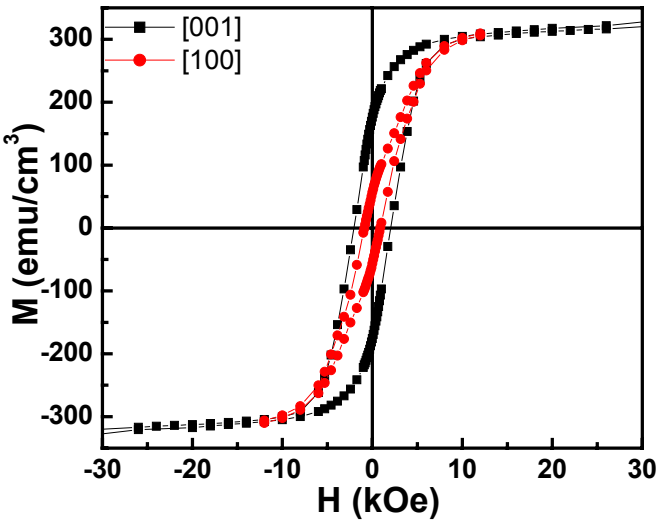

Fig.6.4 Out-of-plane and in-plane M vs H hysteresis loops of the $BiFeO_3$-$CoFe_2O_4$ (1:1) nanostructured thin film deposited at a temperature of 700 °C.

Factors that contribute to the magnetic anisotropy of the films are considered here. Firstly, the shape anisotropy was calculated. It is observed from cross section TEM image that $CoFe_2O_4$ nanopillars have an aspect ratio (*c/a*) of ~2.5. The demagnetization factor for a cylinder with aspect ratio of 2.5 is taken to be $N_z = 0.133$. The associated anisotropy energy is: $E_{shape} = 2\pi(N_x - N_z)M_s^2$, where $Nx = (1-Nz)/2$. For M_s of 320 emu/ cm^3, the shape anisotropy field was calculated to be: $H_{shape} = 2E_{shape}/M_s \sim 1208$ Oe. Secondly, since the $CoFe_2O_4$ pillars have a larger lateral size in the $BiFeO_3$ matrix compared with the $BaTiO_3$ matrix, the compressive lattice mismatch with the $BiFeO_3$ matrix is almost fully relaxed. A residual compressive strain of only about 0.1% along the pillars was obtained from XRD study (compared to ~0.8% strain in the case of $BaTiO_3$-$CoFe_2O_4$). Therefore, the calculated stress

anisotropy[54] is only about 4250 Oe. Since no magnetocrystalline anisotropy is expected between [001] and [100] directions for cubic $CoFe_2O_4$, the total anisotropy from shape, stress and magnetocrystalline anisotropy is ~5458 Oe, which is much smaller than the experimentally observed value (10,000 Oe). We believe that other sources of the anisotropy field, such as surface spin states induced by exchange coupling between ferromagnetic $CoFe_2O_4$ and antiferromagnetic $BiFeO_3$ should play a key role in this system. More work is needed to interpret the spin coupling between the two phases.

Images of the magnetic domains in the $BiFeO_3$-$CoFe_2O_4$ films at their remnant state were obtained using MFM. The samples were poled in the out-of-plane direction in a field of 7 kOe along the $[00\bar{1}]$ and [001] directions, respectively, before imaging. Fig.6.5A is the topography image showing $CoFe_2O_4$ pillars extending over the $BiFeO_3$ matrix by about 100-120 nm, which is consistent with our TEM observations. Fig.6.5B is the MFM image corresponding to Fig.6.5A with magnetic poling along $[00\bar{1}]$. Almost all the $CoFe_2O_4$ domains are poled in one direction as can be seen from the image contrast. The magnetic $CoFe_2O_4$ domains are switched to the other direction by applying a magnetic field in the opposite direction ([001]). Fig.6.5C and D are the topography image and the corresponding MFM images obtained under the reversed field. The individual pillars are clearly identified in the MFM images, which suggest that the dipolar interactions between neighboring pillars are weak. The fairly high anisotropy of the pillars (normally at the expense of magnetic dipole intensity) and large distance between the pillars (~150 nm) may contribute to the weak dipolar interaction between the pillars[192]. At low growth temperatures the pillars get close to each other, and neighboring pillars interact with each other. Large areas of black or white contrast are observed in MFM images (at the remnant state) from films with

pillars having a separation of about 10 nm. The magnetization can be viewed as a collective phenomenon resulting from the alignment of the localized spins within a correlation area of the films.

Therefore, both magnetic hysteresis loops and MFM images resolve the magnetization of the film as a consequence of the $CoFe_2O_4$ pillars. Experiments are currently being carried out to investigate if there is a ferrimagnetic/antiferromagnetic coupling effect of the $BiFeO_3$-$CoFe_2O_4$ nanostructures. The results of this study will be reported in a future publication.

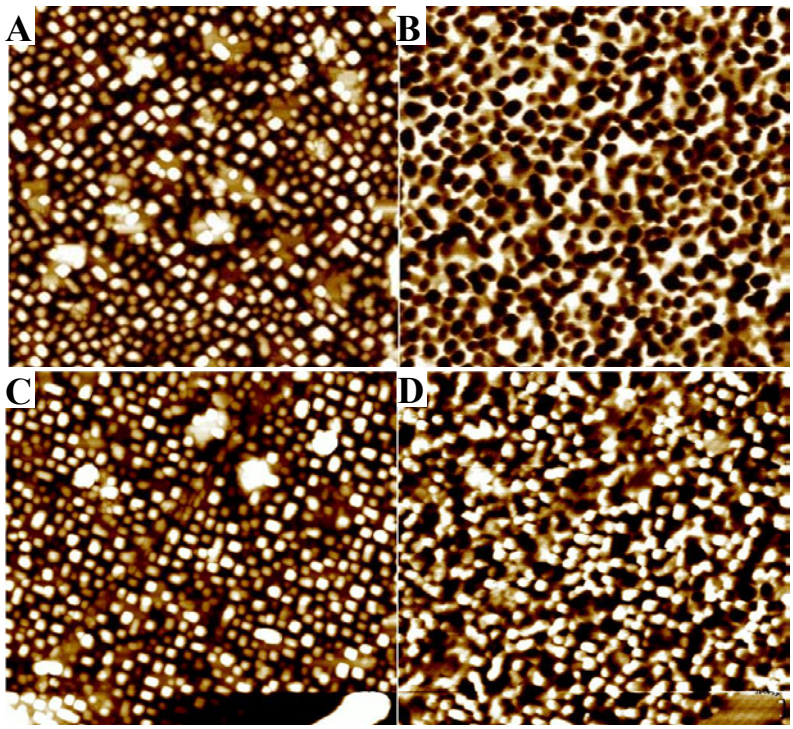

Fig.6.5 Topography and MFM images of the $BiFeO_3$-$CoFe_2O_4$ (1:1) film grown at 700 °C. The images correspond to 5 × 5 μm^2areas. A and B are, respectively, the topography image and the corresponding MFM image after the film was poled in a field of 7 kOe along the $[00\bar{1}]$ direction; C and D are, respectively, the topography image and the corresponding MFM image after the film was poled in a field of 7 kOe along the [001] direction.

6.4 Ferroelectric properties of $BiFeO_3$-$CoFe_2O_4$ nanostructures

Ferroelectric measurements were performed using a commercially available RT6000 test system (Radiant Technologies, USA). Piezoresponse images and d_{33} constant of the films were obtained using an AFM set up[77].

Fig.6.6 A and B are the topography image and piezoresponse image, respectively, taken from a $BiFeO_3$:$CoFe_2O_4$ (1:1) film grown at 700 ºC with a thickness of 250 nm. In the topography image (Fig.6.6A), $CoFe_2O_4$ have square pillars extending above the $BiFeO_3$ matrix. The piezoresponse image was taken with an AC bias of 6 V and a frequency of 6.39 kHz. It is difficulty for the AFM tip to touch the $BiFeO_3$ matrix surface when the extending $CoFe_2O_4$ pillars are close to each other. Thus, the ferroelectric domains in the $BiFeO_3$ matrix where the $CoFe_2O_4$ pillars are closely packed are not identified. In contrast, $BiFeO_3$ ferroelectric domain patterns are clearly visible where the $CoFe_2O_4$ pillars are well separated. The ferroelectric domains were switched when a DC electric field was applied.

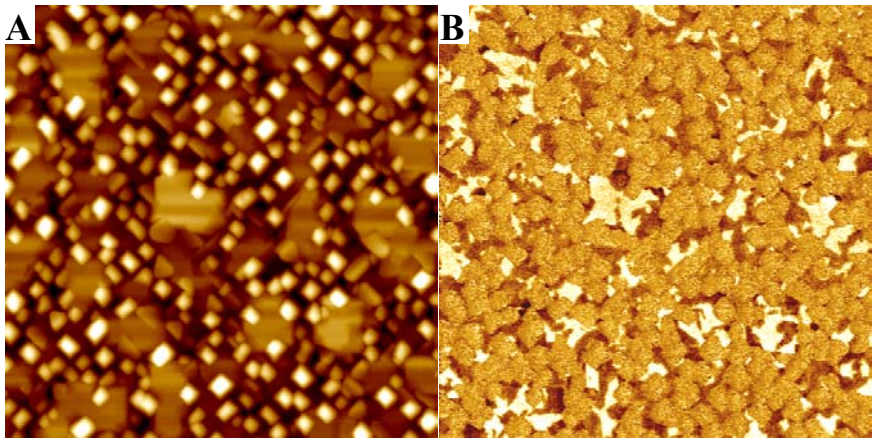

Fig.6.6 Topography and piezoresponse images taken from a $BiFeO_3$-$CoFe_2O_4$ (1:1) film grown at 700 °C with a thickness of 250 nm. The images correspond to 4 × 4 μm^2 areas. A. topography image; B. piezoresponse image taken with an AC bias of 6 V and a frequency of 6.39 kHz.

Quantitative d_{33} measurements of the switching of the polarization in $BiFeO_3$ were conducted. Fig.6.7 is a piezoelectric d_{33} hysteresis loop using a 32 μm diameter capacitor from the film. The hysteresis is well defined in the "up-part" loop with a maximum d_{33} value of about 16 pm/V under an applied field of 8 V. However, the other part of the loop lost the symmetry features. The asymmetry of the hysteresis loop is probably due to the asymmetric electrodes of the measured capacitor. For the present $BiFeO_3$-$CoFe_2O_4$ thin film capacitors, we use $SrRuO_3$ as bottom electrode and Platinum as top electrode. Top electrode with Platinum/$SrRuO_3$ was also tried. However, no considerable improvement of the hysteresis was obtained.

Ferroelectric hysteresis measurements were also conducted. However, no well-defined ferroelectric hysteresis loop was obtained due to both the leakage current (the resistivity is less than $10^{5\sim6}$ Ωcm) and diode effect. Future work to increase the resistivity and eliminate diode effect in the $BiFeO_3$-$CoFe_2O_4$ thin films is needed.

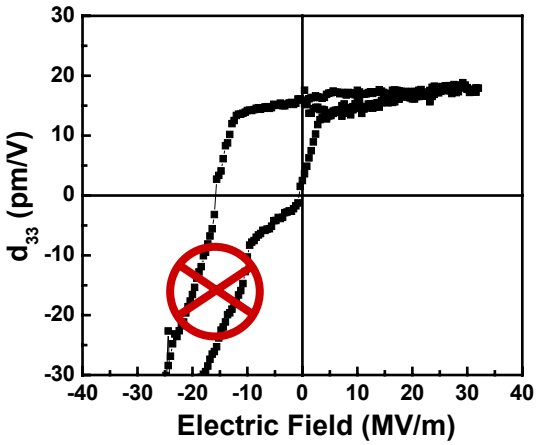

Fig.6.7 Small signal piezoelectric d_{33} hysteresis loop for a 32 μm diameter capacitor from a $BiFeO_3$-$CoFe_2O_4$ film grown at 700 °C with a thickness of 250 nm.

6.5 Magnetoelectric coupling of $BiFeO_3$-$CoFe_2O_4$ nanostructures

We conducted studies on the coupling of the ferroelectric and ferromagnetic order parameters in the $BiFeO_3$-$CoFe_2O_4$ nanostructures. As it was discussed in the $BaTiO_3$-$CoFe_2O_4$ nanostructures, the coupling in a two-phase magnetoelectric nanostructure system requires a strong elastic interaction between the two phases. In order to estimate the elastic energy that is needed to switch to magnetization of $CoFe_2O_4$ pillars, we calculated the elastic energy (E_{el}) associated with the ferroelectric switching of the $BiFeO_3$ matrix, the magnetoelastic energy (E_{mel}) in the $CoFe_2O_4$ pillars due to the stress from the matrix and the demagnetization energy (E_{Dmag}) in the $CoFe_2O_4$ pillars.

The elastic energy (E_{el}) of the $BiFeO_3$ matrix due to ferroelectric switching can be expressed as:

$$E_{el} = \frac{1}{2} Y \varepsilon_{001}^{\ 2} \qquad \text{Eq.6.1}$$

in which, $\varepsilon_{001} = \int d_{33} dE \approx 0.5 \times 10^{-3}$. The value of ε_{001} was estimated from Fig.6.7. We take $Y = 200$ GPa for $BiFeO_3$, for which the elastic energy is $E_{el} \approx 2.5 \times 10^4 J/m^3$.

The magnetoelastic energy (E_{mel}) associated with the stress from the $BiFeO_3$ matrix during growth can be expressed as:

$$E_{mel} = -\frac{3}{2} \lambda_{001} \sigma_{001} \qquad \text{Eq.6.2}$$

in which λ_{001} (taken to be $\lambda_{001} \sim -350 \times 10^{-6}$)[154] is the magnetostriction coefficient of $CoFe_2O_4$, σ_{001} is the stress along the $CoFe_2O_4$ pillars, $\sigma_{001} = Y\varepsilon_{001}$. From XRD results, we get $\varepsilon_{001} = -0.1\%$. The Young's modulus Y of $CoFe_2O_4$ is taken to 141.6 GPa[154]. We estimate $E_{mel} \approx -7.4 \times 10^4 J/m^3$.

The demagnetization energy associate with the shape ($c/a = 2.5$) of the $CoFe_2O_4$ pillar is expressed as:

$$E_{Dmag} = -2\pi(N_x - N_z)M_s^2 \qquad \text{Eq.6.3}$$

in which the demagnetization factor for a cylinder with an aspect ratio of 2.5 is N_z = 0.133 and $N_x = (1 - N_z)/2$ (see section 6.3). For M_s of 320 emu/ cm^3, we estimate $E_{Dmag} \approx -1.9 \times 10^5 ergs/cm^3 \approx -1.9 \times 10^4 J/m^3$.

According to the above estimated values, the elastic energy (E_{el}) associated with the ferroelectric switching of the $BiFeO_3$ matrix is of the same order of magnitude as the magnetoelastic energy (E_{mel}) plus the demagnetization energy (E_{Dmag}) in the $CoFe_2O_4$ pillars. Therefore, it is possible to switch the sign of the total energy E, $E = E_{el} + E_{mel} + E_{Dmag}$ associated with the $CoFe_2O_4$ by the piezoelectric deformation of the $BiFeO_3$ matrix.

Fig.6.8 A and B are MFM images of the $BiFeO_3$-$CoFe_2O_4$ nanostructures before and after an electric poling with –10V. Fig.6.8A is the MFM image when the sample was magnetized in the out-of-plane direction without electrical poling. All the $CoFe_2O_4$ pillars are in black showing that the magnetization of all the pillars is in the same direction. The MFM image after the sample was electrically poled with –10V is shown Fig.6.8B. It is clearly shown that a considerable fraction of $CoFe_2O_4$ pillars changed their magnetization direction due to the electric poling of the $BiFeO_3$, as shown in the marked areas for example. The magnetization of the pillars can be switched back when an electric field of +10 V is applied. Such changes of the magnetization in the $CoFe_2O_4$ pillars due to an applied electric field provide a direct evidence of the coupling between the two parameters.

In summary, $BiFeO_3$-$CoFe_2O_4$ nanostructures spontaneously formed during pulsed laser deposition. Nanostructured films show three dimensional heteroepitaxy. Both magnetic hysteresis loops and MFM images resolve the magnetizatoin of the film corresponding to the $CoFe_2O_4$ pillars. Both PFM imaging and quantitative d_{33} measurements resolved the ferroelectric properties corresponding to the $BiFeO_3$ matrix. The coupling between the two order parameters of ferroelectricity and ferrimagnetism is demonstrated by switching of the magnetization of a large fraction of $CoFe_2O_4$ pillars due to an applied electric field.

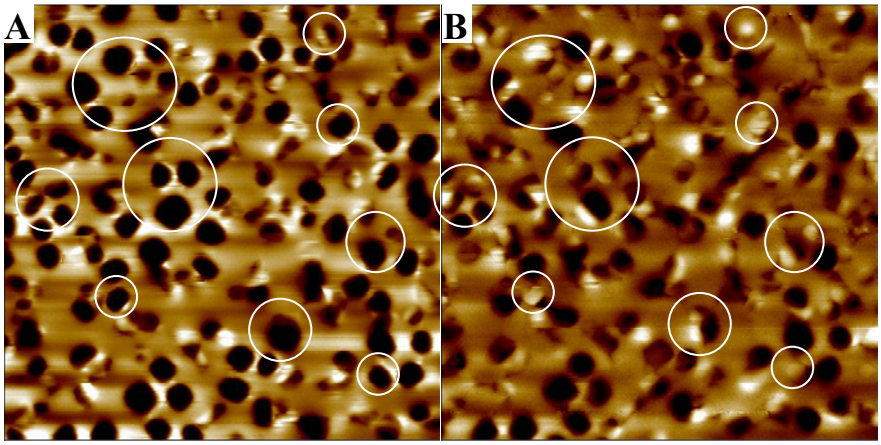

Fig.6.8 MFM images of the $BiFeO_3$-$CoFe_2O_4$ nanostructures before and after an electric poling with –10V. A. MFM image when the film was magnetized in one direction. B. MFM image after the sample was electrically poled with –10V. The images correspond to 4 × 4 μm^2 areas.

Chapter 7 Summary and Future Work

In this dissertation, we performed a systematic study of the formation of $BaTiO_3$-$CoFe_2O_4$ thin film nanostructures and careful characterization of their ferroelectric and magnetic properties, and the magnetoelectric coupling effect in this system. This is a new and exciting approach to creating self-assembled ferroelectric-ferrimagnetic $BaTiO_3$-$CoFe_2O_4$ nanostructures. $BaTiO_3$-$CoFe_2O_4$ is as a model system showing a strong coupling of the order parameters of magnetism and ferroelectricity through heteroepitaxy of the two lattices.

$BaTiO_3$-$CoFe_2O_4$ nanostructures with $CoFe_2O_4$ nano-pillar arrays embedded in a $BaTiO_3$ matrix exhibit three-dimensional heteroepitaxy. In order to understand the formation of the nanostructures, we deposited films under various conditions by systematically changing the growth temperature, growth rate, lattice mismatch strain (via the use of various substrates), the film thickness.. The size and aspect ratio of the $CoFe_2O_4$ pillars can be accurately controlled by the growth temperature and/or the growth rate. The lateral size of the $CoFe_2O_4$ pillars is proportional to the surface diffusion distance during growth.

We measured the ferroelectric and magnetic properties of the thin film nanostructures, which correspond to the $BaTiO_3$ and $CoFe_2O_4$ phases, respectively. $BaTiO_3$-$CoFe_2O_4$ nanostructures exhibit a large uniaxial magnetic anisotropy with an easy axis normal to the film plane. Our calculations of the anisotropy field show that the residual strain in the $CoFe_2O_4$ pillars is the main contribution to the anisotropy field. Both ferroelectric and piezoelectric hysteresis loops of the films demonstrate the ferroelectric properties corresponding to the $BaTiO_3$ phase in the $BaTiO_3$-$CoFe_2O_4$ nanostructures. The temperature dependent magnetic measurements in the $BaTiO_3$-

$CoFe_2O_4$ nanostructures illustrate a coupling between the two order parameters of polarization and magnetization, by a change in magnetization at the ferroelectric Curie temperature.

This approach to the formation of self-assembled ferroelectric and magnetic nanostructures is generic. We created similar nanostructures from other spinel-perovskite systems, such as $BiFeO_3$-$CoFe_2O_4$, $BaTiO_3$-$NiFe_2O_4$, etc.. Thus, this work opens scenarios both in the nanostructure formation of complex oxides and the characterization of multiferroic nanostructures with tunable magnetic and ferroelectric properties.

Further work can be carried out in two areas: the growth of the nanostructures and their properties. For the formation of $BaTiO_3$-$CoFe_2O_4$ nanostructures or other systems, there are several interesting questions to address:

1. How to form highly ordered $BaTiO_3$-$CoFe_2O_4$ nanostructures? Ordered nanostructures are tremendously valuable for device fabrications. However, it is still a challenge to grow well ordered complex oxides by self-assembly. The starting point could be the deposition of the films on patterned substrates.
2. How to form ferroelectric nanopillars in a magnetic matrix? According to the results in this work, ferromagnetic $CoFe_2O_4$, or $NiFe_2O_4$, prefer to form pillars in a ferroelectric $BaTiO_3$, or $BiFeO_3$ matrix in the systems studied ($BaTiO_3$-$CoFe_2O_4$, $BiFeO_3$-$CoFe_2O_4$ and $BaTiO_3$-$NiFe_2O_4$). Experiments on other systems should be conducted in an attempt to obtain ferroelectric nanopillars embedded in a ferromagnetic matrix. In order to select a suitable system various factors should be considered, such as solubility between the two components, elastic moduli, molar ratio and relative lattice unit size of the two

phases, lattice mismatch of the two phases with each other and with the substrate, etc..

3. What parameters determine the shape of the nanostructures? It is interesting that $CoFe_2O_4$ nanopillars have circular cross section in a $BaTiO_3$ matrix while they have square cross section in a $BiFeO_3$ matrix. It would be interesting to study the interfaces in order to understand and further control the shape, structure and properties of the nanostructures.
4. What is the mechanism for the formation of the nanostructure array? An advanced theoretical model needs to be developed in order to fully understand the evolution of the $BaTiO_3$-$CoFe_2O_4$ nanostructures with increasing film thickness.

For the characterization of the multiferroic nanostructures there are also other important issues:

1. Direct quantitative measurements of the magnetoelectric coupling effect in the $BaTiO_3$-$CoFe_2O_4$ or $BiFeO_3$-$CoFe_2O_4$ nanostructures, i.e., direct measurement of the change of magnetization under an applied electric field or measurement of the change of polarization under an applied magnetic field.
2. Measurements of other properties, i.e., optical properties, microwave properties, etc., on the $BaTiO_3$-$CoFe_2O_4$, $BiFeO_3$-$CoFe_2O_4$, or $BaTiO_3$-$NiFe_2O_4$ nanostructure systems.

REFERENCES

[1] P. Weiss, J. Phys. **6**, 661 (1907).

[2]E. C. Stoner, Philos. Mag. **15**, 1080 (**1933**).

[3] V. E. Wood and A. E. Austin, in *Magnetoelectric Interaction Phenomena in Crystals*, A. J. Freeman, H. Schmid, Eds. (Gordon and Breach: Newark, NJ, 1975).

[4] P. Curie, J. Phys. 3^{e} Ser., 393 (1894).

[5] S. A. Boguslavsky, Moscow, Fizmatgiz 231 (1961).

[6] D. N. Astrov, J. Exptl. Theor. Phys. (USSR) **38**, 984 (1960). [Sov. Phys. JETP **11**, 708 (1960)].

[7] V. J. Folen, G. T. Rado and E. W. Stalder, Phys. Rev. Lett. **6**, 607 (1961).

[8] G. T. Rado and V. J. Folen, Phys. Rev. Lett. **7**, 310 (1961).

[9] G. A. Smolensky, V. A. Isupov, N. N. Krainik and A. I. Agranovskaya, Izv. AN SSSR. Ser. Phys. **25**, 1333 (1991).

[10] S. A. Fedulov, Yu. N. Venevtsev, G. S. Zhdanov, E. G. Smazhevskaya, and I. S. Rez, Kristallografiya **7**, 77 (1962).

[11] S. V. Kiselev, R. P. Ozerov and G. S. Zhdanov, Dokl. AN SSSR **145**, 1255 (1962).

[12] G. A. Smolenskiĭ and I. E. Chupis, Sov. Phys. Usp. **25**, 475 (1982).

[13] Y. N. Venevtsev, V. V. Gagulin, and I. D. Zhitomirsky, Ferroelectrics **73**, 221 (1987).

[14] N. A. Hill, J. Phys. Chem. B **104**, 6694 (2000).

[15] E. Wendling, R. V. Hodenberg, and R. Kühn, Kali und Steinsalz **6**, 1 (1972).

[16] R. M. Honea and F. R. Beck, Am. Mineralogist **47**, 665 (1962).

[17] F. Bertaut, F. forrat, and P. Fang, C. R. Acad. Sci. **256**, 1958 (1963).

[18] V. A. Bokov, G. A. Smolenskiĭ, S. A. Kizhaev, and I. E. MyI'nikova, Sov. Phys. Solid State **5**, 2646 (1964).

[19] I. G. Ismailzade and S. A. Kizhaev, Sov. Phys. Solid State **7**, 236 (1965).

[20] J. Chappert, Phys. Lett. **18**, 229 (1965).

[21] R. J. Nelmes, J. Phys. C **7**, 3840 (1974).

[22] E. T. Keve, S. C. Abrahams, and J. L. Berkstein, J. Chem. Phys. **51**, 4928 (1969); **53**, 3279 (1970).

[23] M. DiDomenico, Jr., M. Eibschütz, H. J. Guggenheim, and I. Camlibel, Solid State Commun. **7**, 1119 (1969).

[24] M. Eibschütz and H. J. Guggenheim, Solid State Commun. **6**, 737 (1968).

[25] L. Holmes, M. Eibshütz, and H. J. Guggenheim, ibid. **7**, 973 (1969).

[26] J. F. Ryan and J. F. Scott, ibid. **14**, 5 (1974).

[27] H. Schmid, in *Magnetoelectric Interaction Phenomena in Crystals* (London, New York, Paris, p.121, 1975).

[28] Yu. N. Venevtsev, V. V. Gagulin, and V. N. Lyubimov, Sgnetomagnetiki: Obzor (Ferroelectromagnets: A review) NIITÉKhIM M., 1979.

[29] J. Van Suchtelen, Philips Res. Rep. 27, 28 (1972).

[30] J. Van Den Boomgaard, D. R. Terrelll, R. A. J. Born, and H. F. J. I. Giller, J. Mater. Sci. **9**, 1705 (1974).

[31] A. M. J. G. Van Run, D. R. Terell, and J. H. Scholing, J. Mater. Sci., **9**, 1710 (1974).

[32] J. Van Den Boomgaard, A. M. J. G. Van Run, and J. Van Suchtelen, Ferroelectric **10**, 295 (1976).

[33] J. Ryu, A. Vázquez Carazo, K. Uchino, and H. E. Kim, J. Electroceramics **7**, 17 (2001).

[34] B. T. Cong, N. N. Dinh, D. V. Hien, and N. L. Tuyen, Phyisca B **327**, 370 (2003).

[35] R. P. Mahajan, K. K. Patankar, M. B. Kothale, S. C. Chaudhari, V. L. Mathe, and S. A. Patil, Pramana J. Phys. **58**, 1115 (2002).

[36] J. Ryu, S. Priya, A. Vázquez Carazo, and K. Uchino, J. Am. Ceram. Soc. **84**, 2905 (2001).

[37] J. Ryu, A. Vázquez Carazo, K. Uchino, and H. E. Kim, Jpn. J. Appl. Phys. **40**, 4849 (2001).

[38] J. Ryu, S. Priya, K. Uchino, H.E. Kim, and D. Viehland, J. Korean Ceram. Soc. **39**, 813 (2002).

[39] N. Cai, J. Zhai, C. W. Nan, Y. Lin, and Z. Shi, Phys. Rev. B **68**, 224103 (2003).

[40] G. Srinivasan, E. T. Rasmussen, B. J. Levin, and R. Hayes, Phys. Rev. B **65**, 134402 (2002).

[41] A. Hanumaiah, T. Bhimasankaram, S. V. Suryanaryana, and G. S. Kumar, Bull. Mater. Sci. **17**, 405 (1994).

[42] J. Van Den Boomgaard, A. M. J. G. Van Run, and J. Van Suchtelen, Ferroelctrics **14**, 727 (1976).

[43] W. E. Kramer, R. H. Hopkins, and M. R. Danel, J. Mater. Sci. Lett. **12**, 409 (1977).

[44] A. E. Gelyasin and V. M. Laletin, Inorg. Mater. **24**, 1773 (1988).

[45] V. M. Laletin, Sov. Tech. Phys. Lett. **18**, 484 (1992).

[46] J. Van Den Boomgaard and R. A. J. Born, J. mater. Sci. **13,** 1538 (1978).

[47] T. G. Lupieko, I. B. Lopatina, I. V. Kozyrev, and L. A. Derbaremdiker, Inorg. Mater. **28**, 481 (1992).

[48] T. G. Lupeiko, S. S. Lopatin, I. V. Churikova, and I. B. Lopatina, Inorg. Mater. **27**, 2300 (1991).

[49] K. K. Patankar, V. L. Mathe, A. N. Patil, S. A. Patil, S. D. Lotke, Y. D. Kolekar, and P. B. Joshi, J. Electroceramics **6**, 115 (2001).

[50] G. Harshe, J. P. Dougherty, and R. E. Newnham, Int. J. Appl. Electromagn. Mater. **4**, 145 (1993).

[51] M. Avellaneda and G. Harshe, J. Intell. Mater. Syst. Struct. **5**, 501 (1994).

[52] C. W. Nan, G. Liu, and Y. Lin, Appl. Phys. Lett. **83**, 4366 (2003).

[53] G. A. Smolenskiĭ, Fizika Tverdogo Tela **4**, 1095 (1962).

[54] H. Zheng, J. Wang, S. E. Lofland, Z. Ma, L. Mohaddes-Ardabili, T. Zhao, L. Salamanca-Riba, S. R. Shinde, S. B. Ogale, F. Bai, D. Viehland, Y. Jia, D. G. Schlom, M. Wuttig, A. Roytburd, and R. Ramesh, Science **303,** 661 (2004).

[55] G. T. Rado, Phys. Rev. Lett. **6**, 609 (1961).

[56] G. T. Rado, Phys. Rev. **128**, 2546 (1962).

[57] G. T. Rado, in *Magnetoelectric Interaction Phenomena in Crystals*, J. Freeman and H. Schmid (Gordon and Breach: Newark, NJ, 1975).

[58] M. E. Lines and A. M. Glass, in *Principles of ferroelectrics* (Clarendon Press, Oxford Eng., 1977)

[59] W. H. Bragg, Philos. Mag. **30** 305 (1915).

[60] S. Nishikawa, Proc. Math. Phys. Soc. Tokyo, **8**, 199 (1915).

[61] L. Néel, Ann. Phys. **3**, 137 (1948).

[62] M. A. Willard, Y. Nakamura, D. E. Laughlin, and M. E. McHenry, J. Am. Ceram. Soc. **82**, 3342 (1999).

[63]Y. Yafet and C. Kittel, Phys. Rev. **87**, 290 1952).

[64] R. L. Ashbrook, J. Amer. Ceram. Soc. **60**, 428 (1977).

[65] V. S. Stubican and R. C. Bradt, Ann. Rev. Mater. Sci. **11**, 267 (1981).

[66] G. Blasse, ibid Suppl. **3**, 1, (1969).

[67] V. M. Laletin, Sov. Tech. Phys. Lett. **17**, 342 (1991).

[68] G. Prasad, T. Bhimasankaram and S. V. Suryanaryana, Mod. Phys. Lett. B **14**, 663 (2000).

[69] K. Lefki and G. J. M. Dormans, J. Appl. Phys. **76**, 1764 (1994).

[70] H. Zheng, *et al.* unpublished data.

[71] J. H. Li, *et al.* unpublished data.

[72] D. B. Chrisey and G. K. Hubler (Eds.), in *Pulsed Laser Deposition* (New York: John Wiley and Sons, 1994).

[73] M. Lorenz, H. Hochmuth, D. Natusch, M. Kusunoki, V. L. Svetchnikov, V. Riede, I. Stanca, G. Kästner, and Dietrich Hesse, IEEE Trans. Appl. Supercond. **11,** 3209 (2001).

[74] B. Fultz and J. Howe, in *Transmission electron microscopy and diffractometry of materials* (Berlin; New York: Springer, 2001).

[75] J. Benedict, R. Anderson, and S. J. Klepeis, in *MRS proceedings*, edited by R. Anderson, B. Tray, and J. Bravman (Pittsburgh, USA, **254**, p.121, 1992).

[76] S. D. Traynor, T. D. Hadnagy, and L. Kammerdiner, Integrated Ferroelectrics **16**, 63, (1997).

[77] H. Maiwa and N. Ichinose, Jpn. J. Appld. Phys Part 1-Regular papers, short notes and review papers **39**, 5403 (2000).

[78] S. Buhlman, B. Dwir, J. Baborowski, and P.Muralt, Appl. Phys. Lett. **75**, 3195 (2002).

[79] V. Nagarajan, *et al.*, Appl. Phys. Lett. **81**, 4215 (2002).

[80] S.Y. Chou, P. R. Krauss, and L. Kong, J. Appl. Phys. **79**, 6101 (1996).

[81] IBM, J. Res. Develop. **37,** 288 (1993).

[82] R. L. Kubena, F. P. Stratton, J. W. Ward, G. M. Atkinson, and R. J. Joyce, J. Vac. Sci. Technol. B **7,** 1798 (1989).

[83] U. Drodofsky, J. Stuhler, T. Schulze, M. Drewsen, B. Brezger, T. Pfau, and J. Mlynek, Appl. Phys. B **65**, 755 (1997).

[84] D. M. Eigler and E. K. Schweizer, Nature **344**, 524 (1990).

[85] A. D. Kent, D. M. Shaw, S. V. Molnar, and D. D. Awschalom, Science **262**, 1249 (1993).

[86] K. Pohl, M. C. Bartelt, J. de la Figuera, N. C. Bartelt, J. Hrbek, and R. Q. Hwang, Nature **397**, 238 (1999).

[87] H. Takeshita, Y. Suzuki, H. Akinaga, W. Mizutani, K. Tanaka, T. Katayama, and A. Itoh, Appl. Phys. Lett. **68**, 3040 (1996).

[88] D. D. Chambliss, R. J. Wilson, and S. Chiang, Phys. Rev. Lett. **66**, 1721 (1991).

[89] H. Burne, M. Giovannini, K. Bromann, and K. Kern, Nature **394,** 451(1998).

[90] V. A. Shchukin and D. Bimberg, Rev. Mod. Phys. **71**, 1125 (1999).

[91] C. Teichert, Physics Report, **365**, 335 (2002).

[92] J. Tersoff, C. Teichert, and M. G. Lagally, Phys. Rev. Lett. **76**, 1675 (1996).

[93] Y. H. Phang, C. Teichert, M. G. Lagally, L. J. Peticoloas, J. C. Bean, and E. Kasper, Phys. Rev. B **50**, 14435 (1994).

[94] P. Zeppenfeld, M. A. Krzyzowski, C. Romainczyk, R. David, and G. Comsa, Surf. Sci. **342**, L1131 (1995)

[95] P. Zeppenfeld, M. Krzyzowski, C. Romainczuk, G. Comsa, and M.G. Lagally, Phys. Rev. Lett. **72**, 2737 (1994).

[96] S. Jakubith, H.H. Rotermund, W. Engel, A. Von Oertzen, and G. Ertl, Phys. Rev. Lett. **65**, 3013 (1990).

[97] S. Facsko, T. Dekorsy, C. Koerdt, C. Trappe, H. Kurz, A. Vogt, and H. L. Hartnagel, Science **285**, 1551 (1999).

[98] Q. Xie, A. Madhukar, P. Chen, and N. P. Kobayashi, Phys. Rev. Lett. **75**, 2542 (1995).

[99] G. Springholz, V. Holy, M. Pinczolits, and E. Bauer, Science **282**, 734 (1998).

[100] F. L. Wang, J. C. Jiang, and E. I. Meletis, Appl. Phys. Lett. **12**, 2423 (2003).

[101] O. Fruchart, M. Klaua, J. Barthel, and J. Kirschner, Phys. Rev. Lett. **83**, 2769 (1999).

[102] L. Mohaddes-Ardabili, H. Zheng, S. G. Ogale, B. Hannoyer, W. Tian, J. Wang, S. E. Lofland, S. R. Shinde, T. Zhao, Y. Jia, L. Salamanca-Riba, D. G. Schlom, M. Wuttig, and R. Ramesh, Nature Materials **3**, 533 (2004).

[103] V. Moshnyaga, *et al.*, Nature Materials **2**, 247 (2003).

[104] R. W. Cahn and P. Haasen, in *Physical Metallurgy* (North-Holland, Amsterdam, 1983).

[105] J. W. Cahn, Acta Metall. **7**, 18 (1959).

[106] M. Atzmon, C. D. Adams, Y.-T. Cheng, and D. J. Srolovitz, Mater. Res. Soc. Symp. Proc. **202**, 143, (1991).

[107] C. D. Adams, M. Atzmon, Y.-T. Cheng, and D. J. Srolovitz, J. Mater. Res. **7**, 653 (1992).

[108] C. D. Adams and D. J. Srolovitz, J. Appl. Phys. **74**, 1707 (1993).

[109] M. Atzmon, D. A. Kessler, and D. J. Srolovitz, J. Appl. Phys. **72**, 442 (1992).

[110] S. M. Allen and J. W. Cahn, Acta Metall. **27**, 1085 (1979).

[111] S. Matsumura, H. Oyama, and K. Oki, Mater. Trans., Japan Inst. Metals **30**, 695 (1989).

[112] L.-Q. Chen and A. G. Khachaturyan, Acta Metall. Mater. **39**, 2533 (1991).

[113] L.-Q. Chen and A. G. Khachaturyan, Phys. Rev. B **46**, 5899 (1992).

[114] A. Onuki, J. Phys. Soc. Jpn. **60**, 345 (1991).

[115] R. K. Mishra and G. Thomas, J. Appl. Phys. **48**, 4576 (1977).

[116] E. Fatuzzo and W. J. Merz, in *Ferroelectricity* (North-Holland Pub.Co,; Wiley Interscience Publisher Division, Amsterdam, New York, 1967).

[117] Junling Wang, *Ph.D thesis* (University of Maryland, College Park, 2004).

[118] V. Janovec and Czech, J. Phys. **8**, 3 (1958).

[119] H. F. Kay and J. W. Dunn, Phil. Mag. **7**, 2027 (1962).

[120] Y. Sakashita, H. Segawa, K. Tominaga, and M. Okada, J. Appl. Phys. **73**, 7857 (1993).

[121] J. Junquera and P. Ghosez, Nature **422**, 506 (2003).

[122] M. Okuyama and Y. Hamakawa, Ferroelectrics **63**, 243 (1985).

[123] J. F. Scott, Topics Appl. Phys. **93**, 3 (2004).

[124] W. L. Zhong, B. D. Qu, P. L. Zhang, and Y. G. Wang, Phys. Rev. B **50**, 12375 (1994).

[125] A. G. Zembilgotov, N. A. Pertsev, H. Kohlstedt, and R. Waser, J. Appl. Phys. **91**, 2247 (2002).

[126] R. Kretschmer and K. Binder, Phys. Rev. B **20**, 1065 (1979).

[127] V. Nagarajan, S. Prasertchoung, T. Zhao, H. Zheng, J. Ouyang, R. Ramesh, W. Tian, X. Q. Pan, D. M. Kim, C. B. Eom, H. Kohlstedt, and R. Waser, Appl. Phys. Lett. **84**, 5225 (2004).

[128] M. D. Glinchuk, E. A. Eliseev, and V. A. Stephanovich, Physica B **322**, 356 (2002).

[129] I. P. Batra, P. Wurfel, and B. D. Silverman, J. Vac. Sci. Technol. **10**, 687 (1973).

[130] R. R. Mehta, B. D. Silverman, and J. T. Jacobs, J. Appl. Phys. **44**, 3379 1973).

[131] G. A. Rossetti, I. E. Cross, and K. Kushida, Appl. Phys. Lett. **59**, 2524 (1991).

[132] Z. G. Ban and S. P. Alpay, J. Appl. Phys. **91**, 9288 (2002).

[133] Y. Fujii and T. Sakudo, J. Phys. Soc. Jpn. **41**, 888 (1976).

[134] S. Roberts, Phys. Rev. **71**, 890 (1947).

[135] J. Smit and H. P. J. Wijn, in *Ferrites* (Philips Technical Library, Eindhoven, Netherlands, 1959).

[136] Y. Suzuki, G. Hu, R. B. Van Dover, and R. J. Cava, J. Magn. Magn. Mater. **191**, 1 (1999).

[137] E. M. Gyorgy, J. M. Phillips, Y. Suzuki, R. B. Van Dover, US Patent 5665465, September 9, 1997.

[138] L. Stichauer, G. Gavoille, and Z. Simsa, J. Appl. Phys. **79**, 3645 (1996).

[139] N. Murillo, E. Ochoteco, Y. Alesanco, J. A. Pomposo, J. Rodriguez, J. Gonzalez, J. J. del Val, J. M. Gonzalez, M. R. Britel, F. M. Varela-Feria, and A. R. de Arellanolopez, Nanotechnology **15**, S322 (2004).

[140] N. Moumen and M. P. Pileni, Chem. of Mater. **8**, 1128 (1996).

[141] G. Hu, J. H. Choi, C. B. Eom, V. G. Harris, and Y. Suzuki, Phys. Rev. B **62**, R779 (2000).

[142] Y. Suzuki, R. B. Van Dover, E. M. Gyorgy, J. M. Phillips, V. Korenivski, D. J. Werder, C. H. Chen, R. J. Cava, J. J. Krajewski, and W. F. Peck, Appl. Phys. Lett. **68**, 714 (1996).

[143] S. A. Chambers, R. F. C. Farrow, S. Maat, M. F. Toney, L. Folks, J. G. Catalano, T. P. Trainor, and G. E. Brown, J. Magn. Magn. Mater. **246**, 124 (2002).

[144] R. H. Kodama, J. Magn. Magn. Mater. **200**, 359 (1999).

[145] R. H. Kodama, A. E. Berkowitz, E. J. McNiff, Jr. and S. Foner, Phys. Rev. Lett. **77**, 394 (1996).

[146] R. P. Cowburn, A. O. Adeyeye, and M. E. Welland, Phys. Rev. Lett. **81**, 5414 (1998).

[147] R. P. Cowburn, D. K. Koltsov, A. O. Adeyeye, and M. E. Welland, Europhys. Lett. **48**, 221 (1999).

[148] R. P. Cowburn, D. K. Koltsov, A. O. Adeyeye, and M. E. Welland, J. Appl. Phys. **87**, 7082 (2000).

[149] R. P. Cowburn, J. Phys. D: Appl. Phys. **33**, R1 (2000).

[150] B. Hillebrands, C. Mathieu, C. Hartmann, M. Bauer, O.Büttner, S. Riedling, B. Roos, S.O. Demokritov, B. Bartenlian, C. Chappert, D. Decanini, F. Rousseaux, E. Cambril, A. Müller, B. Hoffmann, and U. Hartmann, J. Magn. Magn. Mater. **175**, 10 (1997).

[151] R. P. Cowburn, A.O. Adeyeye, and M.E. Welland, New J. Phys. **1**, 16.1 (1999).

[152] C. Mathieu, C. Hartman, M. Bauer, O.Büttner, S. Riedling, B. Ross, S.O. Demokritov, B. Hillebrands, B. Bartenlian, C. Chappert, D. Decanini, F. Rousseaux, E. Cambril, A. Müller, B. Hoffmann, and U. Hartmann, Appl. Phys. Lett. **70** (1997) 2912.

[153] R. M. Bozorth, in *Ferromagnetism* (IEEE Press, Piscataway, NJ, 1993).

[154] *Landolt-Börnstein: Magnetic Oxides and Related Compounds* Ш/4b, 366-393 (Springer, Berlin, Heidelderg, New York, 1970).

[155] C. Haginoya, S. Heike, M. Ishibashi, K. Nakamura, K. Koike, T. Yoshimura, J. Yamamoto, and Y. Hirayama, J. Appl. Phys. **85**, 8327 (1999).

[156] V. F. Puntes, P. Gorostiza, D. M. Aruguete, N. G. Bastus, and A. P. Alivisatos, Nature Materials **3**, 263 (2004).

[157] A. E. Berkowitz, J. A. Lahut, I. S. Jacobs, L. M. Levinson, and D.W. Forester, Phys. Rev. Lett. **34**, 594 (1975).

[158] A. E. Berkowitz, J.A. Lahut, and C.E. Van Buren, IEEE Trans. Magn. MAG-**16**, 184 (1980).

[159] R. H. Kodama, A. E. Berkowitz, E. J. McNiff, and S. Foner, Phys. Rev. Lett. **77**, 394 (1996).

[160] R. H. Kodama, J. Magn. Magn. Mater. **200**, 359 (1999).

[161] M. Lederman, D. Fredkin, R. O'Barr, R. Schultz, and S. Ozaki, J. Appl. Phys. **75,** 6217 (1994).

[162] W. Wernsdorfer, K. Hasselbach, A. Sulpice, A. Benoit, J. E. Wegrowe, L. Thomas, B. Barbara, and D. Mailly, Phys. Rew. B **53**, 3341 (1996).

[163] R. P. Cowburn, D. K. Koltsov, A. O. Adeyeye, M. E. Welland, and D. M. Tricker, Phy. Rew. Lett. **83**, 1042 (1999).

[164] A. Fernandez, M. R. Gibbons, M. A. Wall, and C. J. Cerjan, J. Magn. Magn. Mater. **190**, 71 (1998).

[165] A. Chizhik, J. Gonzalez, J. Yamasaki, A. Zhukov, and J. M. Blanco, J. Appl. Phys. **95**, 2933 (2004).

[166] R. E. Dunin-Borkowski, M. R. McCartney, B. Kardynal, and D. J. Smith, J. Appl. Phys. **95**, 374 (1998).

[167] J. F. Smyth, S. Schultz, D. Kern, H. Schmid, and D. Yee, J. Appl. Phys. **63**, 4237 (1988).

[168] A. L. Roitburd, Physica Status Solidi. *A* **37**, 329 (1976).

[169] A. L. Roytburd, J. Appl. Phys. **83**, 228 (1998).

[170] A. G. Khachaturyan, in *Theory of Structural Transformations in Solids* (Wiley, New York, 1993).

[171] Yi Qi, *et al.*, unpublished data.

[172] F. Zavaliche, *et al.*, unpublished data.

[173] G. Srinivasan, E. T. Rasmussen, J. Gallegos, and R. Srinivasan, Phys. Rev. B **64**, 214408 (2001).

[174] Y. Suzuki, R. B. Van Dover, E. M. Gyorgy, J. M. Phillips, V. Korenivski, D. J. Werder, C. H. Chen, R. J. Felder, R. J. Cava, J. J. Krajewski, W. F. Peck, and K. B. Do, App. Phys. Lett. **68**, 714 (1996).

[175] J. W. D. Martens and W. L. Peeters, J. Magn. Mag. Mater. **61**, 21 (1986).

[176] Yi Qi, *et al.*, unpublished data.

[177] K. S. Chang, M. A. Aronova, C. L. Lin, M. Murakami, M. H. Yu, J. Hattrick-Simpers, O. O. Famodu, S. Y. Lee, R. Ramesh, M. Wuttig, and I. Takeuchi, Appl. Phys. Lett. **84**, 3091 (2004).

[178] H. Zheng, *et al.,* to be submitted to Appl. Phys. Lett..

[179] J. Wang, J. B. Neaton, H. Zheng, V. Nagarajan, S. B. Ogale, B. Liu, D. Viehland, V. Vaithyanathan, D. G. Schlom,U. V. Waghmare, N. A. Spaldin, K. M. Rabe, M. Wuttig, and R. Ramesh, Science **299,** 1719 (2003).

[180] JF. Li, J. Wang, M. Wuttig, R. Ramesh, N. Wang, B. Ruette, A. P. Pyatakov, A. K. Zevzdin, and D. Viehland, Appl. Phys. Lett. **84**, 5261 (2004).

[181] K. Y. Yun, M. Noda, and M. Okuyama, Appl. Phys. Lett. **83**, 3981 (2003).

[182] Y. P. Wang, L. Zhou, M. F. Zhang, X. Y. Cheng, J. -M. Liu, and Z. G. Liu, Appl. Phys. Lett. **84**, 1731 (2004).

[183] J. R. Teague, R. Gerson, and W. J. James, Solid State Commun. **8**, 1073 (1970).

[184] C. Michel, J. -M. Moreau, G. D. Achenbach, R. Gerson, and W. J. James, Solid State Commun. **7**, 701 (1969).

[185] F. Kubel and H. Schmid, Acta Cryst. B **46**, 698 (1990).

[186] J. B. Neaton, C. Ederer, U. V. Waghmare, N. A. Spaldin, and K. M. Rabe, unpublished data.

[187] S. V. Kiselev, R. P. Ozerov, and G. S. Zhdanov, Sov. Phys. Dokl. **7**, 742 (1963).

[188] I. E. Dzyaloshinskii, Sov. Phys. JETP **5**, 1259 (1957).

[189] T. Moriya, Phys. Rev. **120**, 91 (1960).

[190] F. Léonard and R. C. Desai, Phys. Rev. B **56,** 4955 (1997).

[191] T. Walther, C. J. Humphreys, and A. G. Cullis, Appl. Phys. Lett. **71,** 809 (1997).

[192] V. F. Puntes, P. Gorostiza, D. M. Aruguete, N. G. Bastus, and A. P. Alivisatos, Nature Materials **3**, 263 (2004).